KU LEUVEN

ARENBERG DOCTORAL SCHOOL
Faculty of Engineering Science

Electrodeposition of semiconductor materials from non-aqueous electrolytes

Minxian Wu

Supervisor:
Prof. dr. ir. Jan Fransaer
Prof. dr. Koen Binnemans

Dissertation presented in partial fulfillment of the requirements for the degree of Doctor in Engineering

September 2015

Electrodeposition of semiconductor materials from non-aqueous electrolytes

Minxian WU

Examination committee:
Prof. dr. ir Dirk Vandermeulen, chair
Prof. dr. ir. Jan Fransaer, supervisor
Prof. dr. Koen Binnemans, supervisor
Prof. dr. ir. Marc De Bonte
Prof. dr. Edward Matthijs
Prof. dr. ir. Maria Seo
Prof. dr. ir. Philippe Vereecken
Prof. dr. Claudine Buess-Herman
(Université Libre de Bruxelles, Belgium)

Dissertation presented in partial fulfillment of the requirements for the degree of Doctor in Engineering

September 2015

© 2015 KU Leuven – Faculty of Engineering Science
Uitgegeven in eigen beheer, Minxian Wu, Kasteelpark Arenberg 44 box 2450, B-3001 Heverlee (Belgium)

Alle rechten voorbehouden. Niets uit deze uitgave mag worden vermenigvuldigd en/of openbaar gemaakt worden door middel van druk, fotokopie, microfilm, elektronisch of op welke andere wijze ook zonder voorafgaande schriftelijke toestemming van de uitgever.

All rights reserved. No part of the publication may be reproduced in any form by print, photoprint, microfilm, electronic or any other means without written permission from the publisher.

ISBN XXX-XX-XXXX-XXX-X

D/XXXX/XXXX/XX

Preface

First I would like to express my sincere gratitude to my promotors, Prof. Jan Fransaer and Prof. Koen Binnemans. I did my master thesis in Prof. Fransaer's group. After submitting my master thesis, I realized there were still a lot of things that I did not know but I wanted to know. I am very happy that Jan and Koen gave me the opportunity to continue exploring the world of electrochemistry. During the past four years, they offered me a lot of help. I can go to Jan's office whenever I have questions. He is always willing to help me to solve problems, discuss research and provide ideas. I got a lot of inspirations from him. I received a lot of help on coordination chemistry and a lot of guidance on academic writing from Koen. I really admire his working attitude. He corrects my every report so carefully that even the mistake of a punctuation has never been missed.

I also want to thank my assessors. Prof. Philippe Vereecken helped me to make deep understanding of rotating-ring disk electrode experiments and semiconductor electrochemistry. I always gained a lot of new knowledge from him after each meeting. I also thank Prof. Maria Seo for her help with transmission electron microscopy. I want to thank Prof. Marc De Bonte for giving me all the documents on germanium and silver germanium deposition. I am really impressed that all the documents are organized so well.

I would like to thank all my colleagues in our group: Stijn, Linda, Hai, Gana, Agniezka, Nocolo, Gijs, João, Jiangshui, Stapen, Bin Wu, Anastasiya, Christian, Xuan Zhang, Huang Zhang, Mikhail, Jianxun and Sam. Stijn is one of the senior researchers in our group and I obtained a lot of help from him. He always answered my questions with patient. Linda knows almost all the equipments in the lab and she taught me how to use the new QCM setup, helped me to do laser curvature experiment and AFM experiment. Hai was the daily supervisor of my master thesis and he showed me the world of electrochemistry. I am really grateful for the accompany of my dear colleagues. Their help and support make these four year colorful and joyful.

Of course without the help of all the technicians in our department, I can never finish this thesis. I want to express my deepest gratitude to Pieter, Marc, Britt, An, Paul, Olivier, Danny, Louis and Tom. I also would like to thank our secretaries, Huberte, Jennifer, Dirk and Mia.

There are so many great memories during these four years and I want to thank everyone presented in those happy moments. I especially want to thank my Chinese friends in our department. They not only shared joyful moments with me, but also helped me with my research. Xiebin, Fei, Gong, Yuanyuan, Xuan Wang, Wenxu, Xue Wang, Ling, Xiaoxu, Minwei, Liugang, Yanyan, Lichun, Xiaomi, Xiaodong, Hao, Chen, Pengcheng, Yujie, Luman, Chunwei, Zhuangzhuang and Bolu.

Last but not least, I want to thank my family, my husband Huayue and my parents. In fact, I have to say sorry to my parents. Four years ago, I was so selfish that I was against their will and insisted to do this PhD. They worried about me so much but they still showed their support when I made my final decision. Without their support, I do not think I can ever finish this thesis.

Abstract

Electrodeposition is a cost-efficient and convenient method to prepare thin film materials on conductive substrates. The film morphology, composition and deposition rate can be easily controlled by changing the deposition conditions such as applied potential, current, temperature, agitation and bath composition. This PhD research investigated the electrodeposition of semiconductor materials: (1) electrodeposition of bismuth-tellurium and bismuth-antimony-tellurium thermoelectric materials from ethylene glycol solutions; and (2) electrodeposition of germanium from ionic liquids.

Bismuth telluride and its derived alloys, $(Bi_{1-x}Sb_x)_2(Se_{1-y}Te_y)_3$ ($0 \leq x, y \leq 1$), have the best thermoelectric properties at room temperature. In ethylene glycol, $Bi(NO_3)_3$, $TeCl_4$ and $SbCl_3$ have high solubilities up to 1 M which are more than 100 times higher than the solubility of Te(IV) ions in aqueous solutions. The most interesting finding is that the equilibrium alloy deposition can be achieved in chloride-free ethylene glycol solutions. This means the atomic ratio of bismuth to tellurium in the electrodeposited film is the same as the element ratio of [Bi(III)]/[Te(IV)] in the electrolyte. The film composition can be easily adjusted with the composition of the electrolyte. Removing Chloride ions also improves the film morphology and reduces the corrosiveness of the electrolyte. Mirror-like bismuth telluride films could be obtained from the chloride-free solutions. High deposition rate up to -3 A dm^{-2} was reached. Depending on the film composition, both p-type and n-type materials could be obtained. A maximum Seebeck coefficient of -120 µm V^{-1} was obtained.

Preparation of multilayered $Bi_2Te_3/(Bi_{1-x}Sb_x)_2Te_3$ thin films were studied for reducing the thermal conductivity and boosting the Seebeck coefficient. It was found that two different forms of antimony formed at different potentials. At lower overpotentials, the electrodeposited antimony is probably in a metastable "explosive" form that can rapidly change from amorphous into crystalline, and at higher overpotentials, crystalline antimony is electrodeposited. The deposition of bismuth-antimony and antimony-tellurium alloys followed the regular alloy

deposition behavior. In a solution containing all three elements, ternary alloys with different compositions can be obtained and the composition depends on the deposition conditions. More antimony was present in the alloy if higher rotation speeds or higher overpotentials were applied. A pulsed potential was used to get multilayered structures and the layer thickness could be easily controlled by the pulse time. In theory, multilayered structures could reduce the thermal conductivity by phonon scattering at the interfaces of the layers.

Electrodeposition of germanium has been performed in aqueous and organic solvents before. But due to the hydrogen evolution on germanium, only ultra thin films could be obtained from aqueous solutions and the current efficiency in organic solvent is extremely low. Ionic liquids are ideal solvents for germanium deposition because water can be easily removed and germanium tetrachloride ($GeCl_4$) has a very high solubility in some ionic liquids. In this research, the germanium compound $[GeCl_4(BuIm)_2]$, which is much less volatile than $GeCl_4$, was synthesized and used in 1-butyl-1-methylpyrrolidinium dicyanamide ([BMP][DCA]). Black germanium films could be obtained. Only a small amount of oxygen impurity was found which could be due to the oxidation of germanium films in the air. This is a great improvement compared to the films deposited from solutions containing $GeCl_4$. In those films, besides oxygen, chlorine and carbon impurities were always observed. However, electropolymerization of $[DCA]^-$ anions was observed on the cathode during deposition and the products were poorly conductive. To suppress the polymerization, [BMP]Cl was added and the deposition temperature was increased to 100 °C to make sure all [BMP]Cl was dissolved. The current density increase with increasing temperature. Temperatures above 100 °C still led to the polymerization of the $[DCA]^-$ anions.

1-Butyl-1-methylpyrrolidinium bis(trifluoromethylsulfonyl)imide [BMP][Tf_2N] containing $GeCl_4$ was used as electrolyte at elevated temperatures up to 180 °C. To prevent the evaporation of $GeCl_4$, a pressure cell was designed and used. A high deposition rate of 6 µm h^{-1} was found at elevated temperatures due to the improved mass transport of the germanium compound and the kinetics of the reactions. The film morphology had also improved. Instead of black germanium films that always form at room temperature, metallic grey shiny germanium layers were obtained. Unfortunately, oxygen, carbon and chlorine impurities were found in the deposited films.

Beknopte samenvatting

Elektrodepositie is een kosten-efficiënte en handige methode om dunne films af te zetten op geleidende substraten. De morfologie van de films, hun samenstelling en de depositiesnelheid kunnen eenvoudig worden gecontroleerd aan de hand van potentiaal, stroom, temperatuur, agitatie en badsamenstelling. Dit promotieonderzoek onderzocht de elektrodepositie van halfgeleidende materialen: (1) het afzetten van thermo-elektrische materialen op basis van legeringen van bismut-telluur en bismut-antimoon-telluur uit ethyleenglycoloplossingen; en (2) elektrodepositie van germanium uit ionische vloeistoffen.

Bismuttelluride (Bi_2Te_3) en de daarvan afgeleide legeringen hebben de beste thermo-elektrische eigenschappen bij kamertemperatuur. In ethyleenglycol hebben zowel $Bi(NO_3)_3$, $TeCl_4$ als $SbCl_3$ een hoge oplosbaarheid tot 1 M. Dit is meer dan honderd maal hoger dan de oplosbaarheid van Te(IV)-ionen in waterige oplossingen. Chloriden werden verwijderd om de filmmorfologie te verbeteren en de corrosiviteit van het elektrolyt te verminderen. De meest interessante ontdekking is dat uit chloridevrije ethyleenglycoloplossingen evenwichtslegeringen kunnen worden afgezet. Dit betekent dat de atoomverhouding van bismut tot telluur in de film dezelfde is als de verhouding [Bi(III)]/[Te(IV)] in de oplossing. De filmsamenstelling kan dus gemakkelijk worden bepaald door de keuze van de samenstelling van de elektrolyt. Spiegelende bismut-telluurfilms konden afgezet worden uit de chloridevrije oplossingen. Afhankelijk van de filmsamenstelling, kunnen zowel p-type als n-type materialen worden verkregen. De hoogste Seebeck-coëfficiënt die werd opgemeten was -120 µm V^{-1}.

Het afzetten van dunne, $Bi_2Te_3/(Bi_{1-x}Sb_x)_2Te_3$ multilagen werd bestudeerd met als doel het verminderen van de thermische geleidbaarheid en daarmee het verhogen van de Seebeck coëfficiënt. Bij lage overpotentialen, leidt de elektrodepositie van antimoon tot een amorfe afzetting, bij hogere overpotentialen groeit het antimoon kristallijn. De afzetting van bismut-antimoon-en antimoon-telluriumlegeringen volgde het gedrag van reguliere

legeringsdepositie. In de oplossing waarin de drie elementen waren opgelost konden ternaire legeringen met verschillende samenstellingen verkregen worden en de samenstelling was afhankelijk van de experimentele parameters. De concentratie van antimoon was hoger voor hogere rotatiesnelheden of bij grotere overpotentialen. Pulsdepositie werd gebruikt om meerlagige structuren te bekomen en de laagdikte kon gemakkelijk worden gekozen door de pulstijd te variëren. In theorie kan een meerlagige structuur de thermische geleidbaarheid verminderen door phononverstrooiing op de grensvlakken van de lagen. Daarom is het jammer dat de thermische geleidbaarheid van de meerlaagse afzettingen niet nauwkeurig kon worden gemeten.

Elektrodepositie van germanium kan worden uitgevoerd in waterige en organische oplosmiddelen. Maar omwille van waterstofontwikkeling op germanium, kunnen slechts ultradunne films worden verkregen uit waterige oplossingen en in organische solventen is het stroomrendement extreem laag. Ionische vloeistoffen zijn een geschikt medium voor germaniumdepositie omdat water gemakkelijk kan worden verwijderd en germaniumtetrachloride ($GeCl_4$) een zeer hoge oplosbaarheid heeft in sommige ionische vloeistoffen. In dit onderzoek, is $[GeCl_4(BuIm)_2]$ gebruikt. Deze germaniumverbinding is minder vluchtig dan $GeCl_4$ en werd gebruikt in 1-butyl-1-methylpyrrolidinium dicyanamide ([BMP][DCA]). Zwarte germanium films waren het resultaat. Slechts een kleine hoeveelheid zuurstof werd gedetecteerd omwille van oxidatie aan de lucht. Dit is een grote verbetering ten opzichte van de afzettingen uit oplossingen met $GeCl_4$. In deze films werden, naast zuurstof, ook chloor- en koolstofonzuiverheden waargenomen. Jammer genoeg werd echter elektropolymerisatie van $[DCA]^-$ anionen op de kathode waargenomen tijdens afzetting. De reactieproducten daarvan zijn slechte geleiders van elektriciteit. Om de polymerisatie te onderdrukken werd [BMP]Cl toegevoegd en de depositietemperatuur werd verhoogd tot 100 °C om er voor te zorgen dat alle [BMP]Cl was opgelost. De stroomdichtheid bleek verhoogd door de toename van de temperatuur. Een te hoge temperatuur leidde echter opnieuw tot de polymerisatie van $[DCA]^-$ anionen.

1-Butyl-1-methylpyrrolidinium bis(trifluoromethylsulfonyl)imide $[BMP][Tf_2N]$ met opgelost $GeCl_4$ werd gebruikt bij verhoogde temperaturen tot 180 °C. Om de verdamping van $GeCl_4$ voorkomen, werd een drukcel gemaakt. Hoge depositiesnelheiden werden gevonden bij deze temperaturen door de toename van het massatransport en de verbeterde kinetiek van de reacties. De filmmorfologie was ook beter. In plaats van zwarte afzettingen, die bij kamertemperatuur gemaakt werden, waren de afzettingen bij 180 °C metallisch grijs en glanzend. Jammer genoeg bevatten de afgezette deklagen nog steeds zuurstof, koolstof en chloor.

Contents

References a

Abstract iii

Contents vii

1 Introduction 1

1.1 Thermoelectric materials 1

1.1.1 Thermoelectric effects and conversion efficiency 1

1.1.2 Room temperature thermoelectric materials 6

1.1.3 Electrodeposition of room temperature thermoelectric materials 10

1.1.4 A short summary 11

1.2 Germanium 12

1.2.1 Germanium and its applications 12

1.2.2 Electrodeposition of germanium 14

1.2.3 A short summary 20

1.3 General introduction of semiconductor electrochemistry 20

1.3.1 Metal-semiconductor interface 20

1.3.2 Semiconductor-electrolyte interface 24

1.3.3 Germanium electrode 29
1.4 Outline of the thesis 31

2 Electrodeposition of Bi_2Te_3 from chloride-free ethylene glycol solutions 35

2.1 Introduction 37
2.2 Experimental 37
2.3 Results and discussion 39
2.3.1 Chloride-free electrolytes 39
2.3.2 Electrochemical behaviors of bismuth and tellurium ions in chloride-free solutions 40
2.3.3 Bismuth telluride electrodeposition 45
2.4 Conclusions 51

3 Pulsed electrodeposition of thermoelectric $Bi_2Te_3/(Bi_{1-x}Sb_x)_2Te_3$ multilayers 53

3.1 Introduction 55
3.2 Experimental 56
3.3 Results and discussion 57
3.3.1 Electrodeposition of antimony in ethylene glycol 57
3.3.2 Electrodeposition of Sb-Te and Bi-Sb alloys 61
3.3.3 Electrodeposition of multilayered thermoelectric material 67
3.4 Conclusions 72

4 Electrodeposition of germanium from the ionic liquid 1-butyl-1-methylpyrrolidinium dicyanamide 75

4.1 Introduction 77
4.2 Experimental 78
4.3 Results and discussions 80
4.3.1 Electrochemistry of $[GeCl_4(BuIm)_2]$ in [BMP][DCA] . . 82

4.3.2 Electrodeposition of germanium in [BMP][DCA] 87
4.3.3 Polymerization of dicyanamide at the anode 91
4.3.4 Electrodeposition from [BMP][DCA] and [BMP]Cl mixture 94
4.4 Conclusions 98

5 Electrodeposition of germanium at elevated temperatures and pressures 99

5.1 Introduction 101
5.2 Experimental 102
5.3 Results and discussion 104
5.3.1 Electrodeposition of germanium using $[GeCl_4(BuIm)_2]$
5.3.2 Electrodeposition of germanium using $GeCl_4$ 106
5.4 Conclusions 122

6 General conclusions and outlook 125

6.1 Conclusions 125
6.1.1 General conclusions 125
6.1.2 Breakthroughs 127
6.2 Outlook for future research 127

Bibliography 129

List of publications 147

List of Figures 149

List of Tables 155

Chapter 1

Introduction

Traditional fossil fuels have been serving our society for decades. They are, however, the main source of greenhouse gases and not renewable. There is an urgent demand for clean energy sources to reduce the consumption of fossil fuels. The electronic devices used in renewable energy systems such as solar cells and thermoelectric generators are attracting a great deal of interests. The functional materials in these devices are semiconductors and preparation of those semiconductor materials using electrodeposition is the main topic of this PhD.

In the following sections, the review of the literature describes two types of materials: thermoelectric materials and germanium. Section 1.1 introduces the thermoelectric effects and electrodeposition of room temperature thermoelectric materials. Section 1.2 deals with a general view of germanium and its applications and summarizes the literature of the electrodeposition of germanium near room temperature. A brief introduction of semiconductor electrochemistry is presented in section 1.3. Section 1.4 introduces the outline of this thesis.

1.1 Thermoelectric materials

1.1.1 Thermoelectric effects and conversion efficiency

In the 1820s, Thomas Johann found that the needle of a compass deflected by heating one the junctions of two dissimilar metals. This phenomenon was later known as the Seebeck effect: an electrical potential, electromotive force

(emf), is generated within any conducting material that has a temperature gradient [1]. The Seebeck effect originates from the diffusion of the charge carriers and dragging of the phonons in the material. The temperature gradient in the material forces the charge carriers to move from one side to the other. On the other hand, phonons also move against the temperature gradient and transfer their momentum to charge carriers which are pushed to move and create a gradient of charge carriers in the material. Due to this gradient in electric charge carriers an electric potential is generated. The electrical potential generates due to the gradient of the charge carriers. The Seebeck coefficient is the change of the emf with temperature at a given temperature [1]:

$$S = \left(\frac{\Delta V}{\Delta T}\right)_T \tag{1.1}$$

The Seebeck coefficient can be either positive or negative depending on the type of the majority charge carriers in the material. Metals and n-type semiconductors usually have negative Seebeck coefficients and p-type semiconductors normally have positive Seebeck coefficients. Thermoelectric generators and thermocouples are the most important applications of the Seebeck effect.

About 20 years after discovering the Seebeck effect, another thermoelectric effect was discovered by a French physicist Jean Peltier: an electrical current can generate a temperature difference at the junctions of two dissimilar metals. This effect is a result of the entropy change of the electrical charge carriers when they flow across a junction [1]. The relative Peltier coefficient (Π_{AB}) indicates the heat absorbed by the lower junction per unit time ($\dot{Q}$) at a given current (i):

$$\Pi_{AB} = \Pi_A + \Pi_B = \frac{\dot{Q}}{i} \tag{1.2}$$

where Π_A and Π_B are the absolute Peltier coefficients of the conductors. The direction of the current flow determines whether heat adsorption or liberation happens at the junction. The main application of the Peltier effect is the thermoelectric cooler.

In 1851, William Thomson (Lord Kelvin) found the effect of the interactions between temperature and current in solids. When the electrical carriers flow in the same direction as the temperature gradient, the potential energy decreases and it liberates heat. If the electrical carriers flow in the direction opposite to the temperature gradient, the potential energy increases, as a result, the material absorbs heat [1].

Thermoelectric materials can be used as thermoelectric generator and/or refrigerator. Figure 1.1 shows a simplified thermoelectric generator. It is composed of a negative (n-type) and a positive (p-type) branch which are

connected to the metallic conductor. When there is a heat input at one end (T_h) and a heat sink at the other end (T_c), a voltage is generated and a current will start to flow. The conversion efficiency η_g is calculated from electrical energy W and input heat Q:

$$\eta_\mathrm{g} = \frac{W}{Q} \tag{1.3}$$

It depends on the temperature difference at the two ends of the generator, the nature of the materials and the design of the device, as well as the external load. The maximum conversion efficiency is a combination of the ideal Carnot efficiency (η_Carnot) and the property of the material:

$$\eta_\mathrm{max} = \left(1 - \frac{T_\mathrm{c}}{T_\mathrm{h}}\right) \frac{\sqrt{1+Z\bar{T}}-1}{\sqrt{1+Z\bar{T}}+\frac{T_\mathrm{c}}{T_\mathrm{h}}} \tag{1.4}$$

$$= \eta_\mathrm{Carnot} \frac{\sqrt{1+Z\bar{T}}-1}{\sqrt{1+Z\bar{T}}+\frac{T_\mathrm{c}}{T_\mathrm{h}}} \tag{1.5}$$

where $\bar{T} = \frac{1}{2}(T_\mathrm{c}+T_\mathrm{h})$ is the average temperature (K), and Z is the figure of merit (K^{-1}) which is a temperature dependent parameter. The dimensionless figure of merit ZT is commonly used to evaluate the performance of thermoelectric materials:

$$ZT = \frac{S^2\sigma}{\kappa}T \tag{1.6}$$

where σ is the specific electrical conductivity (Ω^{-1} m^{-1}) and κ is the specific thermal conductivity (W $\mathrm{m}^{-1}\mathrm{K}^{-1}$). The thermoelectric generator is a device that converts thermal energy into electrical energy. In theory, the efficiency of the thermoelectric generator can reach the ideal Carnot efficiency if the figure of merit ZT approaches infinity. However, the Carnot efficiency can never be achieved in reality because the highest ZT value reported today is 3.6 which is a Bi-doped quantum-dot superlattice of composition $\mathrm{PbTe/PbSe_{0.98}Te_{0.02}}$ [2].

Figure 1.2 shows a schematic drawing of a thermoelectric cooler. When a current is applied to the device, heat is absorbed at one junction and released at the other junction. The conversion efficiency for a thermoelectric cooler is the ratio of the amount of heat it absorbs Q to the input electrical energy W:

$$\varphi_\mathrm{c} = \frac{Q}{W} \tag{1.7}$$

The maximum conversion efficiency of a thermoelectric cooler is:

$$\varphi_\mathrm{max} = \left(\frac{T_\mathrm{c}}{T_\mathrm{h}-T_\mathrm{c}}\right) \frac{\sqrt{1+Z\bar{T}}-\frac{T_\mathrm{h}}{T_\mathrm{c}}}{\sqrt{1+Z\bar{T}}+1} \tag{1.8}$$

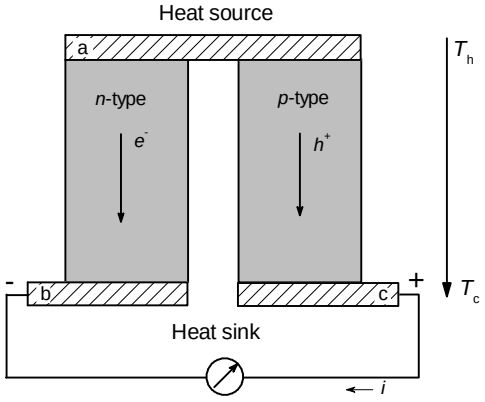

Figure 1.1: Schematic of a thermoelectric generator. It consist of a n-type and a p-type material connected to the metallic conductors a, b and c.

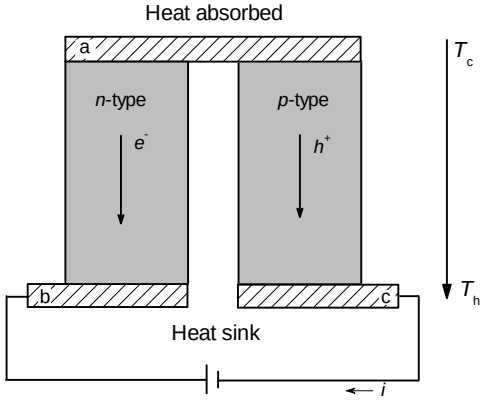

Figure 1.2: Schematic of a thermoelectric cooler.

The maximum conversion efficiency of a thermoelectric cooler is also a function of the Carnot efficient and the nature of the materials. To obtain a higher conversion efficiency, a higher ZT number is required.

Equation 1.6 reveals that materials with high ZT number require a low thermal conductivity (κ) and high power factor ($S^2\sigma$). However, those parameters are not independent from each other and are determined by the charge carrier concentration n. Figure 1.3 shows the effect of charge carrier concentration on those parameters. The electrical conductivity σ increases with the increase of

carrier concentration. On the other hand, the Seebeck coefficient S decreases as more carriers are present in the material:

$$S = \frac{8\pi^2 k_B^2}{3eh} m^\star T (\frac{\pi}{3n})^{\frac{2}{3}} \tag{1.9}$$

where k_B is the Boltzmann constant [1.38 10^{-23} J K^{-1}], e is elementary charge [1.61 10^{-19} C], $m^\star$ is effective mass of charge carrier and h is the Plank constant [6.6 10^{-34} J]. The power factor $S^2\sigma$ is very small for an insulator owing to the negligible electrical conductivity. Although metals have very high electrical conductivity, the power factors for metals are also very low due to the high carrier concentration. On the other hand, semiconductors have relatively high power factors. A maximum power factor $S^2\sigma$ is obtained when the carrier concentration is around 10^{20} cm^{-3}. The thermal conductivity κ is the sum of the lattice (phonon) thermal conductivity κ_p and the electronic thermal conductivity κ_e:

$$\kappa = \kappa_p + \kappa_e \tag{1.10}$$

The carrier concentration only affects the electronic contribution of the thermal conductivity. Electronic thermal conductivity increase proportionally with the carrier concentration. The lattice thermal conductivity is from the lattice vibration, which depends on the atomic weight of the material and heavy elements like bismuth, lead, tellurium, etc. normally have low lattice thermal conductivity. Overall, semiconductors that are used as thermoelectric materials have higher ZT numbers than metals and insulators.

In order to increase the figure of merit ZT, the thermal conductivity κ should be lowered while the power factor $S^2\sigma$ is maintained. The most straight forward way is to reduce the phonon thermal conductivity (κ_p) by selectively scattering phonons. This can be achieved by introducing scattering locations in the materials. Small defects, lattice dislocations and inclusions can be introduced into the material to reduce the mean free path of the phonons. Nanostructured materials have a small grain size and large amount of grain boundaries increasing the grain boundary scattering. In multilayer or superlattice materials, phonons scatter at the interfaces between two layers due to the mismatch of the crystal structures and difference in mass. However, nanoparticles or interfaces between layers not only scatters the phonons, but also affects the movement of electrons. In multilayers, an electron barrier forms between two semiconductor layers or semiconductor/metal layers. Those with energies higher than the barrier can overcome the barrier and contribute to the electrical conductivity. Electrons with energies lower than the barrier are filtered. Thanks to the "electron filtering", although the electrical conductivity is reduced, the Seebeck coefficient S can be increased due to the reduction of the number of charge carriers [4]. It is possible to increase the power factor $S^2\sigma$ by electron filtering. This effect is also present in the materials containing nanoparticles [5].

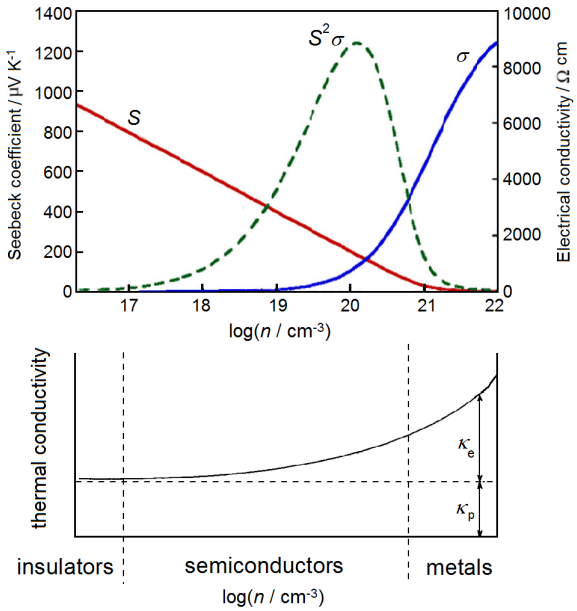

Figure 1.3: Carrier concentration dependency of Seebeck coefficient S, electrical conductivity σ, thermal conductivity κ and power factor $S^2\sigma$ (schematic) [3].

1.1.2 Room temperature thermoelectric materials

Thermoelectric effects are present in all of materials but this does not mean that all materials are useful for thermoelectric devices because of their low figure of merit. As shown in Figure 1.3, semiconductors have the highest power factor and reasonably low thermal conductivity. Figure 1.4 shows the figure of merit of different materials at different temperatures. The figure of merit changes with temperature and there is no material that has good thermoelectric properties over the whole temperature range. For high temperature applications ($>$ 800 °C), silicon-germanium alloys work best because of the high ZT number and low cost compared to other rare earth compounds. Lead chalcogenides (PbTe, etc.) and skutterudites ($CoSb_3$, $CeFe_4Sb_{12}$, etc.) are used in moderate temperature applications [6, 7]. Around room temperature, n-type bismuth telluride and p-type antimony telluride have the highest ZT values. Because of that, bismuth telluride and the derived antimony- and selenium-doped compounds are used extensively as thermoelectric generators and thermoelectric coolers in electronics near room temperature.

The crystal structure of bismuth telluride is rhombohedral but it is easier to describe it as an hexagonal cell with quintuple layers (-$Te^{(1)}$-Bi-$Te^{(2)}$-Bi-$Te^{(1)}$-) stacking along the *c*-axis [8]. The crystal structure is shown in Figure 1.5. The bonds between $Te^{(1)}$ and Bi, $Te^{(2)}$ and Bi are ionic-covalent bonds, whereas the bonds between $Te^{(1)}$ atoms are van der Waals bonds which are much weaker [9, 10]. Because the bonding between $Te^{(1)}$ and Bi, $Te^{(2)}$ and Bi are stronger than the bonds between adjacent $Te^{(1)}$ planes, the crystals prefer to grow along the layers perpendicular to the *c*-axis resulting in plate-like crystals. As shown in Figure 1.5, tellurium atom/ion A and B are approaching the crystal in two different directions. Because tellurium atom A can only be weakly bonded to the material by van der Waals force, it easily goes back to the solution. On the other hand, tellurium atom B can form a strong covalent bond with the material leading to a crystal growth along the layers. Due to the crystal structure, the thermal conductivity and electrical conductivity are anisotropic. The electrical conductivity and thermal conductivity measured perpendicular to the *c*-axis are higher than those measured along the other directions. The Seebeck coefficient is more or less isotropic with only 10% difference between S_{33} and S_{11}. The highest figure of merit is measured in the direction perpendicular to the *c*-axis [1]. The Seebeck coefficient S as a function of the composition at room temperature is shown in Figure 1.6. Depending on the composition of the material, bismuth-tellurium can be either n-type or p-type. Tellurium-rich alloys (62.5 at.%–73 at.%) are n-type materials and the alloys are p-type materials when the tellurium concentration is in the range of 51 at.%–62.5 at.%. The band gap of bismuth telluride is only 0.16 eV at 300 K [11].

Antimony telluride has the same rhombohedric crystal structure as bismuth telluride. The structure also can be seen as a hexagonal cell which is constructed with quintuple layers stacked along the *c*-axis. The ternary alloy $(Bi_{1-x}Sb_x)_2Te_3$ is constituted from antimony telluride and bismuth telluride. The bismuth atoms are substituted by the antimony atoms. The Seebeck coefficient of $(Bi_{1-x}Sb_x)_2Te_3$ at room temperature is shown in Figure 1.7. The Seebeck coefficient not only depends on the composition of the alloy, but is also affected by the processing techniques. $(Bi_{1-x}Sb_x)_2Te_3$ single crystals are p-type semiconductors and the Seebeck coefficient decreases as the doping level of antimony increases [1]. Bulk polycrystalline alloys made by mechanical grinding-hot press (MG-HP) and mechanical alloying-pulsed discharge sintering (MA-PDS) have a p-n transition when x is around 0.57–0.67. [15, 16].

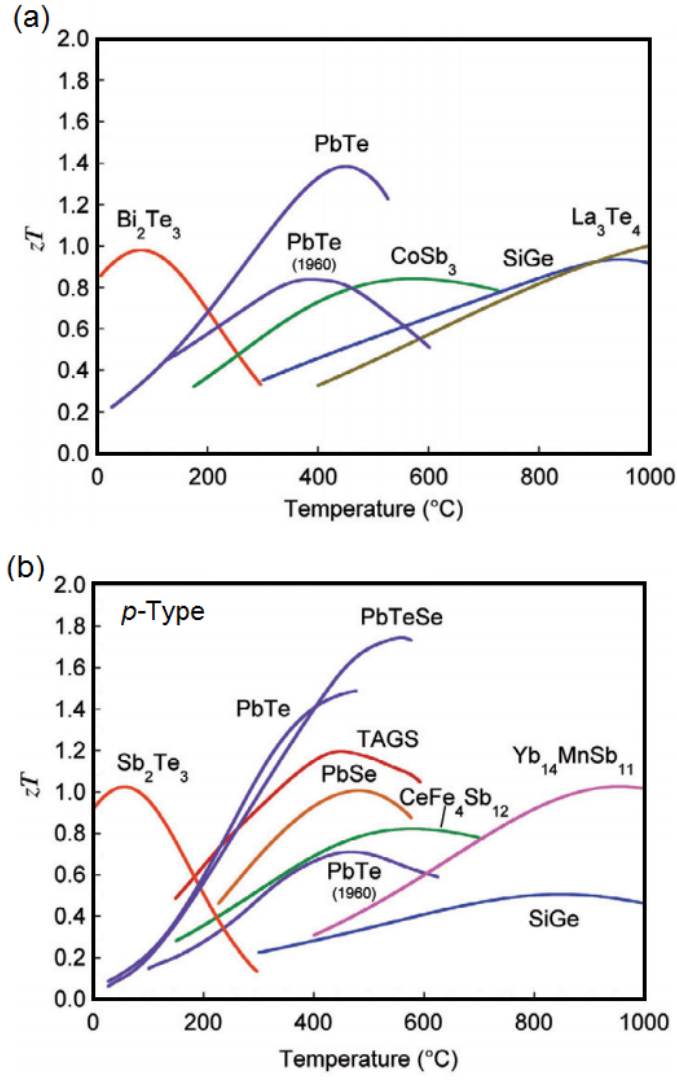

Figure 1.4: Figure of merit of (a) n-type and (b) p-type materials at different temperatures (from [12] with permission).

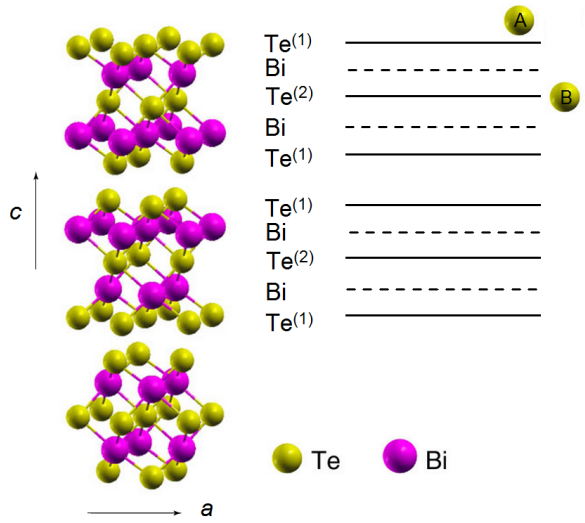

Figure 1.5: Crystal structure of Bi_2Te_3 (adapted from [13])

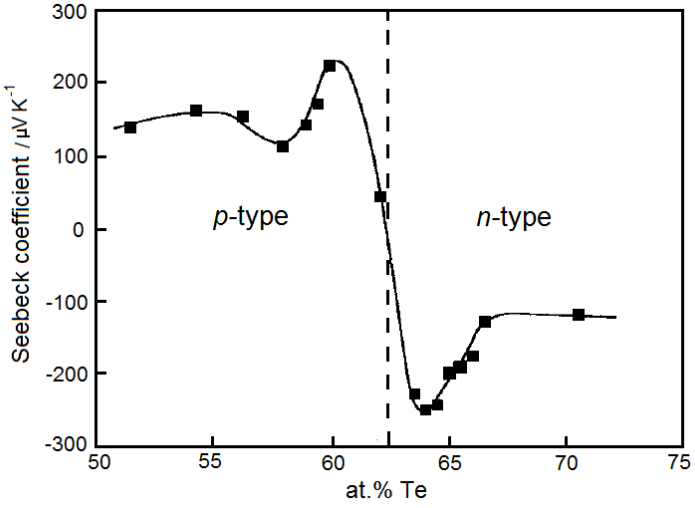

Figure 1.6: Seebeck coefficient of bismuth-tellurium alloys at room temperature (from reference [1, 14]).

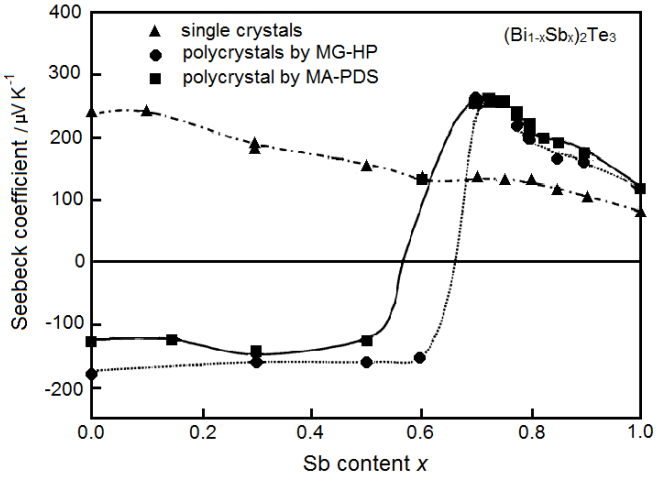

Figure 1.7: Seebeck coefficient of $(Bi_{1-x}Sb_x)_2Te_3$ alloys at room temperature (from [16] with permission).

1.1.3 Electrodeposition of room temperature thermoelectric materials

The thermoelectric performance of materials is one of the key factors in the development of thermoelectric devices. In 1950s, the development of thermoelectric devices was rapidly rising due to the discovery of semiconductors as thermoelectric materials. Before that, thermoelectric materials were only used in thermocouples for measuring temperature. With the growth of the semiconductor industry, thin film materials have been introduced to thermoelectric devices [17]. Compared to conventional bulk thermoelectric materials (> 200 µm thick), thin film thermoelectric materials are typically 5 to 30 µm thick which significantly reduce the dimension of the devices [18, 2]. Moreover, the cost of the materials can be reduced which is another important factor that promotes the development of thermoelectric devices.

Thermoelectric films can be prepared by various methods, including chemical vapor deposition (CVD) [19, 20], physical vapor deposition (PVD) [21, 22], pulsed laser deposition [23, 24, 25], molecular beam epitaxy (MBE) [2, 26], ion-beam mixing [27], screen printing [28, 29, 30], electrodeposition [31], etc. [32, 33, 34, 35]. Electrodeposition is one of the favorite techniques in the industry because of the low operation and capital cost and high deposition rate. The properties of the materials can be easily adjusted by the deposition conditions [31]. The electrodeposition of Bi_2Te_3 attracts a great interest since the 1990s.

In the 1990s, only fewer than 5 articles per year were published on this topic and this number increased to about 20 articles per year in the 2000s [36].

Because the band gap of the band gap of Bi_2Te_3 is only 0.16 eV at room temperature, the electrodeposition behavior of this compound is more like that of a metal than a semiconductor. Electrodeposition of Bi_2Te_3 is mostly carried out from aqueous electrolytes containing nitric acid. In some cases, other electrolytes with $HClO_4$, H_2SO_4, or ethylenediaminetetraacetic acid (EDTA) are used [36, 37, 38, 39]. In the nitric acid solutions, $Bi(NO_3)_3$ or Bi_2O_3 and TeO_2 or Te metal are commonly used as metal ion precursors. The concentration of metal ions in the solution normally ranges from 0.6 mM to 20 mM because of the low solubility of $HTeO_2^+$ ions even at very low pH [36, 40]. In electrolytes with H_2SO_4, $Bi_2(SO_4)_3$ and K_2TeO_3 were used as precursors. However, the solubility of metal ions was also very low. K_2TeO_3 had the highest solubility of 3.4 mM in this electrolyte. Due to the low solubilities of metal ions in aqueous solutions, electrodeposition was performed at limiting current densities in order to obtain reasonable deposition rates of 2-6 µm h^{-1}. The deposition rates of each element in aqueous solutions were mass transport controlled. Because the diffusion coefficient of the bismuth ions is lower than the diffusion coefficient of tellurium ions, the ratio of bismuth and tellurium in the films is lower than the ratio of metal ion concentration in the solutions. The electrodeposited films often have a preferential (110) orientation corresponding to the plane perpendicular to the *c*-axis which is a suitable orientation in module configuration [36]. The Seebeck coefficient can reach values of -200 µV K^{-1} for n-type Bi_2Te_3 thin film deposited from aqueous solutions [14, 41]. Also for the electrodeposition of alloys containing antimony, acidic electrolytes are also most commonly used. Seebeck coefficients of +213 µV K^{-1} were reported for $(Bi_{1-x}Sb_x)_2Te_3$ films that were electrodeposited from a solution with nitric acid [42]. To prevent the attack by the acidic electrolytes, Ti, Au, Pt, stainless steel, etc. were used as substrates. Besides aqueous solutions, Bi-Te based thermoelectric materials can also be electrodeposited from choline chloride based deep-eutectic solvents [43, 44, 45] and organic solvents, e.g. dimethyl sulfoxide (DMSO) and ethylene glycol [46, 47, 48, 49]. Compared to aqueous solutions, Te(IV) ions have much higher solubilities in deep eutectic and organic solvents. Thanks to the high concentrations of metal ions in the solution, higher current densities can be obtained. Nguyen *et al.* reported a current density of -5 A dm^{-2} from an ethylene glycol solution containing 1 M $Bi(NO_3)_3$ and $TeCl_4$ [49].

1.1.4 A short summary

The thermoelectric effects, thermoelectric materials and the electrochemically preparation of bismuth tellurium based thin films are briefly introduced in

this chapter. The efficiency of thermoelectric materials is a key point for the application. Compared with metals and insulators, semiconductors have the best thermoelectric performance. Bismuth telluride and their derived alloys have the best thermoelectric performance at room temperature. Bismuth tellurium thin films can be prepared by electrodeposition. To have higher ion solubility, organic solvents are preferred over aqueous solutions.

1.2 Germanium

1.2.1 Germanium and its applications

Germanium is a group IV semiconductor. The existence of this element was predicted by Dmitri Mendeleev in 1869. He predicted it had similar property as silicon and called it "ekasilicon". He also predicted its atomic mass of 72 which was very close to the actual value of 72.6. After 17 year, germanium was finally discovered by Clemens Winkler. Germanium has a shiny grey luster. After exposing to air, the surface becomes dull due to the formation of germanium dioxide. Like other semiconductors germanium is brittle at room temperature. At temperatures above 450 °C, germanium becomes increasingly ductile [50, 51] This unique mechanical property is due to the diamond cubic structure of germanium. Every germanium atom connects with the four nearest neighbors with covalent bonds. The defects have a high frictional resistance in shearing the covalent bond and also the dislocation energy is relative high [50]. Therefore, it is rather easy to grow low-dislocation density or even dislocation-free germanium crystals.

Germanium is the 52nd most abundant element in earth's crust ($\sim$ 1.7 ppm) and widely distributed [52, 53]. There is no native metal or real germanium minerals in nature. However, some minerals contain small amounts of germanium. Germanium is mostly found in zinc sulfide minerals and most of it is a byproduct of zinc smelting [54]. Table 1.1 lists the worldwide suppliers of germanium. Belgium is one of the largest germanium exportation countries. In 2006 and 2007, more than 40% (gross weight) of germanium that was imported in the U.S. was from Belgium [55].

Germanium was used in the first semiconductor transistor in 1948 because the best crystalline quality can be achieved for germanium at that time. However, silicon quickly took over the role of germanium in transistors because of its low cost, less leakage, etc. As shown in Figure 1.8, in 1980, 25% germanium was used in semiconductors, but the share rapidly decreased to 10% in 1990 and 0% in 2000. Since the new century, germanium has been revived as an

Table 1.1: Germanium suppliers [56]

Country	Company	Product
Belgium	N.V. Umicore S.A.	Ge
Canada	Argento Plata Metals Ltd. (ON)	Ge
	Teck Cominco Metals Ltd. (BC)	GeO_2
China	Beijing Transistor Material Works	Ge & GeO_2
	Emei Semi-Conductor Materials Factory	Ge & GeO_2
	General Research Institute for Non-Ferrous Metals	Ge
	Huidong Lead-Zinc Mine	Ge
	Shanghai Copper & Lead Refinery	Ge
	Shanghai Smelter	Ge
	Shaoguan Smelter	Ge
	Tianjin Semiconductor Material Plant	Ge & GeO_2
	Yunnan Huize Lead-Zinc Mine	Ge
France	Metaleurop SA	Ge
Germany	Metaleurop GmbH	Ge
	PPM Pure Metals GmbH	Ge & GeO_2
	Rhur-Zink GmbH	Ge
Russia	Krasnoyarsk Non-ferrous Plant	Ge
	Mednogorsk Copper & Sulphur Works	Ge conc.
Spain	Asturiana de Zinc SA (parent–Xstrata plc)	GeO_2
Ukraine	Zaporozhye Titanium & Magnesium Works	Ge & GeO_2
United Kingdom	Meldform Metals Ltd.	Ge & GeO_2
United States	Eagle-Picher Industries (OH)	Ge
	Germanium Corp. America (parent–Indium Corp.)	Ge
	Resources Alloys & Metal Inc. (MI)	Ge

Source: Non-Ferrous Metal Works of the World (Metal Bulletin), Roskill Publications.

electronic material [54]. Transistors composed of ultra thin epitaxial germanium on silicon are five times faster than comparable silicon transistors [54]. Single crystal germanium, mostly prepared by the Czochralski (Cz) technique, is used as substrate for epitaxial deposition of group III-V alloys. They can be used in light-emitting diodes (LED), laser diodes and photovoltaic solar cells [54].

Nowadays, fiber optics is one of the most important applications of germanium. Fiber optics had a rapid growth in 1990s. Until 2000, 50% of the consumption of germanium in the U.S. was used for fiber optics. Among all kinds of optical fibers, silica glass doped with less than 4 wt.% germanium oxide is the most important commercial one because of its transparency to near-infrared radiation, high refractive index and low chromatic dispersion [54]. Because germanium and germanium oxide are transparent at near-infrared radiation, they are applied in infrared optical systems for thermal imaging, night vision goggles, infrared laser, etc.

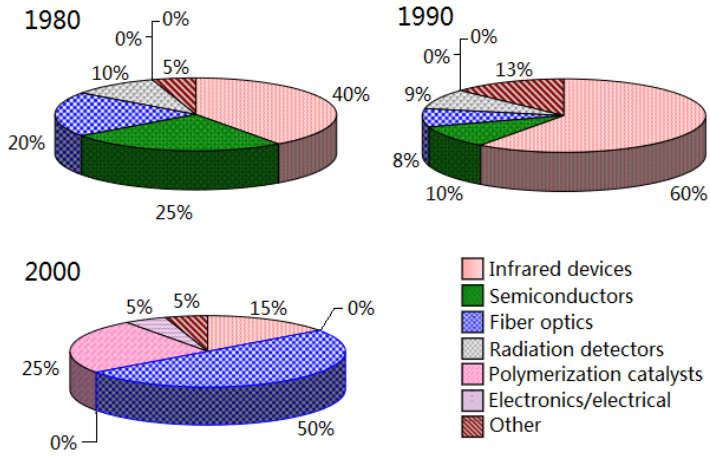

Figure 1.8: Share of germanium use in different applications in the U.S. Data from the U.S. Bureau of Mines, 1980, 1990; U.S. Geological Survey, 2000 (reprinted from [54]).

The use of germanium compounds as polycondensation catalyst is another important application of germanium compounds. Germanium dioxide is a catalyst for the polymerization of polyethylene terephthalate (PET) and it yields products with better transparency and whiteness than other catalysts [54]. However this kind of use has not been reported until late 1990s. In 2000, 25% of germanium was used as catalyst for polymerization in the U.S.

Germanium is also alloyed with other elements for various uses. For example, germanium-silicon alloys are used in thermoelectric devices [57], germanium-antimony-tellurium ternary alloy is a phase change material which is used in rewriteable data storage [58]. Niobium-germanium alloy is a superconductor up to 23 K [59]. Germanium can also be used as the anode in lithium ion batteries [60, 61].

1.2.2 Electrodeposition of germanium

Electrodeposit from aqueous electrolytes Nowadays, zinc ores are one of the main sources for the industrial production of germanium. However back to 1920s, germanium was first attracting attention in electrometallurgy because it was a harmful element in the electrowinning of zinc [62]. Electrowinning of germanium from molten salts was reported by Jaffee *et al.* in 1946 [63] Electrodeposition of germanium from an alkaline solution was first reported by Hall and Koenig in

1934 [64]. Germanium dioxide was dissolved in 3 M KOH. Electrodeposition ceased after formation of an ultra thin but shiny germanium layer on a copper substrate. This is because the overpotential for hydrogen evolution is very low on germanium and the reduction of water took place as a layer of germanium formed on the cathode. They tried to improve the electrolyte with additional potassium salts or even substitute KOH with other alkalies, but still only ultra thin germanium films were obtained. Other researchers used GeS_2 instead of GeO_2, but they also obtained only very thin germanium films as well. Attempts were made in acidic solutions in order to have higher germanium solubility. As expected, only very thin germanium films were obtained.

Very recently, Maldonado and co-workers used an electrochemical liquid-liquid-solid (ec-LLS) process to achieve the continuous deposition of germanium from an aqueous solution of pH 8.5 with dissolved GeO_2 [65]. A mercury (Hg) pool electrode was used as the cathode because it is much less electroactive for hydrogen evolution. The authors defined three steps for the deposition of germanium. The first step is reduction of $HGeO_3^-$ to Ge(0) on the Hg electrode:

$$HGeO_3^-(aq) + 4e^- + 2H_2O(l) \rightarrow Ge(s) + 5OH^-(aq) \tag{1.11}$$

This Ge(0) dissolved in the Hg as an amalgam. Thanks to the low solubility ($2.7\ 10^{-4}$ at.% at 298 K [66]) and diffusivity of germanium in mercury, as more germanium was reduced, it precipitated due to the supersaturation of the germanium amalgam near the Hg-electrolyte interface. The electrodeposited germanium was nanocrystalline with an average size between 8 nm and 53 nm depending on the applied potential. The crystal size was smaller at more negative potentials. The deposited germanium was free of residual impurities except for oxygen. They also used gallium as the working electrode and successfully deposited germanium crystals. Template-free germanium nanowires can be successfully electrodeposited from the solutions containing GeO_2 and $Na_2B_4O_7$ [67]. Discrete indium (In) nanoparticles were dispersed on either n-type silicon or a copper substrate. Although the melting point of bulk indium is 157 °C, the melting point of small indium nanoparticles is below 100 °C. At room temperature In-Ge nanoparticles show liquid properties. Polycrystalline germanium nanowires grew on top of the indium nanoparticles. The density of germanium nanowires increased as more indium nanoparticles were placed on the substrate. Single crystalline germanium nanowires also can be electrodeposited from the aqueous solution using the so-called electrochemical Liquid-Liquid-Solid (ec-LLS) process [68]. Liquid gallium (Ga) nanodroplets were placed on a single crystalline germanium or silicon substrate. Germanium nanowires were epitaxially electrodeposited under the gallium nanodroplets. The gallium nanodroplets stayed affixed to the tip of the nanowires. In aqueous solutions, a carbon anode was used. Germanium is not suitable to work as the anode

in aqueous solutions, because germanium anodically oxidizes and forms an oxidation layer that delaminated from the germanium [62].

Besides the deposition of pure germanium film, also the germanium alloys like copper-germanium and silver-germanium were studied in the past [62, 69]. Unlike the deposition of pure germanium film that can only be obtained as very thin layers, thick layers can be electrodeposited which can be because the hydrogen overpotential increases on those alloy surfaces and also the shift of deposition potential of germanium in the alloy due to the enthalpy of formation of these alloys..

Electrodeposition from organic solvents To avoid the severe hydrogen evolution on the deposited germanium surfaces, organic solvents were investigated as the electrolytes for germanium deposition. Shiny germanium films can be electrodeposited from ethylene glycol, diethylene glycol, 1,3-propanediol, propylene glycol and glycerol containing dissolved germanium halide [70, 71, 62]. Szekely studied the electrodeposition of germanium from ethylene glycol and propylene glycol containing germanium tetrachloride ($GeCl_4$) [72]. $GeCl_4$ has a very high solubility in ethylene glycol up to 10 vol%. Electrodeposition was performed from the solutions containing 0.5 vol% to 3.8 vol% $GeCl_4$ and the cathodic current efficiency increased from 0.17% to 0.54%. Germanium films could be obtained from all those solutions, but the films deposited from the solution with higher concentration of $GeCl_4$ were brighter. The effects of current density and working temperature were also studied. In generally, brighter films could be obtained at higher applied current density up to -50 A dm^{-2}. At about 80 °C, although bright germanium films could be electrodeposited, the surfaces were rougher than those from lower temperatures. Introducing agitation during electrodeposition improved the film morphology. Ethylene glycol is hydrophilic and it absorbs water from the atmosphere. Water in the solution also has an effect on the deposition. In solution containing 1.3 g L^{-1} water, black, smutty germanium was obtained. Ethylene glycol was dried using vacuum distillation and a bright metallic-look germanium film could be obtained from it. The current efficiency also increased as less water was present in the solution. In propylene glycol solutions, the electrodeposition behavior was similar to the deposition behavior in ethylene glycol solutions. Perfect mirror-like germanium film was obtained at current density of -40 A dm^{-2} from the propylene glycol containing 7 vol% $GeCl_4$ at 59 °C. This is also the optimum deposition conditions suggested by Szekely. The highest current efficiency of 0.877% was obtained in solution containing 5 vol% $GeCl_4$. Germanium anodes worked good in ethylene glycol solutions. But in propylene glycol solutions, the anodic efficiency was much higher on the germanium anode than the cathodic efficiency resulting in the precipitation of

the germanium compound during deposition. To avoid that problem, graphite was used as anode. Huang *et al.* electrodeposited amorphous germanium on n-type silicon and highly doped p-type silicon substrates in 0.5 M $GeCl_4$ in 1,3-propanediol [71]. Post deposition annealing was carried out at 400 °C for 2 h in forming gas and single crystalline germanium film formed. To be noticed here, the cleanliness of the silicon substrate is crucial to the germanium epitaxy. The efficiency was 0.3% which was also very low. Huang attributed this to the hydrogen evolution on the germanium surface.

Another interesting case is the anodic electrodeposition of germanium films [70]. Chandrasekharan *et al.* prepared Zintl phase K_4Ge_9 as the precursor compound and dissolved it in ethylenediamine. Electrodeposition was performed in a two electrode cell. The working electrode was boron-doped silicon and a copper wire was used as the counter electrode. Different current densities up to 0.3 A dm^{-2} and different potentials up to 100 V were applied and highest current efficiency of 73% was achieved. The efficiencies obtained from this work were 2 orders of magnitude higher than the efficiencies of cathodic deposition. This is because there were less side reaction on the anode than on the cathode. They electrodeposited germanium contained some oxides which were most likely due to the oxidation of negatively charged germanium species. The as-deposited germanium was amorphous.

Jawad *et al.* proposed an alternative method to deposit germanium [73]. They first electrochemically dissolved germanium metal in a 1:4 HF (49%):ethanol (95%) mixture and then electrodeposited germanium on a silicon cathode. Unlike the deposition from aqueous solutions, thick layers up to 3 µm could be obtained. Unlike the films obtained from organic solvents, the deposited germanium was crystalline. A current efficiency of 94% was reported.

Electrodeposition from ionic liquids Germanium can be electrodeposited from aqueous and organic electrolytes but the current efficiency is extremely low because of the hydrogen evolution during electrodeposition. Ionic liquids, which are also known as room temperature molten salts, are solvents that consist entirely of ions. One of the advantages of this kind of solvent is that water can be easily removed. They also have a wide electrochemical window and an intrinsic ionic conductivity [74, 75]. The vapor pressure of ionic liquids is very low which makes it possible to work even under vacuum [76, 77, 78]. However, they have a high viscosity that can range from 0.022–40 Pa s and are more expensive than organic solvents [75]. Using ionic liquids as electrolytes and performing electrodeposition from ionic liquids have been a hot research topic during the last decade. Some metals that are impossible to deposit from water due to the fact that hydrogen evolution happens before metal ion reduction,

can be electrodeposited from ionic liquids [79].

Endres and coworkers first reported on germanium electrodeposition from the ionic liquid 1-butyl-3-methylimidazolium hexafluorophosphate ([BMIM][PF_6]) using germanium(IV) halides as germanium source [80, 81, 82, 83]. They started with the least volatile compound GeI_4 which is however only slightly soluble in [BMP][PF_6] [80]. At the early stage of the deposition, germanium nanoclusters were formed and then transformed into bilayer structure with a GeX_3 (X=I, H, F, OH) layer on top. Germanium films with a maximum thickness of 20 nm were deposited from solutions containing 0.1 mM to 1 mM GeI_4. To increase the germanium concentration in the solution, $GeBr_4$ was used and 0.5 M $GeBr_4$ could be dissolved in [BMIM][PF_6] [82]. The cyclic voltammogram indicated the reduction of germanium happens in two steps: Ge(IV) was first reduced to Ge(II) at the first reduction peak and then Ge(II) was further reduced to Ge(0) at more negative potentials. The reduction processes were irreversible. However the in situ scanning tunneling microscope (STM) showed the Au working electrode was already remarkably rough at potentials more positive than the potential for deposition of germanium. At the beginning a thin layer with rather metallic behavior formed on the Au working electrode followed by the bulk deposition. The bulk deposition of germanium started with formation of nanoclusters. And the thick films were like coherent nanosized wires growing from the substrate towards the solution.

As a system, they studied the electrodeposition with $GeCl_4$ [81]. The electrochemical behavior and the mechanism of the germanium growth were very similar to the solution using $GeBr_4$. They also confirmed that at the first reduction peak germanium islands formed. This underpotential deposition of germanium was demonstrated with spectroscopic analysis in their later work [84]. Other ionic liquids were tested for germanium deposition in their goup, e.g. 1-butyl-3-methylimidazolium bis(trifluoromethylsulfonyl)imide, 1-butyl-1-methylpyrrolidinium bis(trifluoromethylsulfonyl)imide, 1-ethyl-2,3-dimethylimidazolium bis(trifluoromethylsulfonyl)imide [85, 86, 87]. The change of ionic liquids did not show a clear effect on the electrodeposition. Now bis(trifluoromethylsulfonyl)imide $[Tf_2N]^-$ based ionic liquids are preferred to $[PF_6]^-$ because $[PF_6]^-$ is very sensitive to water which causes the decomposition of the anion. The films deposited from ionic liquids with germanium halides were amorphous and impurities of halides and oxygen, etc. were found. They attributed the halides impurity to a GeX_3 termination and oxygen to the oxidation in the air [83]. The germanium layers deposited from [BMIM][PF_6] containing either $GeBr_4$ or $GeCl_4$ had a band gap of about 0.7 ± 0.1 eV which is close to the value for intrinsic bulk germanium. An interesting phenomenon was observed that the deposited germanium films were attacked by the solutions. Endres claimed in their earlier studies that the the germanium film was attacked

by $GeBr_4$ or $GeCl_4$ in the solution in their early studies. But later, they tried to experimentally convince the readers that the dissolution of deposited germanium film was due to the decomposition products of $[Tf_2N]^-$ anions [88]. They also found the dissolution of the film in the electrolyte without applying any current through but the dissolution rate was much slower. It must be mentioned that in their early studies they found the dissolution of germanium films deposition from ionic liquid [BMP][PF_6] which does not contain $[Tf_2N]^-$ anions, but the attack of deposited germanium was also observed and described. The reason for the dissolution of the deposited germanium is not well defined yet.

Because germanium is a semiconductor, the introduction of light should have an influence on the electrochemical behavior. Endres and coworkers performed cyclic voltammetry and electrodeposition under 254 nm and 365 nm UV light [89, 84]. The reduction potential shifted to a more positive value as UV light with smaller wavelength was applied. They also found the UV light has an influence on the film morphology: the cluster formation was less in the presence of UV lights. Germanium deposition was also performed on different templates in order to obtain certain morphologies or properties. Meng *et al.* prepared three-dimensionally ordered macroporous (3DOM) nanostructures on indium tin oxide (ITO) glasses and showed various optical colors by changing the angle of incidece light [90]. Amorphous germanium nanowires were also successfully electrodeposited with the help of nanoporous polycarbonate (PC) membranes [86]. Liu *et al.* found it was possible to deposit germanium nanotubes using PC membranes with large hole diameter up to 400 nm [91]. Generally speaking, there are four key parameters that determine the formation of germanium nanotubes instead of nanowires: (1) pore size of the template, large pore diameter is essential for obtaining nanotubes; (2) applied current, higher current density is preferred for nanotubes; (3) the concentration of $GeCl_4$, high concentration is required; and (4) deposition time, as the previous three conditions are achieved, nanotubes form at the beginning, but after a short time, germanium grows along the inner wall of the PC membrane.

Electrodeposition from supercritical fluids A substance that exits above its critical temperature and critical pressure is called a supercritical fluid. It has the properties of both a liquid and a gas. Compared with other solvents, supercritical fluids have low viscosity that can provide better mass transport. They can easily penetrate nanoporous template structures. Ke *et al.* studied electrodeposition of germanium from liquid CH_3CN and CH_2F_2 in $scCO_2$ containing CH_3CN and CH_2F_2 with $GeCl_4$ and $[NBu_4^n][GeCl_3]$. Bulk amorphous germanium could be electrodeposited [92]. High pressure electrochemical cells have to be used for these kind of solutions.

1.2.3 A short summary

In this chapter, the history and applications of germanium were introduced. A comprehensive literature survey on electrodeposition of germanium around room temperatures has been covered in this chapter. Due to the hydrogen evolution on the germanium surface, only very thin germanium films or very low current efficiency could be obtained in aqueous or organic solutions. Ionic liquids were used for germanium deposition because high solubility of germanium compound and low water content. Black germanium films were always obtained and oxygen, chlorine and carbon impurities were present in the films.

1.3 General introduction of semiconductor electrochemistry

Electrodeposition has become a mature technology during the first half of the 20th century. At that time, the interest was mostly in electrodeposition of metals and metal alloys for surface treatment. Thanks to the development of semiconductors and their use in electronics, electrodeposition of semiconductors become a topic of interest during the second half of the 20th century. Bismuth telluride and germanium are both semiconductors. Although the band gap of bismuth telluride is only 0.16 eV and it has similar behavior as metals or semi-metals during electrodeposition, bear in mind that the electrochemical behavior of semiconductor materials is not the same as metals. It is logical to have a general view of semiconductor electrochemistry before presenting the results of electrodeposition of semiconduction. A brief introduction of semiconductor electrochemistry is presented in this section.[1]

1.3.1 Metal-semiconductor interface

Unlike metals which have high electrical conductivity due to the overlapping of valance bands and conduction bands, there is a band gap ($E_{\text{g}} < 4$ eV) between the valance bands and conduction bands in semiconductors. Intrinsic semiconductors which are impurity-free materials exhibit a very low electrical conductivity due to the low carrier density. The density of electrons n in the conduction band and the density of holes p in the conduction band are given

[1] In this section, U stands for electric voltage and E stands for electron energy. In other chapters E stands for electric voltage.

by:

$$n = N_{\mathrm{c}} \exp\left[-\frac{(E_{\mathrm{c}} - E_{\mathrm{F}})}{\mathrm{k}T}\right] \tag{1.12}$$

$$p = N_{\mathrm{v}} \exp\left[-\frac{(E_{\mathrm{F}} - E_{\mathrm{v}})}{\mathrm{k}T}\right] \tag{1.13}$$

where N_{c} and N_{v} are the effective density of states in the conduction band and valence band, respectively, E_{c} is the minimum conduction band energy, E_{v} is the maximum valence band energy, E_{F} is the Fermi energy which means at this energy level there is 50% probability of getting occupied by an electron at any temperature and k is the Boltzmann constant [8.6 10^{-5} eV K^{-1}]. For a band gap of 1 eV, the carrier density of an intrinsic semiconductor is only about 10^{11} cm^{-3} which is very small compared to the carrier density in metals which is around 10^{22} cm^{-3} [93]. The Fermi level (E_{F}) of an intrinsic semiconductor is located near the middle of the band gap. Semiconductors can be easily doped with donor or acceptor impurities. Semiconductors with donor impurities are n-type and the Fermi level is located at the upper half of the band gap. Semiconductors with acceptors are p-type and the Fermi level is at the lower half of the band gap. The band diagrams of metal and n- and p-doped semiconductors are shown in Figure 1.9. The Fermi energy can be determined by the work function Φ. In a metal, the work function is identical to the ionization energy I which is the energy required to remove an electron from the material to the vacuum level and the electron affinity χ which is the energy gained when an electron is transferred from the vacuum into the material. In a semiconduction, the ionization energy is not the same as the electron affinity. The ionization energy is the energy required to excite an electron from the valence band to the vacuum and the electron affinity is the energy gained when an electron transfer from the vacuum to the conduction band [93]. In a vacuum, the electron energy is zero which is taken as a reference here. The bands of the semiconductor can be considered to be flat by assuming the semiconductor is free from surface states. When a semiconductor contacts a metal, the Fermi level has to coincide in these two materials at thermal equilibrium.

If the work function of a metal Φ_{m} is larger than the work function Φ_{s} of semiconductor, after contacting, electrons are transferred from the semiconductor to the metal leading to a positive space charge region inside the semiconductor next to the metal-semiconductor interface. This layer is also known as the depletion layer. A metal in contact with a semi-conductor can form a Schottky junction as shown in Figure 1.10a. The barrier height Φ_{b} is the difference between the work function of the metal Φ_{m} and the electron affinity of the semiconductor χ [93]:

$$\Phi_{\mathrm{b}}(\mathrm{n}) = \Phi_{\mathrm{m}} - \chi \tag{1.14}$$

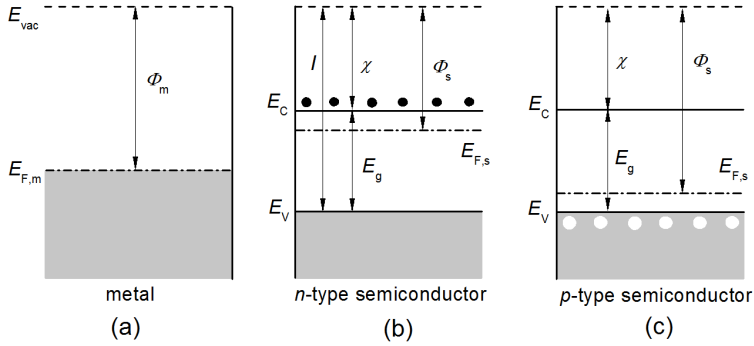

Figure 1.9: Band diagram of metals and semiconductors.

and the energy across the space charge region is:

$$\Phi_{\mathrm{sc}} = \Phi_{\mathrm{b}} - (E_{\mathrm{c}} - E_{\mathrm{F}}) \tag{1.15}$$

p-Type semiconductors normally have larger work functions than the work functions of metals. A negative space charge region is formed inside the p-type semiconductors. The barrier height is given by [93]:

$$\Phi_{\mathrm{b}}(\mathrm{p}) = E_{\mathrm{g}} - (\Phi_{\mathrm{m}} - \chi) \tag{1.16}$$

Only the electrons that have sufficient energies to overcome the barrier can move through the junction and the current depends on the concentration of those electrons. If there is no external voltage applied ($U = 0$), an energy of at least $E_{\mathrm{F}} + \Phi_{\mathrm{b}}$ is required for an electron to cross the Schottky barrier which is composed with an n-type semiconductor and a metal [93]. Those electrons with sufficient energy to cross the barrier generate a very small current density from metal to the semiconductor $j_{\mathrm{s}\to\mathrm{m}}$ and a very small current density from semiconductor to metal $j_{\mathrm{s}\to\mathrm{m}}$, but the total current density must be zero at $U = 0$. Therefore

$$|j_{\mathrm{s}\to\mathrm{m}}| = |j_{\mathrm{s}\to\mathrm{m}}| = j_0 = \frac{4\pi e m^{\star} \mathrm{k} T}{\mathrm{h}^3} T^2 \exp\left(-\frac{\Phi_{\mathrm{b}}}{\mathrm{k}T}\right) \tag{1.17}$$

where k is the Boltzmann constant [8.6 10^{-5} eV K^{-1}].

When a forward bias, which is a negative voltage on the semiconductor in this case, is applied to the semiconductor, the barrier for the electrons in the conduction band becomes smaller and electrons with lower energies can also transfer into the metal (Figure 1.10b). The current increases exponentially with

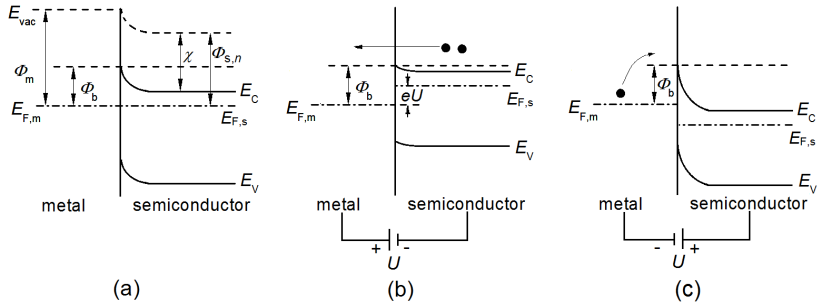

Figure 1.10: Band diagram of n-type semiconductor-metal interface.

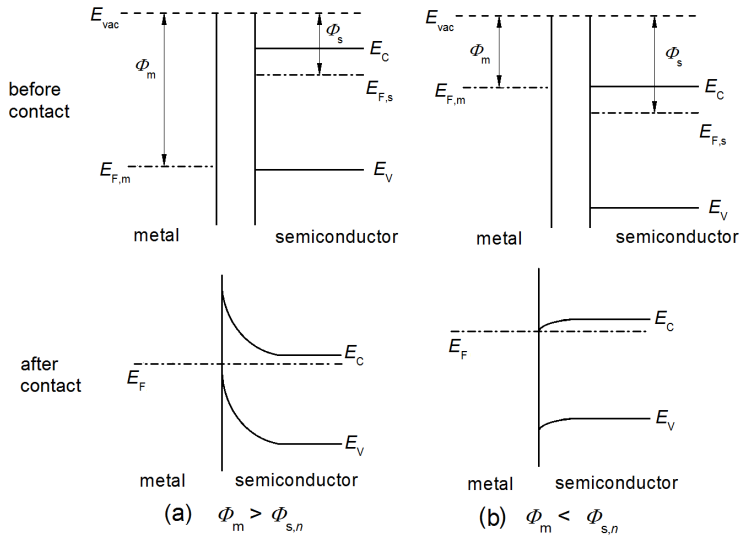

Figure 1.11: Band diagram of metal-semiconductor interface.

the applied voltage:

$$j = j_0 \left[\exp\left(\frac{eU}{kT}\right) - 1 \right] \tag{1.18}$$

Under reverse bias, i.e. when a negative voltage is applied to the metal with respect to the semiconductor, the barrier height remains constant. The electrons are blocked in the metal and only electrons with energies larger than the barrier energy can enter the semiconductor (Figure 1.10c). As a result, there is only a very small leakage current $j_{\mathrm{m}\to\mathrm{s}} = j_0$ under reverse bias.

If the work function of the metal is much higher than the work function of the semiconductor, the barrier height can be close to value of the band gap. The space charge region is called inversion layer in this case (Figure 1.11a). Under forward bias, not only electrons can move across the junction, minority hole carriers can also be injected in the semiconductor and recombine with electrons in the bulk. The current contributed by the hole injection depends on the carrier density, diffusion constant and diffusion length.

When the work function of the metal is smaller than that of the semiconductor, electrons are transferred from the metal to the semiconductor leading to a negative space charge region. This is called accumulation region in semiconductors (Figure 1.11b). In this case, metal and semiconductor form a barrier-less contact known as ohmic contact. If we want to study the electrochemical reactions on the semiconductor electrode, it is important for the semiconductor electrodes forming an ohmic contact to the current-carrying cables to ensure both cathodic and anodic current can flow to the semiconductor-electrolyte interface [93].

1.3.2 Semiconductor-electrolyte interface

Before discussing the semiconductor-electrolyte interface, the Fermi level of a redox system has to be defined. The chemical potential of a species in an ideal solution depends on its concentration c_i:

$$\mu_\mathrm{i} = \mu_\mathrm{i}^0 + \mathrm{k_B} T \mathrm{N_A} \ln \frac{c_\mathrm{i}}{c_\mathrm{i}^0} \tag{1.19}$$

where $\mathrm{N_A}$ is the Avogadro constant, μ^0 is the standard chemical potential, $\mathrm{k_B}$ is the Boltzmann constant [1.38 10^{-23} J K^{-1}] and c_i^0 is 1 M. For a charged species the electrochemical potential $\bar{\mu}_\mathrm{i}$ of a species i is defined as the sum of the chemical potential of that species plus the electrostatic energy to bring that species to an electric potential Ψ:

$$\bar{\mu}_\mathrm{i} = \mu_\mathrm{i} + z_\mathrm{i} \mathrm{e} \mathrm{N_A} \Psi \tag{1.20}$$

where z_i is the charge number of the species and Ψ is potential (V) which only depends on the large-scale environment of a given phase. In a solution containing a redox couple, oxidant (Ox) can be reduced to reductant (Red):

$$\mathrm{Ox} + \mathrm{e}^- \rightleftharpoons \mathrm{Red} \tag{1.21}$$

The electrochemical potential of the electron in this redox system is given by:

$$\overline{\mu}_{\mathrm{e,redox}} = \overline{\mu}_{\mathrm{Red}} - \overline{\mu}_{\mathrm{Ox}} \tag{1.22}$$

$$= \mu^0_{\mathrm{Red}} - \mu^0_{\mathrm{Ox}} - \mathrm{k_B}T\mathrm{N_A}\ln\frac{c_{\mathrm{Ox}}}{c_{\mathrm{Red}}} - \mathrm{eN_A}\Psi^{\mathrm{sol}} \tag{1.23}$$

$$= \overline{\mu}^0_{\mathrm{e,redox}} - \mathrm{k_B}T\mathrm{N_A}\ln\frac{c_{\mathrm{Ox}}}{c_{\mathrm{Red}}} \tag{1.24}$$

The Fermi level of a redox system $E_{\mathrm{F,redox}}$ is equivalent to the electrochemical potential of the electrons ($\bar{\mu}_{\mathrm{e,redox}}$) in the solution. The electron energies of a redox system is shown in Figure 1.12a. The electron energy E^0_{Red} is actually an ionization energy I because electrons are removed from reductant and the E^0_{Ox} is the electron affinity χ because the oxidant gain electrons. In a metal, the ionization energy is identical to the electron affinity. However, these two are not the same for a redox couple in an electrolyte:

$$I - \chi = E^0_{\mathrm{Ox}} - E^0_{\mathrm{Red}} = 2\lambda \tag{1.25}$$

where λ is reorganization energy which is introduced by reorganization of solvation layer around the ions. The ions in the electrolyte are solvated and the solvation layers around the reductant and oxidant are different. For example, a reductant M^z is surrounded by a solvation shell typical for reducing agent. After extraction of an electron from it, it becomes an oxidant M^{z+1} but it is still surrounded by the solvation shell for M^z. To obtain the equilibrium state for M^{z+1}, the solvation shell has to be rearranged which requires an energy λ. Due to the thermal fluctuations of the solvation shell of Red and Ox, the energy of the electron levels of them are not fixed leading to a broadening of the electronic levels (Figure 1.12b).

When a semiconductor electrode is in contact with an electrolyte, a movement of charge at the interface is required to establish equilibrium between the semiconductor electrode and the electrolyte. This behavior is similar to the metal-semiconductor contact. n-Type semiconductors normally have higher Fermi levels than that of the electrolyte. Therefore, the electrons move from the semiconductor to the electrolyte leaving a positive charge space region close to the interface. At equilibrium (no external potential is applied), the electrode potential $\mathrm{e}U_{\mathrm{E}}$ which is measured with respect to a reference electrode is the same as the energy difference between the Fermi level and the reference electrode (Figure 1.13a). By applying a cathodic potential to the semiconductor electrode, the Fermi level of the semiconductor moves up. As shown in Figure 1.13b, the change of the potential on the electrode $\mathrm{e}\Delta U$ is the same as the change of the potential across the space charge layer Φ_{sc}. At a certain electrode potential,

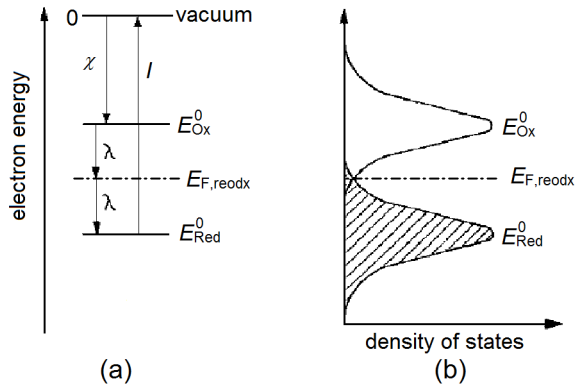

Figure 1.12: The electron energies of a redox system (adapted from [93]).

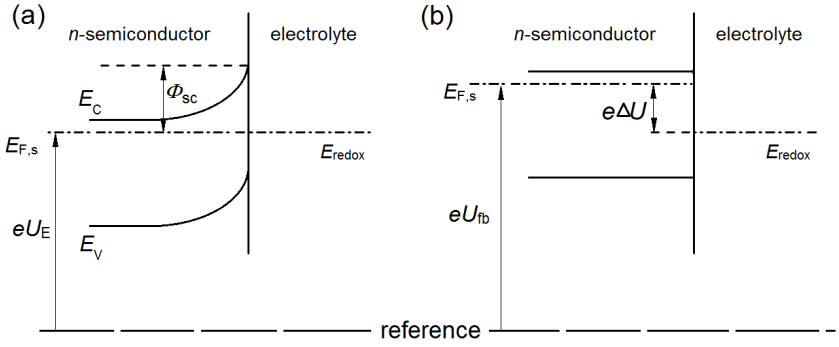

Figure 1.13: Energy scheme of an n-type semiconductor-electrolyte interface: (a) at equilibrium and (b) under flatband condition.

the conduction band and valence band of the semiconductor electrode become flat. That potential is called flatband voltage U_{fb}. The flatband voltage can be experimentally obtained using capacitance-voltage measurements. Knowing the flatband potential, the position of Fermi energy level and band energy can be located in a potential scale with respect to a reference electrode, e.g. normal hydrogen electrode (NHE) or saturated calomel electrode (SCE), and become comparable with redox potentials of elements.

The charge transfer across the interface can only go through the valence band or conduction band because there are no electron levels within the band gap. Therefore there are four electron transfer mechanisms:

electron capture: electrons transfer from the conduction band to the oxidant:

$$\mathrm{Ox} + \mathrm{e}^- \rightarrow \mathrm{Red}; \tag{1.26}$$

The rate of electron capture depends on the density of free electrons at the semiconductor surface n_s. When a cathodic bias is applied, the cathodic current increases exponentially with the applied voltage (U), the corresponding cathodic current density is given by:

$$j_\mathrm{c}^- = -\mathrm{F}k_\mathrm{c}^\mathrm{Ox} n_\mathrm{s} c_\mathrm{Ox} \tag{1.27}$$

$$n_\mathrm{s} = n_0 \exp\left[-\frac{\mathrm{e}(U - U_\mathrm{fb})}{\mathrm{k}T}\right] \tag{1.28}$$

where k_c^Ox is the rate constant which depends on the density of unoccupied states of the oxidant, c_Ox is the concentration of oxidant at the surface, n_0 is the bulk electron density.

electron injection: electrons transfer from the reductant to the conduction band (not shown in the figure):

$$\mathrm{Red} \rightarrow \mathrm{Ox} + \mathrm{e}^-. \tag{1.29}$$

The corresponding anodic current is given by:

$$j_\mathrm{c}^+ = -\mathrm{F}k_\mathrm{c}^\mathrm{Red} c_\mathrm{Red} \tag{1.30}$$

where $k_\mathrm{c}^\mathrm{Red}$ is the rate constant which depends on the density of occupied states of the reductant.

hole injection: holes transfer from the oxidant to the valence band:

$$\mathrm{Ox} \rightarrow \mathrm{Red} + \mathrm{h}^+ \tag{1.31}$$

The corresponding cathodic current is given by:

$$j_\mathrm{v}^- = -z\mathrm{F}k_\mathrm{v}^\mathrm{Ox} c_\mathrm{Ox}. \tag{1.32}$$

where k_v^Ox is the rate constant which depends on the density of unoccupied states of the oxidant.

hole capture: holes transfer the valence band to the reductant:

$$\mathrm{Red} + \mathrm{h}^+ \rightarrow \mathrm{Ox} \tag{1.33}$$

The corresponding anodic current is given by:

$$j_\mathrm{v}^+ = -z\mathrm{F}k_\mathrm{v}^\mathrm{red} p_\mathrm{s} c_\mathrm{Red} \tag{1.34}$$

$$p_s = p_0 \exp\left[-\frac{e(U - U_{fb})}{kT}\right] \tag{1.35}$$

where k_v^{Red} is the rate constant depending on the density of occupied states of the reductant, p_s and p_0 are the electron density at the surface and in the bulk, respectively.

n-Type semiconductors normally form Schottky contacts with electrolytes because the Fermi levels of semiconductors are normally higher than the Fermi level of electrolytes. As shown in Figure 1.14a, when a cathodic voltage is applied, electron capture happens and the cathodic current increases exponentially with the applied voltage (equation 1.27 and 1.28). When an anodic voltage is applied, a current is generated by the electron injection process. This current is independent of the applied voltage and is very small because the conduction band barely overlaps with the energy states of the reductant that few electrons have energy to transit to the conduction band of the semiconductor and thus a low anodic current is obtained (equation 1.30). If the Fermi level of the semiconductor electrode is much higher than the redox potential of the electrolyte, minority carrier process hole-injection also can occur. The current due to the hole injection is potential independent and it depends on the overlap of the valence band with the density of oxidant states.

p-Type semiconductors normally have lower Fermi levels compared to the Fermi levels of electrolytes. As shown in Figure 1.14b, when a cathodic voltage is applied, because the energy states of the oxidant barely overlaps with the valence band, very low cathodic current are obtained. When an anodic voltage is applied, anodic current due to the hole capture increases exponentially with the applied voltage. Electron injection is possible if the conduction band of the p-type semiconductor overlaps with the energy states of the reductant.

Electron capture and hole capture depend on the charge carrier concentration on the semiconductor surface (n_s and p_s). This prevents the electron capture process (cathodic reduction) in p-type semiconductor and hole capture (anodic oxidation) in n-type semiconductor in the dark [94]. The number of minority carriers can be enhanced by light excitation. A photon with energy $h\nu$ (where ν is the frequency) higher than the band gap E_g, can generate an electron-hole pair. Depending on the penetration depth of the incident light, the excitation of electron-hole pairs takes place near the surface. Not all of the excited minority carriers can contribute to the current. The minority carries formed in the depletion layer can be transferred across the interface and contribute to the photocurrent. And those formed outside of the depletion layer will move towards the interface. But due to the recombination with the majority carriers, not all of them can move into the depletion layer and contribute to the photocurrent. Figure 1.15 shows the theoretical i-V curves for an n-type electrode [93]. The

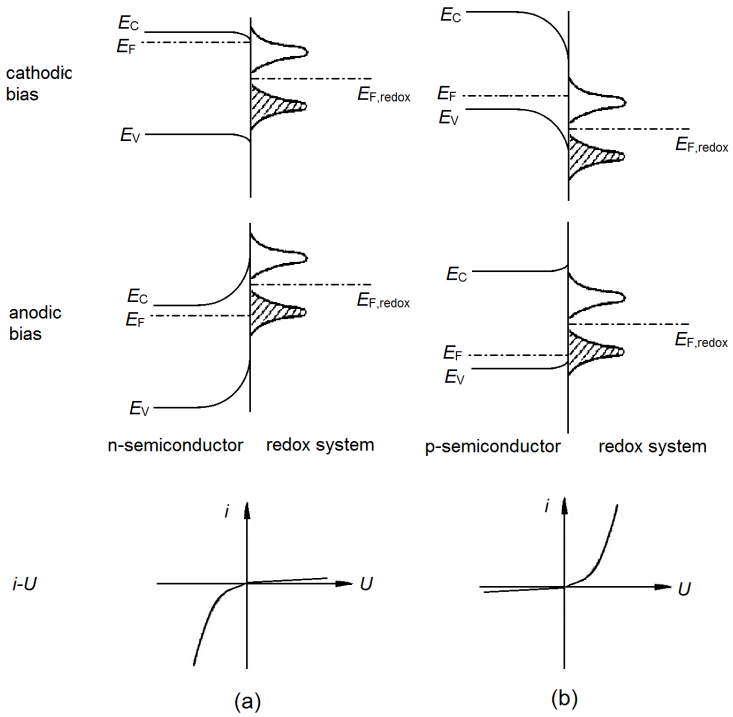

Figure 1.14: Energy diagram of the interface of semiconductor and redox system with different biases and the corresponding current.

photocurrent increases with the intensity of the incident light, but is independent of voltage.

1.3.3 Germanium electrode

Pure germanium is an intrinsic semiconductor with a band gap of 0.66 eV at room temperature. The band gap is a function of temperature and it decreases with temperature as:

$$E_g = 0.74 - 4.8 \times 10^{-4} T^2/(T + 235) \text{ eV} \tag{1.36}$$

where T is temperature (K). The carrier concentration in intrinsic germanium is only 2 10^{13} cm^{-3} which is about 9 orders of magnitude smaller than in a metal. Extrinsic germanium can be obtained by doping elements from group III and V mostly and other groups as well. n-Type germanium is normally doped

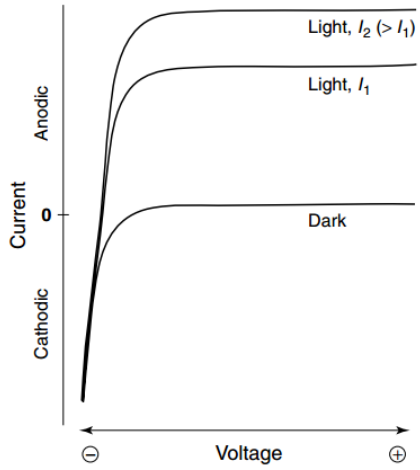

Figure 1.15: Theoretical curves of the current density change vs. applied potential on an n-type electrode in the dark and under illumination (reprinted from [95]).

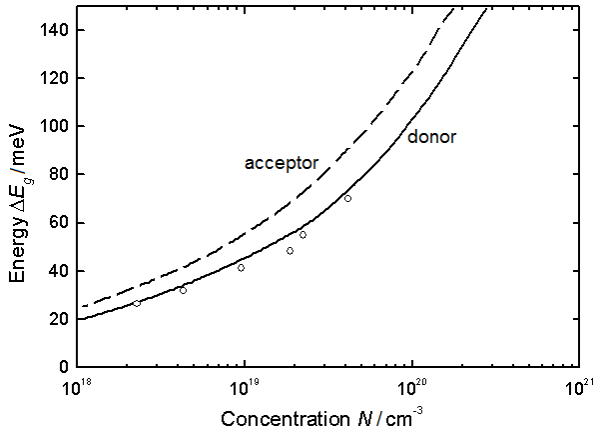

Figure 1.16: Band gap narrowing with the doping level, the open circles are experimental data (adapted from [96]).

with As, P, Sb, Bi or Li and p-type germanium contains acceptors like B, Al, Ga, In or Tl. As shown in Figure 1.16, the band gap become smaller with the doping level. The band gap is narrowed about ΔE_g 100 meV by doping 10^{20} cm^{-3} donor impurities [96].

Table 1.2: Barrier height of metal/n-Ge Schottky diode [101]

Metal	Pt	Hf	Ni	Ti	Ta	La	Gd	Ce
Φ_b / eV	0.64	0.58	0.58	0.57	0.51	0.51	0.49	0.49

The work function of germanium has been measured with different techniques. Dillon *et al.* obtained the work function of 4.5 eV for n-type germanium using the contact potential difference (CPD) between germanium and a gold reference [97]. This value is close to the value of 4.75 eV measured by Haneman and Apker *et al.* using potoelectric emission [98, 99]. Melnikov *et al.* computed the electron affinity of germanium which is 4.4 eV [100]. Germanium forms Schottky diodes with many metals and the barrier height with different metals are listed in Table 1.2 [101]. The barrier height of an n-type Ge/Pt contact is close to the band gap of germanium. This case is similar to the junction described in Figure 1.11a. Both majority and minority carriers contribute to the cathodic current, however there is almost no anodic current in the dark. The barrier height of p-Ge/Pt can be estimated based on equation 1.16, which is only about 0.02 eV. The contact between platinum and p-type germanium can be ohmic depending on the position of the Fermi level.

Figure 1.17 shows the relationship between the redox potentials of several redox couples and the valence band and conduction band of germanium. Please notice that the energy level of conduction and valence band depend on the pH of electrolyte, temperature, doping, illumination, etc. The band energy in the figure is estimated using the electron affinity of germanium. Ge^{4+}/Ge^{2+} has the same redox potential as H^+/H_2 which lies close to the conduction band of germanium.

1.4 Outline of the thesis

This PhD research was focused on the electrodeposition of germanium and bismuth telluride based alloys. The electrodeposition was carried out from non-aqueous solutions in order to prevent the problems introduced by hydrogen evolution such as low current efficiency and hydrogen embrittlement. Also, the solubility of bismuth and tellurium metal ions is much higher in organic solvents than in water so that long-term deposition with high current density can be achieved. Bismuth telluride is a thermoelectric material and to improve the thermoelectric performance, multilayers were prepared. This thesis contains 6 chapters.

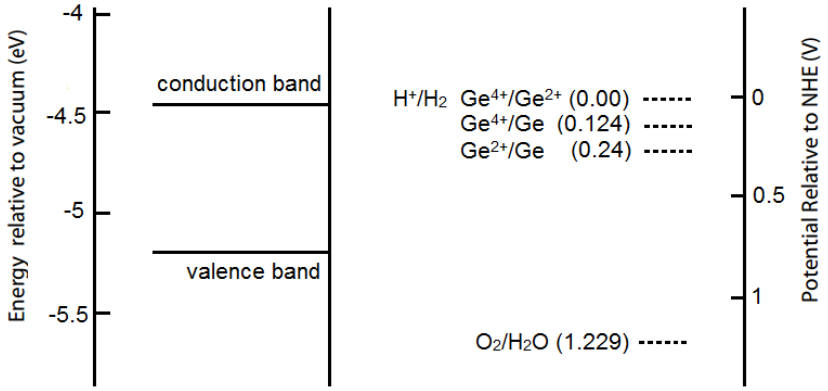

Figure 1.17: The valence and conduction band positions and redox potentials of water.

Chapter 2 reports the electrodeposition of bismuth telluride from a modified ethylene glycol solution in which chloride ions were removed by precipitation with silver ions. The electrochemical behavior of tellurium and bismuth in chloride-containing and chloride-free solutions was studied by means of cyclic voltammetry (CV), electrochemical quartz crystal microbalance (EQCM) and rotating disk electrode (RDE). The diffusion coefficients and kinetic parameters of bismuth and tellurium ions were measured in chloride-containing and chloride-free solutions. Bismuth-tellurium films were electrodeposited at different conditions to study the change of film composition as a function of deposition potential, rotation speed, bath composition and bath concentration. The electrodeposited films were characterized by scanning electron microscopy (SEM), energy-dispersive X-ray spectroscopy (EDX) and X-ray diffraction (XRD). The Seebeck coefficient of the films were measured.

Chapter 3 introduces the electrodeposition of $Bi_2Te_3/(Bi_{1-x}Sb_x)_2Te_3$ multilayers in order to reduce the thermal conductivity and increase the Seebeck coefficient. Chloride-free ethylene glycol solutions were used for this study. The electrochemical behavior of antimony in chloride-free ethylene glycol solutions was studied on both platinum and glassy carbon electrodes. The diffusion coefficient of antimony in chloride-free solution was calculated using Levich's equation. Electrodeposition of bismuth-antimony and antimony-tellurium alloys were studied using CV and thermodynamic calculations. The ternary alloys were electrodeposited at different potentials and rotation speeds to study the composition change. The deposited films were characterized with SEM, XRD and inductively coupled plasma optical emission spectroscopy (ICP-OES). Pulsed potential deposition was used to obtain multilayer structures. Chapter

4 reports the investigation of germanium deposition from ionic liquid 1-butyl-1-methylpyrrolidinium dicyanamide [BMP][DCA]. A new germanium compound $[GeCl_4(BuIm)_2]$ was and used. The electrochemical behavior of $[GeCl_4(BuIm)_2]$ in [BMP][DCA] was studied using CV and EQCM. The diffusion coefficient and kinetic paraments of germanium ions in that solution were obtained from the Koutecký-Levich equation. The electrodeposition of germanium was also studied in a mixture of [BMP][DCA] and [BMP]Cl in order to prevent the polymerization of $[DCA]^-$ anions. The electrodeposited germanium films were characterized by SEM and EDX.

Chapter 5 introduces the electrodeposition of germanium at elevated temperatures and pressures. In order to increase the deposition rate and improve the film morphology, the electrodeposition was performed at elevated temperatures up to 180 °C. A pressure cell was used to prevent the evaporation of $GeCl_4$. The electrochemical behavior of $GeCl_4$ in 1-butyl-1-methylpyrrolidinium bis(trifluoromethylsulfonyl)imide [BMP][Tf_2N] was studied using CV, linear scan voltammetry (LSV) and rotating ring-disk electrode (RRDE). The diffusion coefficient of germanium was calculated based on the relation between peak current density and scan rate. Germanium films were deposited on platinum, copper and n-type germanium substrates. SEM, EDX, XRD, transmission electron microscopy (TEM), electron backscatter diffraction (EBSD) and Auger electron spectroscopy (AES) were used to characterize the deposited germanium.

Chapter 6 is a summary of the main results and an outlook on future work.

Chapter 2

Electrodeposition of Bi_2Te_3 from chloride-free ethylene glycol solutions

This chapter is adapted from:

M. Wu, H. P. Nguyen, R. J. M. Vullers, P. M. Vereecken, K. Binnemans and J. Fransaer, Electrodeposition of bismuth telluride thermoelectric films from chloride-free ethylene glycol solutions, *J. Electrochem. Soc.*, **160**, D1–D6 (2013).

(Scientific contribution: most of the experiments, data analysis and writing the first draft.)

Abstract

Electrodeposition of bismuth telluride thermoelectric films is studied and compared in chloride-free and chloride-containing ethylene glycol solutions by means of cyclic voltammograms (CV), electrochemical quartz crystal microbalance (EQCM) and rotating disk electrode (RDE) experiments. It is found that chloride ions strongly affect the tellurium reduction but have almost no effect on the electrodeposition of bismuth. The kinetics of tellurium reduction in chloride-free solutions is three orders of magnitude lower than in chloride-containing solutions, while only a factor of three for bismuth. From chloride-free electrolytes, regular alloy deposition behavior was observed for the bismuth-tellurium system. Equilibrium deposition was obtained under various conditions, mostly at more negative potentials and from tellurium-rich solutions ([Te(IV)]/[Bi(III)]>1). Stoichiometric Bi_2Te_3 films with a smooth morphology were obtained over a wide potential range. Both p- and n-type films were prepared with a highest Seebeck coefficient of 120 $\mu V\,K^{-1}$. The chloride-free ethylene glycol electrolytes are highly promising for large scale production of bismuth telluride thermoelectric films as films with well-controlled composition can be deposited at high rates.

2.1 Introduction

Electrodeposition of bismuth telluride has been mostly carried out from acidic solutions (1 M HNO_3) [102, 31, 38, 103, 36, 104]. Because bismuth and tellurium are only sparingly soluble in acidic solutions, even in very acidic media, the deposition rates are limited. We have resolved this problem by investigating bismuth telluride electrodeposition from ethylene glycol electrolytes [105]. These solutions could dissolve up to 1 M bismuth nitrate and tellurium chloride and bismuth telluride films could be obtained at current density of -5 A dm^{-2} ($\sim$100 µm h^{-1}). However, highly tellurium-rich films were often obtained from these solutions, especially from concentrated solutions. This actually compromises the advantage of the high solubility of $TeCl_4$ and $Bi(NO_3)_3$ in ethylene glycol solutions. Furthermore, agitation was found to have strong effect on the film composition as almost pure tellurium deposits were obtained if the substrate rotated faster than 200 rpm. This is not practically convenient because agitation is often required to improve mass transport during deposition and the uniformity of deposits.

As the thermoelectric performance of bismuth telluride alloys strongly depends on their composition [106], controlling the film composition during electrodeposition is vitally important. In this chapter, we report that stoichiometric Bi_2Te_3 films can be easily obtained from chloride-free solutions, which are prepared by substituting NO_3^- for Cl^- ions and the alloy composition can be simply controlled by adjusting the molar ratio of Te(IV) and Bi(III) in the electrolyte. The kinetics of bismuth and tellurium reductions were studied in different electrolytes for the effect of chloride ions.

2.2 Experimental

Ethylene glycol (Alfa Aesar, 99%), $AgNO_3$ (Acros Organics, 99.85%), $TeCl_4$ (Alfa Aesar, 99%), $Bi(NO_3)_3{\cdot}5H_2O$ (Alfa Aesar, >98%), $LiNO_3$ (Sigma Aldrich, 99%), and LiCl were used as received.

Chloride-free ethylene glycol solutions containing 1 M tellurium ions were prepared by mixing a 1 M $TeCl_4$ solution with a 4 M $AgNO_3$ solution at 1:1 volume ratio. A slight excess of $AgNO_3$ (< 0.01 M) was added to minimize the remaining chloride concentration. The AgCl precipitate was removed by filtering. In order to minimize the remaining silver concentration in the solution, electrolysis was applied at a constant potential -0.1 V vs. Ag at 50 °C using a platinum coil as a counter electrode. These concentrated tellurium solutions

were then used as the tellurium ion source to prepare other tellurium and bismuth-tellurium solutions used in this work.

All the experiments were carried out in a three-electrode setup. The reference electrode was a porous ceramic-bottomed glass tube filled with an ethylene glycol solution containing 2 mM ferrocene (Fc), 2 mM ferrocenium (Fc^+) and 1 M $LiNO_3$ in which a Pt wire ($\phi = 0.5$ mm) was immersed. In this paper, all the potentials are converted with respect to the standard hydrogen electrode (SHE). A Pt coil was used as counter electrode. The films were deposited on gold-coated silicon wafers (silicon covered with 500 nm SiO_2, 10 nm Ti and 100 nm Au). The electrodes were cleaned by degreasing in an alkaline cleaner (P3-RST Henkel) at 70 °C for 10 minutes, then rinsed with deionized water and immersed in a 10 wt.% HCl solution for 1 minute, followed by rinsing with deionized water and absolute ethanol, and finally dried in a stream of warm air. Most electrochemical experiments were carried out with an EG&G 273 potentiostat. Conductivity measurements were carried out with an Autolab PGSTAT 302N potentiostat. The electrochemical experiments were typically performed at 50 °C. The diffusion coefficient of tellurium ions in the chloride-free electrolyte was estimated from polarization curves obtained at different rotation speeds with a platinum rotating disk electrode (Autolab $\phi = 3$ mm).

The chemical dissolution rates of bismuth and tellurium films in the ethylene glycol electrolytes were determined by using an electrochemical quartz crystal microbalance (EQCM, Maxtek). Thin bismuth and tellurium films previously electrodeposited on Pt-coated 5 MHz quartz crystals were immersed in different electrolytes and the mass change Δm was determined via the Sauerberey equation:

$$\Delta f = -C_f \Delta m \tag{2.1}$$

where Δf is the frequency change and C_f is the sensitivity factor of the crystal, which is 4020 Hz g^{-1} cm^2 in ethylene glycol solutions according to the calibration process described in [105].

The morphology and elemental composition of the films were determined by scanning electron microscopy (SEM) and energy-dispersive X-ray spectroscopy (EDX) (Philips XL 30 FEG). Seebeck coefficients of the deposited films were characterized using the method and setup described in [49].

2.3 Results and discussion

2.3.1 Chloride-free electrolytes

After pre-electrolysis, the tellurium concentrated chloride-free solutions were checked for remaining silver ions by inductively coupled plasma optical emission spectroscopy (ICP-OES, Varian 720-ES). A concentration as low as 29 ppm, which is approximate only 0.03 at% of the tellurium concentration, was often observed. In addition, no traces of silver were found in the energy-dispersive X-ray spectroscopy (EDX) spectrum of the deposited films. Therefore we can assume that the effect of the remaining silver concentration is negligible in the present system.

The solutions remained clear in closed bottles for months. After a long time, transparent crystals slowly appeared and became white precipitates when the solution was stirred. Analysis by single crystal X-ray diffraction showed that the crystals are neutral species with the chemical formula $Te(OCH_2CH_2O)_2$ and contain Te(IV) coordinated by two ethyleneglycolato (deprotonated ethylene glycol) molecules. The full structure determination is reported by Brooks *et al.* [107]. The precipitate could not be redissolved with heating and stirring. Even though the speciation of tellurium in the chloride-free solutions is not clear yet, we refer to tellurium present in the solutions as $Te(NO_3)_4$.

Measurements by a Mettler-Toledo DL39 Karl Fischer coulometer showed that the ethylene glycol electrolytes contained 5 wt% of water, which can be explained by the fact that the bismuth salt contains five water molecules ($Bi(NO_3)_3{\cdot}5H_2O$) and ethylene glycol is highly hygroscopic.

The corrosiveness of the chloride-containing ($TeCl_4$ + $Bi(NO_3)_3$) and chloride-free ($Te(NO_3)_4$ + $Bi(NO_3)_3$) electrolytes were evaluated by using electrochemical quartz crystal microbalance (EQCM) at 50 °C. The solutions contain 0.05 M of each metal salt and 0.5 M $LiNO_3$ as supporting electrolyte. The EQCM crystals with pre-deposited bismuth and tellurium films were immersed into the two solutions and mass loss Δm (g) was recorded in a period of time Δt (s). The corrosion rate was then estimated as follows:

$$\text{corrosion rate} = \frac{\Delta m}{1000 \rho A \Delta t}\,(\mathrm{m\,s^{-1}}) \tag{2.2}$$

where ρ is the density of the bismuth or tellurium film (kg m^{-3}), and A is the surface area of the working electrode (1.37 10^{-4} m^2). As shown in Table 2.1, higher corrosion rates for both bismuth and tellurium were observed in the solutions containing chloride ions, which is well explained by the simultaneous presence of nitrate and chloride ions.

Table 2.1: Corrosion rates (nm min^{-1}) of Bi and Te films in ethylene glycol solutions with and without chloride estimated by EQCM.

	chloride-containing	chloride-free
Bi	21.7	3.5
Te	18.2	0.5

2.3.2 Electrochemical behaviors of bismuth and tellurium ions in chloride-free solutions

The investigation by EQCM in our previous work has revealed that in chloride-containing ethylene glycol solutions bismuth and tellurium ions underwent one-step reductions to bismuth and tellurium [105]. In chloride-free solutions we assume that the same reduction mechanisms take place via the following reactions:

$$Bi^{3+} + 3e^- \rightarrow Bi \tag{2.3}$$

$$Te^{4+} + 4e^- \rightarrow Te \tag{2.4}$$

Cyclic voltammetry investigation shows that chloride ions have much stronger effect on tellurium than on bismuth reduction. The reduction peak of tellurium shifts to more negative potentials and becomes smaller when $Te(NO_3)_4$ is used instead of $TeCl_4$ as tellurium source as shown in 2.1. This agrees well with the previous observation that the reduction peak of tellurium shifted strongly to a more negative potential (-0.3 V) when a chloride salt was used as supporting electrolyte instead of a nitrate salt [105]. Because the influence of chloride ions on the bismuth reduction is insignificant, the shift of tellurium reduction peak brings the two reduction peaks close together, as shown in Figure 2.2 (dotted and solid lines). The simultaneous reduction of bismuth and tellurium is also observed in the solution containing both bismuth and tellurium ions as the cyclic voltammogram shows only one reduction peak (dash line in Figure 2.2). This suggests that the alloy composition will be unaltered over a wide range of applied potentials. This was verified by experiments (Section 2.3.3).

To investigate the effect of anions on the kinetic parameters of the bismuth and tellurium reductions in ethylene glycol solutions, rotating disk electrode experiments were carried out. The solutions containing 0.05 M of either $TeCl_4$ or $Te(NO_3)_4$ and 0.5 M $LiNO_3$ were used to study the electrochemical parameters of tellurium ions. The parameters of the bismuth ions in chloride-free solution was performed in a solution containing 0.05 M $Bi(NO_3)_3$ and 0.5 M $LiNO_3$. Extra 0.2 M LiCl, which provided the same chloride ion concentration as given by 0.05 M $TeCl_4$, was added into the previous bismuth solution to make a

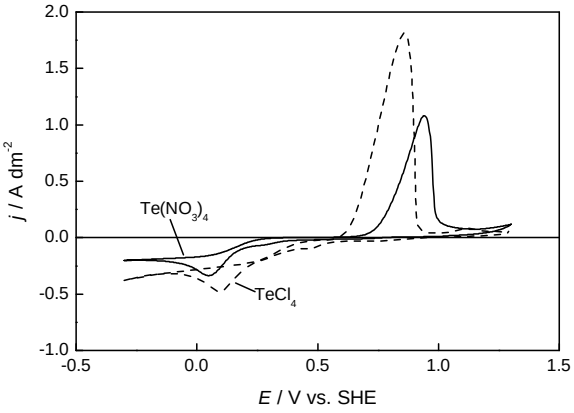

Figure 2.1: Cyclic voltammograms from ethylene glycol solutions containing 0.05 M $Te(NO_3)_4$ (solid line) or 0.05 M $TeCl_4$ (dash line) and 0.5 M $LiNO_3$ at 50 °C and at a scan rate of 20 mV s^{-1}.

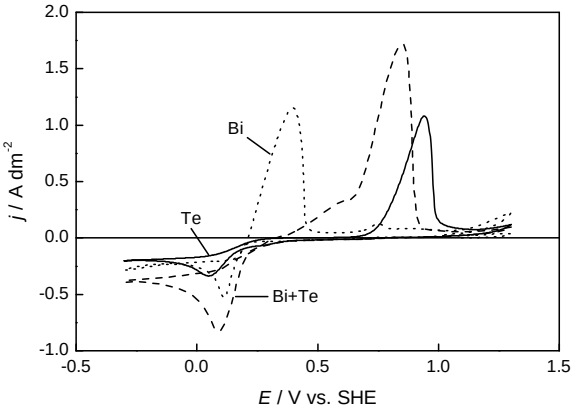

Figure 2.2: Cyclic voltammograms from ethylene glycol solutions containing 0.05 M $Bi(NO_3)_3$ (dotted line), 0.05 M $Te(NO_3)_4$ (solid line), and 0.05 M $Bi(NO_3)_3$ + 0.05 M $Te(NO_3)_4$ (dash line) (all with 0.5 M $LiNO_3$ supporting electrolyte) at 50 °C, and at a scan rate of 20 mV s^{-1}.

Table 2.2: Conductivity of different bismuth and tellurium ethylene glycol solutions at 50 °C. All solutions contain 0.5 M $LiNO_3$ as supporting electrolyte.

solution	conductivity / Ω^{-1} m^{-1}
0.05 M $Te(NO_3)_4$	0.40
0.05 M $TeCl_4$	0.51
0.05 M $Bi(NO_3)_3$	0.47
0.05 M $Bi(NO_3)_3$ + 0.2 M LiCl	0.62

chloride-containing solution. Bismuth or tellurium was deposited on a Pt electrode prior to each experiment. Polarization (j-E) curves were recorded at different rotation rates from 100 to 1000 rpm with a scan rate of 5 mV s^{-1} at 50 °C. To correctly estimate the kinetic parameters from the curves, iR-drop correction was applied for each curve with the conductivity of the solutions estimated from impedance measurement (Table 2.2). At different rotation rates, the reciprocal of the current density j at an applied potential is proportional to the reciprocal of the square root of the rotating speed ω, following the Koutecký-Levich equation [108]:

$$\frac{1}{j} = \frac{1}{0.62 z \mathrm{F} D^{2/3} \nu^{-1/6} c} \frac{1}{\omega^{1/2}} + \frac{1}{z \mathrm{F} c k} \tag{2.5}$$

where z is the number of electron involved in the electrodeposition reaction, F is Faraday's constant, D is the diffusion coefficient (m^2 s^{-1}), ν is the kinematic viscosity (m^2 s^{-1}), c is the bulk concentration of electroactive species (mol m^{-3}), ω is the rotation rate (rad s^{-1}), and k is the rate constant of the electrochemical reaction (m s^{-1}). Equation 2.5 predicts that plots of j^{-1} versus $\omega^{-1/2}$ generates parallel straight lines having slopes proportional to $D^{-2/3}$ and intersects with the y-axis proportional to k^{-1}, based on which D and k can be estimated. Figure 2.3 shows an example for the case of the ethylene glycol solution containing 0.05 M $Te(NO_3)_4$ and 0.5 M $LiNO_3$. The polarization curves are in Figure 2.3a and the Koutecký-Levich plots are shown in Figure 2.3b. The estimated diffusion coefficients for bismuth and tellurium are listed in Table 2.3. It shows that in nitrate solutions (chloride-free), the diffusion coefficients are lower than those in chloride-containing solutions, with a factor of about 1.5 and 2 for bismuth and tellurium, respectively.

The rate constant k in Equation 2.5, which can be determined from the intersects of Koutecký-Levich plots with the y-axis, depends on the overpotentials η as [109]:

$$k = k_0 \exp\left(-\frac{\alpha \mathrm{F}}{\mathrm{R}T}\eta\right) \text{ or } \ln(k) = \ln(k_0) - \frac{\alpha \mathrm{F}}{\mathrm{R}T}\eta \tag{2.6}$$

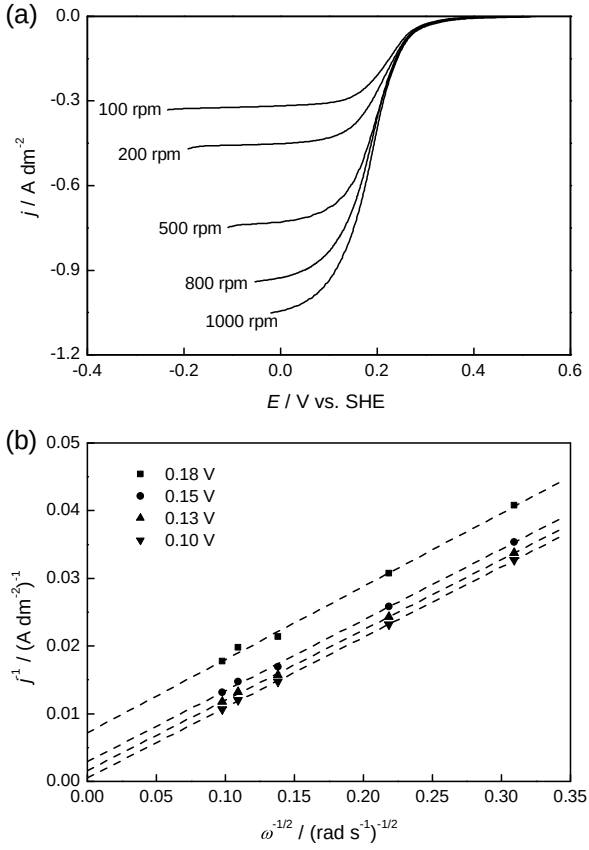

Figure 2.3: Polarization curves after iR correction (a) and Koutecký-Levich plots (b) for tellurium reduction at different potentials in an ethylene glycol solution containing 50 mM $Te(NO_3)_4$ and 0.5 M $LiNO_3$, at 50 °C, scan rate 5 mV s^{-1}.

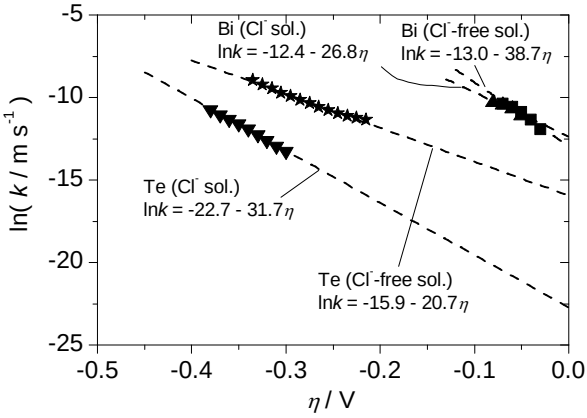

Figure 2.4: $\ln(k)$ vs. η plots for bismuth and tellurium reductions from different chloride-containing and chloride-free ethylene glycol solutions at 50 °C. The concentrations of bismuth and tellurium salts were 0.05 M, of LiCl was 0.2 M.

where k_0 is the standard rate constant (m s^{-1}), α is the transfer coefficient, R = 8.314 (J mol^{-1} K^{-1}) is the molar gas constant, T is the absolute temperature (K). Based on the linear dependence of $\ln(k)$ on the overpotential η, the cathodic transfer coefficient α can be obtained from the slope and the standard rate constant k_0 is estimated from the intercept with $\eta = 0$. The exchange current density is then derived [109]:

$$j_0 = z\mathrm{F}k_0c^{1-\alpha} \tag{2.7}$$

Figure 2.4 shows the $\ln(k)$ vs. η plots for bismuth and tellurium reductions from chloride-containing and chloride-free ethylene glycol solutions, from which the k_0, α, and j_0 were estimated and summarized in Table 2.3. The standard rate constants for bismuth reduction from chloride-containing and chloride-free solutions are 4.2 10^{-6} and 2.3 10^{-6} m s^{-1}, respectively, which are compatible to the reported value of 2 10^{-6} m s^{-1} for reduction of bismuth (III) chloride from molten $PbCl_2$ + KCl equimolar mixture at 475 °C [110]. The exchange current density for bismuth reduction from chloride-free solution is about 8.3 A m^{-2} while a higher value of 22.3 A m^{-2} is found in chloride-containing solution. The enhancement of bismuth reduction in presence of chloride ions was also observed by Johansson *et al.* in the exchange processes between bismuth chloride complexes and liquid bismuth amalgam, although with much larger effect from 4.55 A m^{-2} (38.4 mM Bi, chloride-free) to 230 A m^{-2} (4 mM Bi, 2 mM Cl^-) [111]. The effect of chloride ions on the kinetics of tellurium reduction is much larger. The standard rate constant increases three orders from 10^{-10} A m^{-2}

Table 2.3: Kinetic parameters for bismuth and tellurium in chloride-containing and chloride-free solutions. Diffusion coefficient D is estimated via slopes of Koutecký-Levich plots (Equation 2.5). Standard rate constant k_0 and exchange current density j_0 are estimated using Equation 2.6 and 2.7.

		D (m^2 s^{-1})	k_0 (m s^{-1})	α	j_0 (A m^{-2})
Bi	Cl^--containing	$1.2\ 10^{-10}$	$4.2\ 10^{-6}$	0.25	22.7
	Cl^--free	$8.5\ 10^{-11}$	$2.3\ 10^{-6}$	0.36	8.3
Te	Cl^--containing	$6.7\ 10^{-11}$	$1.2\ 10^{-7}$	0.14	1.3
	Cl^--free	$3.2\ 10^{-11}$	$1.4\ 10^{-10}$	0.22	$1.1\ 10^{-3}$

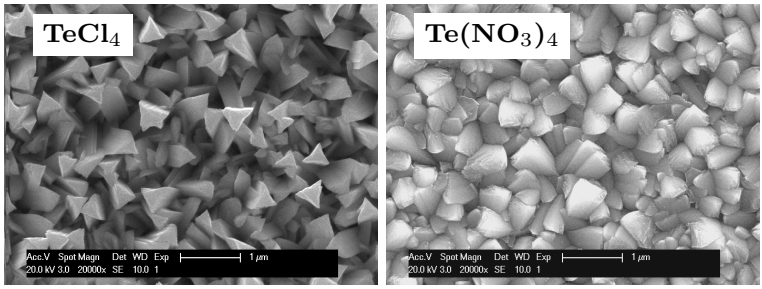

Figure 2.5: SEM images of Te films deposited from ethylene glycol solutions containing 50 mM $TeCl_4$ (left) or $Te(NO_3)_4$ (right) and 0.5 M $LiNO_3$ at 50 °C, -0.1 V vs. SHE, non-stirred.

in $Te(NO_3)_4$ solution to 10^{-7} A m^{-2} in $TeCl_4$ solution. These values are far higher than that of $2.3\ 10^{-12}$ m s^{-1} obtained in a chloride-free H_2SO_4 aqueous solution [112].

Chloride ions have a slight influence on the morphology of the films deposited at more positive potentials. However, at more negative potentials the tellurium films deposited from $TeCl_4$ solutions showed slightly rougher surface than those deposited from chloride free solutions as seen in Figure 2.5.

2.3.3 Bismuth telluride electrodeposition

Bismuth telluride films were electrodeposited at constant potentials from an ethylene glycol solution containing 40 mM $Bi(NO_3)_3$, 60 mM $Te(NO_3)_4$ and 0.5 M $LiNO_3$ at 50 °C. The same amount of charge was applied to obtain films with comparable thickness (∼0.5 µm). As can be seen in Figure 2.6, the

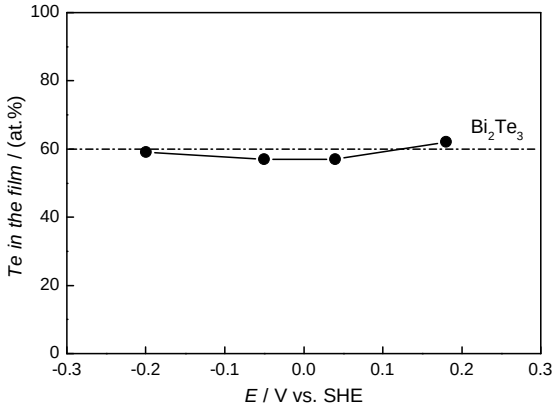

Figure 2.6: Composition of Bi_xTe_y films deposited at different potentials from a mixed solution containing 40 mM $Bi(NO_3)_3$, 60 mM $Te(NO_3)_4$, and 0.5 M $LiNO_3$, at 50 °C, non-stirred.

composition of the Bi_xTe_y is nearly independent of potential, when the potential was varied over a range of almost 0.5 V. This is already reflected by the cyclic voltammogram from the solution containing both bismuth and tellurium ions (dash line in Figure 2.2), where only one reduction peak was visible. Also, the molar ratio of the Bi to Te in the film was the same as that in the electrolyte, which suggests the deposition system is in the equilibrium mode. This is of great advantage for alloy deposition in general and for bismuth-tellurium alloy deposition in particular, because the thermoelectric performance of bismuth telluride materials strongly depends on their composition [106]. From this chloride-free ethylene glycol electrolyte, the composition of the films is much less dependent on the applied potential and can be easily controlled by adjusting the bath composition. This is very important for organic electrolytes, because often the poor electric conductivity of such solutions leads to large iR-drops, which alters the deposition potential especially on complex structures in uncontrollable ways.

Figure 2.7 shows the micromorphology of the films electrodeposited from an ethylene glycol solution containing 40 mM $Bi(NO_3)_3$ and 60 mM $Te(NO_3)_4$ and 0.5 M $LiNO_3$ at +0.05 V and -0.2 V (vs. SHE) at 50 °C. Both films show similar morphology, which is typical for electrodeposited stoichiometric bismuth telluride films. Slightly rougher films were obtained at more negative potentials, but they are still smoother than the film electrodeposited from chloride-containing ethylene glycol solution [105].

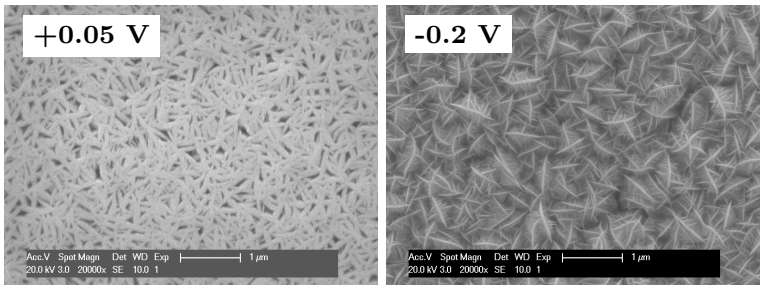

Figure 2.7: SEM images of Bi_xTe_y films deposited from a mixed solution containing 40 mM $Bi(NO_3)_3$, 60 mM $Te(NO_3)_4$, and 0.5 M $LiNO_3$, at 50 °C, non-stirred.

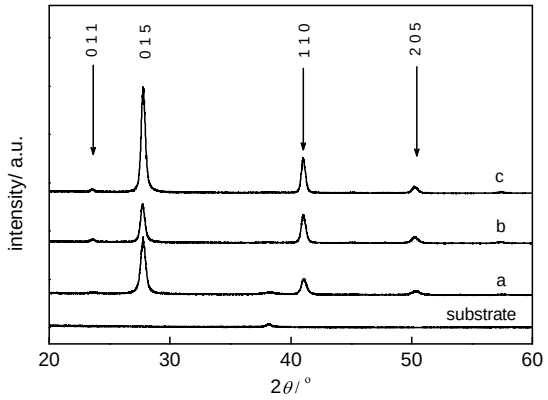

Figure 2.8: The XRD patterns of the films electrodeposited from the ethylene glycol solution containing 40 mM $Bi(NO_3)_3$, 60 mM $TeCl_4$ and 0.5 M $LiNO_3$ at different potentials: (a) -0.2 V, (b) -0.05 V, and (c) +0.07 V vs. SHE at 50 °C.

Figure 2.8 shows the XRD patterns of films electrodeposition from the solution containing 40 mM $Bi(NO_3)_3$, 60 mM $TeCl_4$ and 0.5 M $LiNO_3$ at 50 °C. In order to minimize the contribution from the substrate, a fixed incidence angle of 9° was applied. All the films have the rhombohedral crystal structure of Bi_2Te_3. The (0 1 5) plane peak is detected at $2\theta \sim 27.6°$ for all the films. In the film electrodeposited at -0.05 V, there are more crystals with a (1 1 0) orientation than in the films deposited at +0.07 V or -0.2 V (vs. SHE).

From chloride-free ethylene glycol solutions agitation shows nearly no effect on the film composition. As seen in Figure 2.9 consistent compositions between

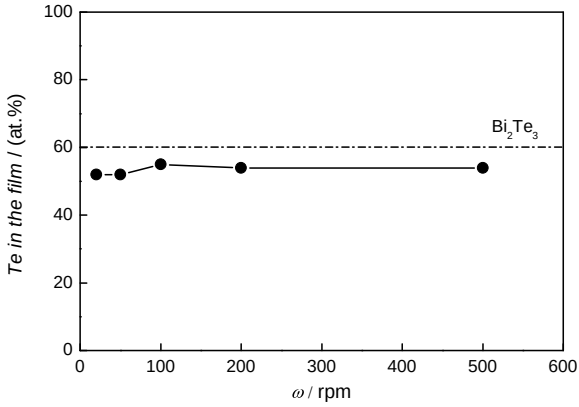

Figure 2.9: Composition of Bi_xTe_y films deposited at different rotation speeds from a chloride-free ethylene glycol solution containing 50 mM $TeCl_4$, 50 mM $Bi(NO_3)_3$, and 0.5 M $LiNO_3$, at 50 °C, at +0.18 V vs. SHE.

53-57 Te *at.*% were obtained for bismuth telluride films deposited at different rotation speeds between 0 and 500 rpm from a solution containing 50 mM $Te(NO_3)_4$ and 50 mM $Bi(NO_3)_3$ and 0.5 M $LiNO_3$, at +0.18 V vs. SHE, 50 °C. This is in strikingly contrast to the results observed for ethylene glycol electrolytes containing chloride ions, where almost pure tellurium films were obtained if the substrate rotated faster than 200 rpm. From a practical point of view, the chloride-free electrolyte is preferred because agitation is mostly required to improve mass transport and film uniformity. As seen in Figure 2.10, the morphology of the bismuth telluride films deposited at higher rotation rates is obviously improved.

Figure 2.11 shows the variation of composition of the films deposited at different potentials from solutions containing different metal ion ratios and different total concentrations ([Bi(III)]+[Te(IV)]). The content of tellurium, which is more noble than bismuth, increases monotonically with increasing tellurium concentration in solution for all cases. The tellurium content also increases as the total concentration increases from 0.1 M to 0.5 M (Figure 2.11). These observations are similar to those observed for the bismuth telluride deposition from chloride-containing ethylene glycol solutions [105], which are consistent with the behavior of a regular alloy deposition system [113]. However, in the chloride-free solutions, the variation of film composition is much less dependent on the total metal ion concentration, which is a great advantage for controlling alloy composition. As a result, bismuth telluride films with a composition close to the stoichiometric were obtained over a wide range of bath compositions.

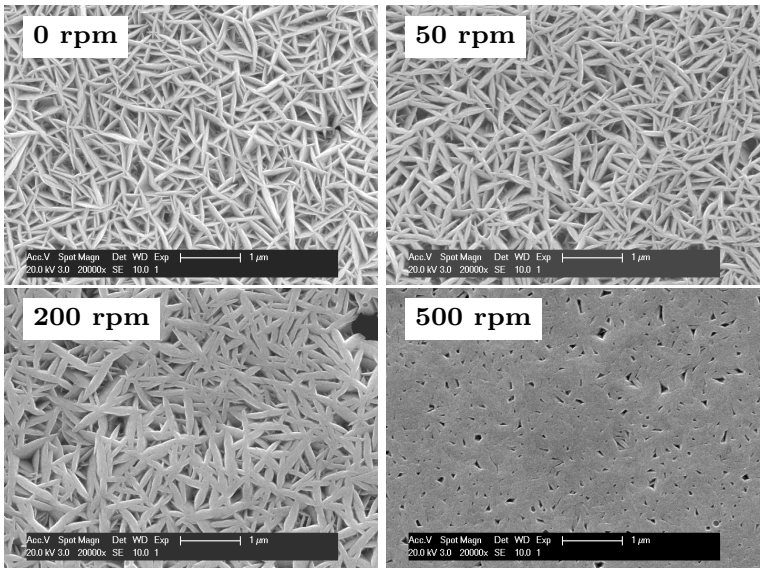

Figure 2.10: SEM images of Bi_xTe_y films deposited at different rotation speeds from a mixed solution containing 50 mM $TeCl_4$, 50 mM $Bi(NO_3)_3$, and 0.5 M $LiNO_3$, at 50 °C, +0.18 V vs. SHE.

It can also be recognized Figure 2.11 that many data points consist close to the reference line, which means the film composition is equal to the metal ion ratio in solution. These include the points for the films deposited at -0.05 V and -0.2 V vs. SHE from the solutions containing total metal ion concentration of 0.1 M (Figure 2.11a) and the films deposited at -0.2 V vs. SHE and metal ion ratios in solution of 0.6-0.8 from the more concentrated solutions (Figure 2.11b and c). This behavior is typical for equilibrium alloy deposition systems [113], from which the alloy composition can easily be varied by adjusting the metal ion ratio in solution.

Measurements of the Seebeck coefficient of the bismuth telluride films deposited at constant current densities (up to -3 A dm^{-2}, ∼10 µm) showed both positive and negative values, which means both p- and n-type semiconductor types have been prepared. The highest Seebeck coefficient of -120 µV K^{-1} was obtained for n- bismuth telluride films.

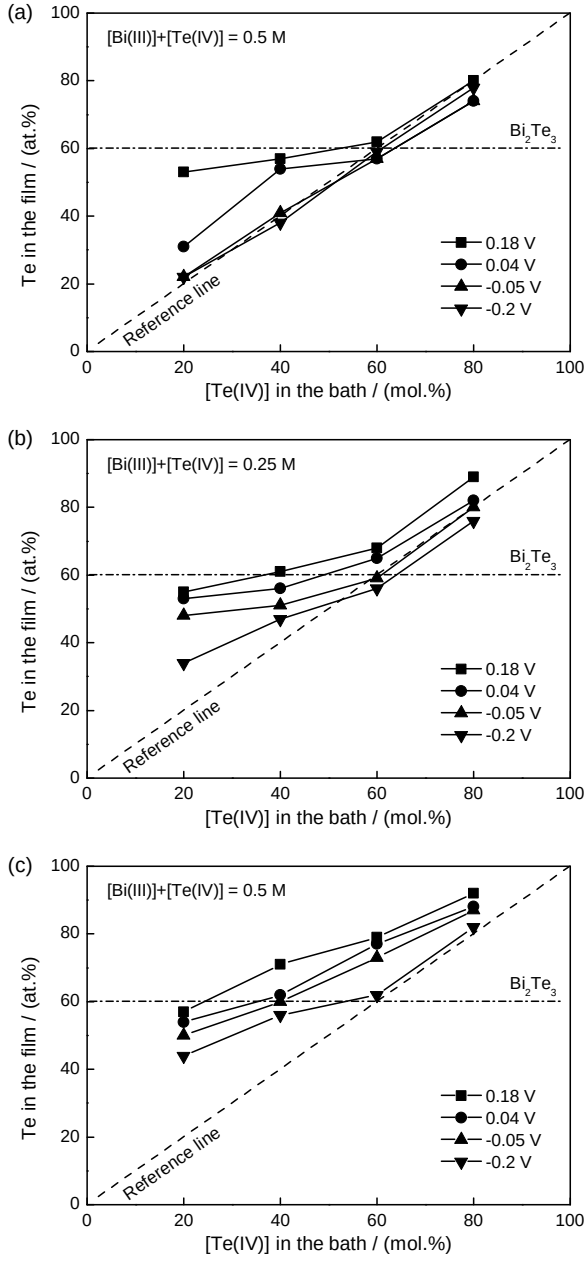

Figure 2.11: + $[Te(NO_3)_3]$).]Variation of Bi_xTe_y film composition with respect to bath content at different applied potentials from non-stirred ethylene glycol solutions containing different total concentrations ($[Bi(NO_3)_3]$+$[Te(NO_3)_3]$): (a) 0.1 M, (b) 0.25 M and (c) 0.5 M, at 50 °C.

2.4 Conclusions

Chloride-free ethylene glycol electrolytes were investigated for the electrodeposition of bismuth telluride thermoelectric films. Chloride ions were found to more strongly affect the reduction of tellurium than that of bismuth. The reduction peak of tellurium shifted to more negative potential in chloride-free ethylene glycol solutions and hence became close to the reduction peak of bismuth, which resulted in comparable deposition rates of bismuth and tellurium from the solutions. The standard rate constant of tellurium reduction in chloride-free solutions strongly decreased three orders of magnitude compared to that in chloride-containing solutions, while this factor was about three for bismuth reduction. These results explain the strong promotion of tellurium deposition in chloride-containing electrolytes, which results in the preferential deposition of tellurium from electrolytes containing both bismuth nitrate and tellurium chloride.

From chloride-free ethylene glycol electrolytes, bismuth telluride films with the desired stoichiometric composition (Bi_2Te_3) are obtained over a broad range of operational parameters. Both n-type and p-type bismuth telluride films were obtained. The highest Seebeck coefficient was -120 µV K^{-1}. The system show regular alloy deposition as the content of tellurium, the more noble metal, in film increases in proportion to its content in solution or with increasing total metal ion concentration in solution. Equilibrium deposition could be obtained under various conditions, mostly at relatively large overpotentials and from tellurium-rich solutions with Te-Bi ion ratios higher than 0.5. The alloy composition of the films is not affected by agitation. As bismuth telluride films can be deposited at high rates and their composition can be well controlled and ethylene glycol is a very cheap solvent, the chloride-free ethylene glycol electrolytes are highly promising for large scale electrodeposition of thermoelectric bismuth telluride films.

Chapter 3

Pulsed electrodeposition of thermoelectric $Bi_2Te_3/(Bi_{1-x}Sb_x)_2Te_3$ multilayers

This chapter is adapted from:

M. Wu, K. Binnemans and J. Fransaer, Electrodeposition of antimony from chloride-free ethylene glycol solutions and fabrication of thermoelectric $Bi_2Te_3/(Bi_{1-x}Sb_x)_2Te_3$ multilayer using pulsed potential electrodeposition, *Electrochim. Acta*, **147**, 451–459 (2014). – With permission from Elsevier.

(Scientific contribution: all of the experiments, data analysis and writing the first draft.)

Abstract

The electrochemical behavior of antimony in chloride-free ethylene glycol and the electrodeposition of antimony-bismuth and antimony-tellurium binary alloys, and bismuth-antimony-tellurium ternary alloys from ethylene glycol solutions were investigated by means of cyclic voltammetry (CV), electrochemical quartz crystal microbalance (EQCM) and rotating disk electrode (RDE) and rotating ring-disk electrode (RRDE) experiments. It was found that antimony(III), tellurium(IV) and bismuth(III) have comparable diffusion coefficients in ethylene glycol. The electrodeposition potential of antimony was more negative than that of tellurium and the alloy deposition obeyed regular alloy deposition behavior. In the ternary alloy deposition experiments, only a bismuth-telluride alloy could be electrodeposited at low overpotentials and the antimony content in the alloy increased when more negative potentials were applied or when lower rotation speeds were used. $Bi_2Te_3/(Bi_{1-x}Sb_x)_2Te_3$ multilayers were obtained by alternating the electrodeposition potentials using a rotating disk electrode. During the deposition of antimony by reduction of antimony(III) in ethylene glycol, “explosive” antimony was probably formed.

3.1 Introduction

Bismuth telluride and the derived antimony- and selenium-doped compounds have the highest ZT number ($\simeq$1) at room temperature of all known thermoelectric materials [1, 104, 114, 115, 116, 117, 118]. However, thermoelectric devices must have a $ZT > 3$ to become competitive with large-scale conventional cooling and power generation devices [119]. The thermoelectric performance can be significantly enhanced through nanostructuring [120, 121]. Multilayer (superlattice) thermoelectric materials are one of the nanostructuring materials that have larger ZT values than bulk materials [122]. Multilayer thermoelectric materials utilize the mismatch between two different layers leading to phonon scattering which reduces the thermal conductivity. Venkatasubramanian *et al.* reported a ZT value of about 2.4 for p-type Bi_2Te_3/Sb_2Te_3 superlattices at 300 K [18]. Thermoelectric materials can be obtained by electrochemical deposition which is an easy and fast technique [41, 47, 48, 123, 124]. Several research groups made efforts to electrodeposit bismuth-telluride-based mutilayer thermoelectric material. Ma *et al.* electrodeposited Bi_2Te_3/Sb_2Te_3 multilayer from two aqueous plating baths [125]. The electrodeposition of $Bi_2Te_3/(Bi_{1-x}Sb_x)_2Te_3$ multilayers from a single aqueous bath was studied by Banga *et al* [126]. Bi_2Te_2Se/Te and $Bi_2Te_3/(Bi_{0.3}Sb_{0.7})_2Te_3$ multilayer nanowire arrays were synthesized by pulsed potential deposition [127, 128].

Ethylene glycol was found to be an excellent solvent for electrodeposition of bismuth telluride [129, 105]. Equilibrium alloy deposition was obtained in ethylene glycol solutions with dissolved nitrate salts, and the film composition could be easily controlled by adjusting the molar ratio of bismuth(III) and tellurium(IV) in the solution. Due to the high solubility of both bismuth(III) and tellurium(IV) compounds in ethylene glycol, current densities up to -5.0 A dm^{-2} could be obtained. Antimony can be electrodeposited from various kinds of electrolytes [46, 130, 131, 132, 133, 134, 135, 136, 137]. In the aqueous solutions, Sb_2O_3 is a commonly used antimony source. It dissolves as antimonyl SbO^+ in very acidic media ($-2 < pH < 1$). In the pH range between 2 and 10, it forms undissociated $HSbO_2$ which is virtually insoluble. In more alkaline solutions, Sb_2O_3 dissolves upon formation of the antimonite ion SbO_2^- [40, 138]. To get hydrolyzed antimony ions for electrodeposition, very acidic or alkaline solutions were used in the literature for electrodeposition of antimony. Electrodeposited antimony is chemically attacked in very acidic media. Qiu *et al.* used an alkaline solution to dissolve Sb_2O_3 to deposit antimony [139]. However, the addition of a diaminourea polymer was required to obtain smooth and uniform films. $SbCl_3$ has a high solubility in ethylene glycol. Yamamoto *et al.* dissolved 8.1 mol.% $SbCl_3$ ($\sim$ 1.58 M) in ethylene glycol to study the electrodeposition of antimony from ethylene glycol [140].

In our experiments, ethylene glycol was used as the solvent. In order to have better control of film composition, smooth film morphology and to be sure that the solution is less corrosive, chloride-free solutions were prepared and used. In this paper, we describe the electrochemical behavior of the electrodeposition of antimony, antimony-bismuth and bismuth-tellurium alloys. Thermoelectric $Bi_2Te_3/(Bi_{1-x}Sb_x)_2Te_3$ multilayers were electrodeposited from a single bath using pulsed potential deposition.

3.2 Experimental

Ethylene glycol (Alfa Aesar, 99%), $SbCl_3$ (Alfa Aesar, >99%), $TeCl_4$ (Alfa Aesar, >99%), $Bi(NO_3)_3{\cdot}5H_2O$ (Alfa Aesar, >98%), $AgNO_3$ (Sigma-Aldrich, >99%), ferrocene (Acros Organics, 98%), ferrocenium hexafluorophosphate (Sigma-Aldrich, 97%) and $LiNO_3$ (Sigma-Aldrich, 99%) were used as received. $Sb(NO_3)_3$ solutions in ethylene glycol were prepared by mixing equal volumes of a solution of 0.4 M $SbCl_3$ in ethylene glycol and a solution of 1.2 M $AgNO_3$ (a slight excess) in ethylene glycol, followed by removal of the AgCl precipitate by centrifugation. The excess of silver(I) ions was removed by electrodeposition of silver on a large surface area platinum mesh working electrode, by applying a constant potential of -0.1 V (vs. Ag) and a platinum coil as the counter electrode. $Te(NO_3)_4$ solutions were prepared according to a literature procedure [129]. After pre-electrolysis, the 0.2 M $Sb(NO_3)_3$ and 0.5 M $Te(NO_3)_4$ ethylene glycol solutions were found to have a residual silver content of 4 ppm and 6 ppm, respectively (determined by ICP-AES on a Varian 720-ES apparatus).

All the experiments were carried out in a three-electrode set-up on a lab bench. Ethylene glycol is hydrophilic and it absorbs water from the environment, so all the solutions used contained 3–5% of water. The reference electrode was a glass tube with a porous ceramic plug in the bottom filled with an ethylene glycol solution with equimolar (2 mM) ferrocene (Fc) and ferrocenium hexafluorophosphate (Fc^+) and 1 M $LiNO_3$. The potential of the Fc/Fc^+ electrode was compared with the Ag/AgCl/3 M KCl electrode in a 3 M KCl solution at room temperature. The potential of Fc/Fc^+ electrode was +0.29 V vs. Ag/AgCl/3 M KCl electrode. In this paper, all the potentials were converted with respect to the standard hydrogen electrode (SHE). A platinum coil was used as counter electrode. The films were deposited on gold-coated silicon wafers (silicon covered with 500 nm of silica, 10 nm of titanium and 100 nm of gold). The wafers were cleaned by degreasing in an alkaline cleaner (P3-RST Henkel) at 70 °C for 10 min, then rinsed with deionized water and immersed in a 10 wt% HCl solution for 1 min, followed by rinsing with deionized water and absolute ethanol, and finally dried in a stream of warm air. The working

electrode for cyclic voltammetry and for linear scan voltammetry experiments was a polished platinum disk (diameter $\phi = 1$ mm) embedded in EpoFix® resin. The rotating disk electrode experiments were performed on a platinum rotating disk ($\phi = 3$ mm, Autolab).

The electrochemistry of antimony in ethylene glycol solutions was studied using an electrochemical quartz crystal microbalance (EQCM, Maxtek). The mass change per unit area (Δm) was determined from the Sauerbrey equation [141]:

$$\Delta f = -C_f \Delta m \tag{3.1}$$

where $\triangle f$ is the frequency change and C_f is the sensitivity factor of the crystal, which was calibrated as 4020 Hz g^{-1} m^2 in ethylene glycol solutions for a 5 MHz AT cut quartz crystal with a diameter of 2.54 cm. The working electrode was Pt/Ti with a surface area of 1.37 cm^2. The calibration process followed the method described by Gabrielli *et al* [142]. A solution of 50 mM $AgNO_3$ in ethylene glycol was used for calibration, and depositions were done at constant potentials. The sensitivity factor was calculated using the Sauerbrey equation by assuming the current efficiency for silver deposition in this solution is 100%.

All the electrochemical experiments were carried out with an EG&G 273 potentiostat/galvanostat or an Autolab PGSTAT 302N potentiostat. The elemental compositions of the deposited films were determined by inductively coupled plasma optical emission spectroscopy (ICP-OES, Varian 720-ES apparatus). The water contents of the solutions were measured using a Mettler-Toledo DL39 Karl Fischer coulometer. The films were characterized by scanning electron microscopy (SEM, Philips XL 30 FEG) using secondary electrons (SE) and back-scattered electrons (BSE). The antimony distribution in the multilayer was analyzed by wavelength dispersive–electron probe microanalyzer (WD-EPMA, field emission microprobe JXA-8530F). X-ray diffraction (XRD, Seifert 3003) was used to characterize the crystal structure of the deposits.

3.3 Results and discussion

3.3.1 Electrodeposition of antimony in ethylene glycol

The cyclic voltammograms of a solution of 50 mM $Sb(NO_3)_3$ and 0.5 M $LiNO_3$ in ethylene glycol on a platinum working electrode are shown in Figure 3.1a. The CVs were stopped at different cathodic vertex potentials to study the reduction reactions at different potentials. There are two reduction waves on the cathodic scan. The first reduction wave r1 is at +0.12 V, and the main reduction peak r2 at -0.08 V is assigned to the bulk reduction of Sb(III) ions to

elemental antimony. The reduction potential of antimony in ethylene glycol is more negative than that in the acidic solutions ($E^0_{SbO^+/Sb}$ = +0.21 V vs. SHE), but more positive than its reduction potential in alkaline solutions ($E^0_{SbO_2^-/Sb}$ = -0.66 V vs. SHE) [143]. On the reverse scan, a distinct stripping peak a1 was observed at a potential more positive to the onset of the bulk stripping peak a2. However, on the glassy carbon working electrode, only one reduction peak and one oxidation peak could be observed which illustrates the effect of substrate property on the pre-wave (Figure 3.1b). A similar pre-wave was observed during the deposition of antimony from the dimethyl sulfoxide (DMSO) solution containing 20 mM $SbCl_3$ by Li and co-workers [144]. They claimed that the pre-peak was due to the reduction of Sb(III) to Sb(II) and Sb(II) was further reduced to elemental antimony at more negative potentials. However, the pre-wave r1 in ethylene glycol solutions could not be assigned to Sb(III) to Sb(II). This was proven by the wait-scan experiments: a constant potential of +0.1 V, where only the first reduction reaction would happen, was applied for 10 seconds, then the potential scanned from +0.1 V to +1.1 V after waiting at open circuit potential for different times. An oxidation peak was always observed at the potential scan, indicating the reduction product at the first reduction peak was insoluble and did not diffuse away during the waiting time. Rotating ring-disk electrode (RRDE) experiment also shows that there was no Sb(II) produced on the cathodic scan. A constant potential of +0.8 V (vs. SHE) was applied on the ring while a cyclic voltammetry was performed on the disk. No oxidation current was detected on the ring. This suggests that no Sb(II) or Sb(I) ions formed on the disk. Besides, to the best of our knowledge, there are no other literature reports on the existence of Sb(II) species in solution. So the pre-wave r1 is not due to the multi-step reduction of Sb(III). The nucleation loop on the cyclic voltammogram and the position of the pre-oxidation peak eliminates the possibility of the underpotential deposition of antimony [145, 146]. A reasonable explanation for this pre-wave is the formation of the "explosive" allotrope of antimony. "Explosive" antimony is an amorphous, metastable form of antimony. By providing excitation energy, for instance by rubbing or scratching the compound, it "explosively" transforms into the stable crystalline form [147, 148]. Preparation of "explosive" antimony by electrodeposition was first described by Gore in 1855 [149]. This kind of amorphous antimony can be easily obtained by continuous electrodeposition from aqueous solutions at room temperature or below room temperature [148, 150]. The crystallinity can be improved by elevating the temperature, increasing the deposition rate or using pulsed electrodeposition [151, 152, 153]. In ethylene glycol solutions, the peak current density of the pre-wave r1 is only -0.05 A dm^{-2} which is a favorable condition for forming amorphous antimony. The electrodeposited amorphous antimony is less stable than crystalline antimony, so that it is stripped before the crystalline form. The stripping peak a1 associated with the pre-wave r1 was

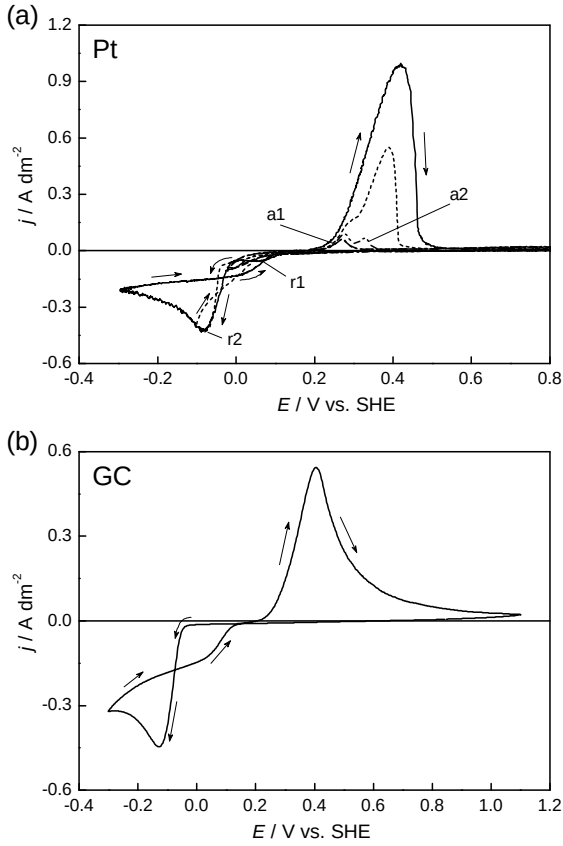

Figure 3.1: Cyclic voltammograms of an ethylene glycol solution containing 0.05 M $Sb(NO_3)_3$ and 0.5 M $LiNO_3$ at 50 °C on different working electrodes: (a) on a platinum disk electrode: the CVs were stopped at different cathodic vertex potentials, and (b) on a glassy carbon disk electrode. The counter electrode was a platinum coil. The scan rate was 20 mV s^{-1}.

observed before the oxidation peak a2 which corresponds to the dissolution of bulk antimony. The pre-wave can be assigned to the deposition of amorphous antimony.

Very uniform and flat antimony films could be electrodeposited at +0.1 V. At more negative potentials, the film became rough and dendrites could be observed (Figure 3.2). *Electrochemical quartz crystal microbalance* (EQCM) studies were carried out to compare the electrochemical behavior of antimony deposition in a solution of $Sb(NO_3)_3$ in ethylene glycol with the behavior of a solution of $SbCl_3$

in ethylene glycol. Cyclic voltammograms were recorded on a platinum-coated EQCM working electrode, and the corresponding frequency was simultaneously recorded using an EQCM. Figure 3.3 shows the EQCM results of the ethylene glycol solution of $Sb(NO_3)_3$ or $SbCl_3$. The blue curves are the real mass changes on the crystal which are calculated based on the frequency changes, and the red curves are the theoretical mass changes which are based on the charge passed through the working electrode. The mass increased during the cathodic scan due to the deposition of antimony, and then the mass decreased as the current changed to positive which is due to the stripping of the deposit from the crystal. In the ethylene glycol solution containing $Sb(NO_3)_3$ (Figure 3.3a), the theoretical mass did not fall back to zero after cyclic voltammetry. This is because the cathodic charge was greater than the anodic charge leading to a current efficiency lower than 100%. This is also evident in the EQCM data where it can be seen that the real mass increase during the cathodic scan is lower than the theoretical mass increase. In the potential range of the first reduction wave (Figure 3.3a inset), a mass increase could be observed, indicating antimony was deposited on the working electrode. This finding is consistent with the statement in the previous paragraph that Sb(III) is not reduced to Sb(II). In the $SbCl_3$-containing ethylene glycol solution (Figure 3.3b), on the forward scan, the real mass of the antimony deposit coincided with the theoretical mass change at potentials more positive than -0.4 V (vs. SHE). At the potentials more negative than -0.4 V, the experimentally observed mass became greater than the theoretical one. This can be explained by the morphology effect. At more negative overpotentials, the films became very rough and feather-like dendrites were formed leading to a mass increase (Figure 3.4). At the first reduction peak (Figure 3.3b inset), a real mass increase was also observed, which is due to the deposition of antimony. In both $Sb(NO_3)_3$ and $SbCl_3$ solutions, a pre-wave could be observed which corresponds to the deposition of amorphous antimony.

The diffusion coefficient of Sb(III) in the ethylene glycol solution containing 0.05 M $Sb(NO_3)_3$ and 0.5 M $LiNO_3$ was studied using linear scan voltammetry on a rotating disk electrode. The diffusion coefficient in the solution was calculated from the Levich equation:[108]

$$j_{\mathrm{L}} = 0.62 z \mathrm{F} D^{\frac{2}{3}} \omega^{\frac{1}{2}} \nu^{-\frac{1}{6}} c \tag{3.2}$$

where j_{L} is the limiting current density (A m^2), F is the Faraday constant (96485 C mol^{-1}), ν is the kinematic viscosity (m^2 s^{-1}), c is the concentration (mol m^{-3}), and ω is the rotation rate (rad s^{-1}). Based on the linear relationship between $\sqrt{\omega}$ and j_{L}, the diffusion coefficient can be calculated from the slope. A series of cathodic scans with different rotating speeds were carried out on a platinum rotating disk electrode, and all the scans started from open circuit potential. Figure 3.5a shows the polarization curves without IR-drop correction. The limiting current density at each rotation speed could be easily read from

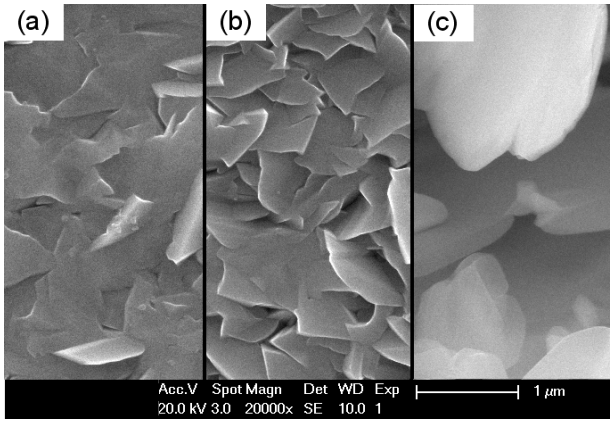

Figure 3.2: SEM images of the antimony films deposited from a 50 mM $Sb(NO_3)_3$ and 0.5 M $LiNO_3$ solution in ethylene glycol at 50 °C at different potentials: (a) +0.1 V, (b) -0.05 V, and (c) -0.15 V.

the plateau. The currents at -0.27 V were taken as the limiting currents. The diffusion coefficient of Sb(III) ions was derived from the plot of the limiting current density and the square root of the rotation speed (Figure 3.5b), and a value of 6.96±0.34 10^{-11} m^2 s^{-1} (95% confidence interval) was obtained. This value is smaller than that in aqueous solutions ($\sim 10^{-9}$ m^2 s^{-1}), but of the same order as the value in the choline chloride - urea deep eutectic solvent (1.76 10^{-11} m^2 s^{-1}) [43]. The difference in diffusion coefficient in different solutions is due to the variation in viscosity. As the Stoke-Einstein equation illustrates, the diffusion coefficient is inversely proportional to viscosity. The viscosity of ethylene glycol is higher than water leading to a lower diffusion coefficient in ethylene glycol. The value of the diffusion coefficient of Sb(III) ions is comparable to the values of the diffusion coefficients of Bi(III) and Te(IV) ions in the chloride-free ethylene glycol solutions, 8.5 10^{-11} m^2 s^{-1} and 3.2 10^{-11} m^2 s^{-1}, respectively [129].

3.3.2 Electrodeposition of Sb-Te and Bi-Sb alloys

The cyclic voltammogram of a solution of 50 mM $Sb(NO_3)_3$ and 50 mM $Bi(NO_3)_3$ in ethylene glycol contains two reduction peaks (Figure 3.6a). Because bismuth and antimony are perfectly miscible in the solid state, there is only one stripping peak. The first reduction peak at +0.14 V can be assigned to the reduction of Bi(III) to Bi(0). The second reduction peak at +0.015 V is due to the formation of a bismuth-antimony alloy. This peak lies at a potential +0.09 V

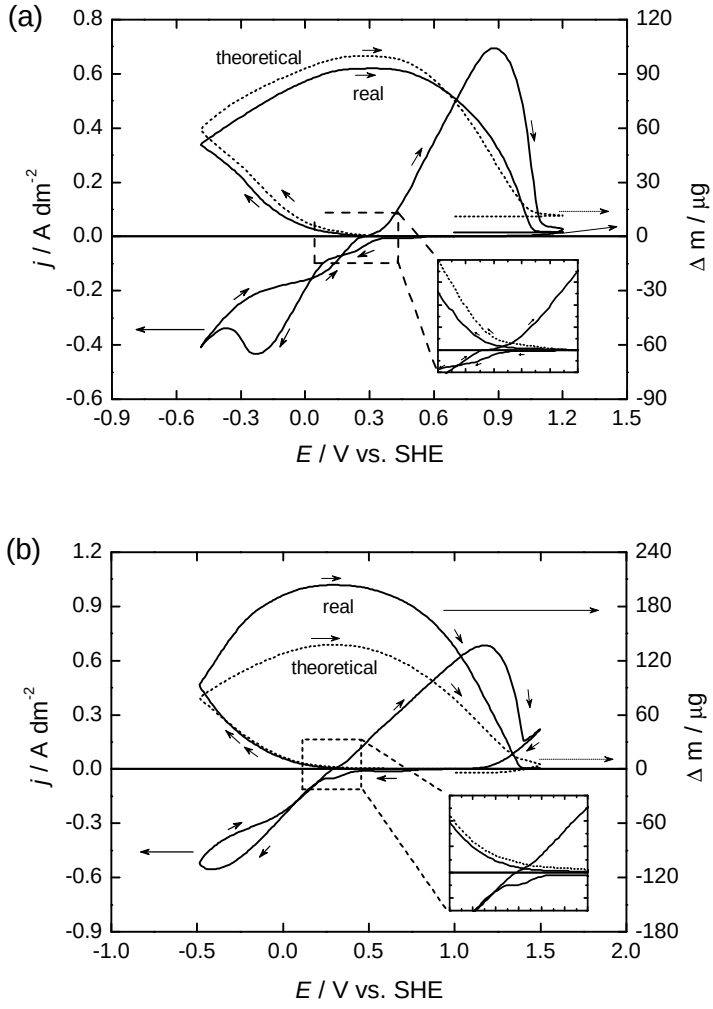

Figure 3.3: Cyclic voltammograms and corresponding real mass and theoretical mass changes on the crystal in ethylene glycol solutions containing (a) 50 mM $Sb(NO_3)_3$ and 0.5 M $LiNO_3$, and (b) 50 mM $SbCl_3$ and 0.5 M $LiNO_3$ at 50 °C. The working and counter electrodes were platinum, and the scan rate was 20 mV s^{-1}.

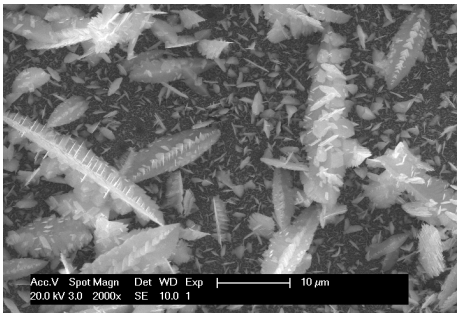

Figure 3.4: SEM image of the antimony film deposited from a 50 mM $SbCl_3$ and 0.5 M $LiNO_3$ solution in ethylene glycol at 50 °C at -0.15 V.

more positive than the potential of the reduction of pure antimony (Figure 3.1) which is caused by the activity of the alloy constituents [154, 155]:

$$E^0_{\mathrm{Sb}} + \frac{\mathrm{R}T}{3\mathrm{F}} \ln\left(\frac{a_{\mathrm{Sb}^{3+}}}{a_{\mathrm{Sb}}}\right) + \eta_{\mathrm{Sb}} = E^0_{\mathrm{Bi}} + \frac{\mathrm{R}T}{4\mathrm{F}} \ln\left(\frac{a_{\mathrm{Bi}^{3+}}}{a_{\mathrm{Bi}}}\right) + \eta_{\mathrm{Bi}} \tag{3.3}$$

$$a_{\mathrm{Sb}} = \exp\left(\frac{\mu_{\mathrm{Sb}}}{\mathrm{R}T}\right) \tag{3.4}$$

$$E_{\mathrm{Sb}} = E^0_{\mathrm{Sb}} + \frac{\mathrm{R}T}{3\mathrm{F}} \ln\left(a_{\mathrm{Sb}^{3+}}\right) - \frac{\mu_{\mathrm{Sb}}}{3\mathrm{F}} + \eta_{\mathrm{Sb}} \tag{3.5}$$

where E^0_i is the standard potential, a^{z+}_i is the activity of discharged ions, a_i is the activity of the metal at the surface of the alloy, η_i is the cathodic overpotential, and μ_i is the chemical potential or partial molar free energy of component i in the alloy. If the charge transfer kinetics for the deposition of component i is independent of the substrate composition, then η_i is constant. The deposition potential shift of antimony in alloy deposition can then be written as:

$$\Delta E_{\mathrm{Sb}} = -\frac{\mu_{\mathrm{Sb}}}{3\mathrm{F}} \tag{3.6}$$

$$\mu_{\mathrm{Sb}} = G^{\phi} + (1 - x_{\mathrm{Sb}}) \frac{\partial G^{\phi}}{\partial x_{\mathrm{Sb}}} \tag{3.7}$$

where G^{ϕ} is the Gibbs free energy of the alloy, which was calculated using the thermodynamic simulation software PANDAT^{TM}, where x_{Sb} is the molar fraction of antimony in the alloy. The deposition potential shift of antimony in bismuth-antimony alloy deposition was calculated according to the free energy of bismuth-antimony alloy, as shown in Figure 3.7. The Gibbs free energy is proportional to the alloy composition, and the deposition potential of antimony shifted +0.051 V to more positive potential. The potential shift calculated

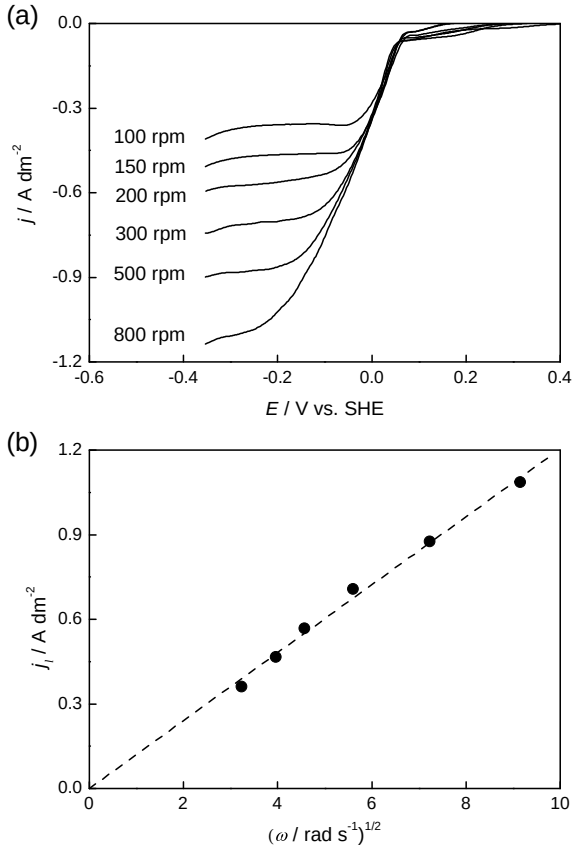

Figure 3.5: Polarization curves performed on an antimony-coated platinum rotating disk ($\phi = 3$ mm) in an ethylene glycol solution containing 50 mM $Sb(NO_3)_3$ and 0.5 M $LiNO_3$ at 50 °C (a), and Levich plot (b). The counter electrode was a platinum coil, and the scan rate was 5 mV s^{-1}.

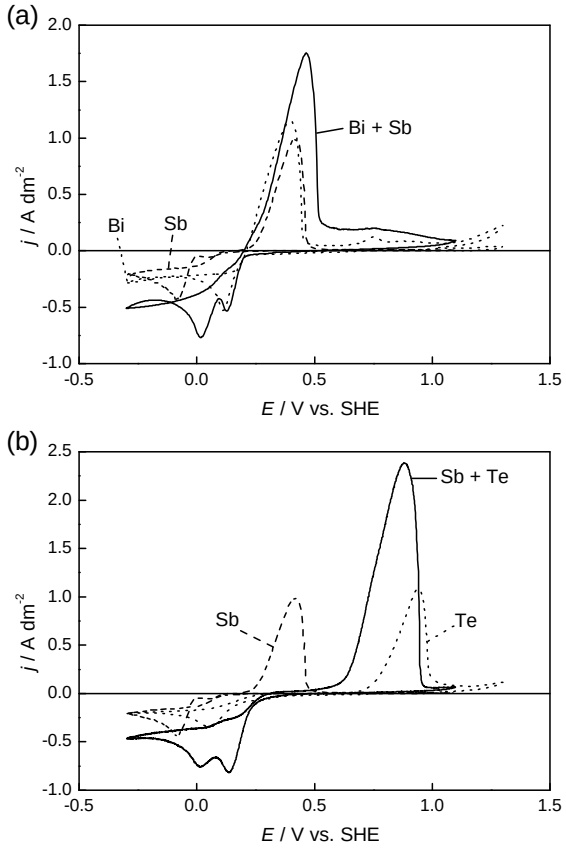

Figure 3.6: Cyclic voltammograms in ethylene glycol solutions at 50 °C: (a) 50 mM $Sb(NO_3)_3$, 50 mM $Bi(NO_3)_3$ and 0.5 M $LiNO_3$, (b) 50 mM $Sb(NO_3)_3$, 50 mM $Te(NO_3)_4$ and 0.5 M $LiNO_3$. The working and counter electrodes were platinum, and the scan rate was 20 mV s^{-1}.

from equation 3.6 and 3.7 corresponds well with the experimental shift of the potential observed in Figure 3.6a.

Bismuth-antimony alloys were electrodeposited from ethylene glycol solution containing 50 mM $Sb(NO_3)_3$ and 50 mM $Bi(NO_3)_3$ at different potentials. The SEM images of the films are shown in Figure 3.8. At large overpotentials, nucleation is favored over crystal growth and the crystals become smaller. The antimony content in the alloy increased as more negative potentials were applied.

Figure 3.6b shows the cyclic voltammogram of a solution of 50 mM $Sb(NO_3)_3$

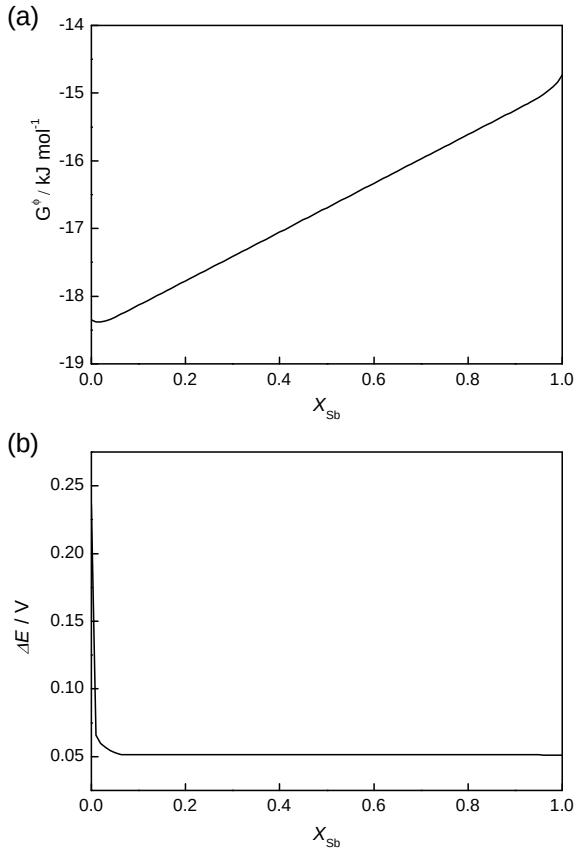

Figure 3.7: Gibbs free energy of bismuth-antimony alloys (a) and the calculated potential shift of antimony versus the mole fraction of antimony (b), calculated at 50 °C.

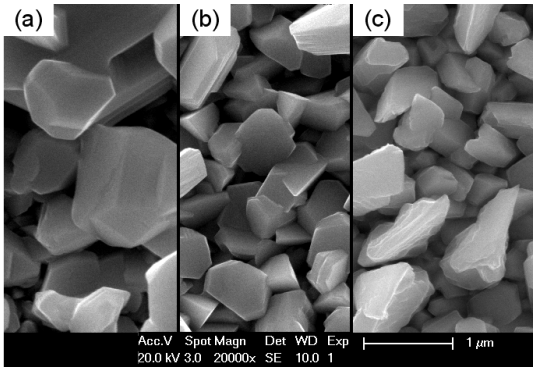

Figure 3.8: SEM images of the bismuth-antimony films deposited from a 50 mM $Sb(NO_3)_3$, 50 mM $Bi(NO_3)_3$ and 0.5 M $LiNO_3$ solution in ethylene glycol at 50 °C at different potentials: (a) +0.18 V (99 at.% Bi), (b) +0.08 V (86 at.% Bi), and (c) -0.04 V (64 at.% Bi).

and 50 mM $Te(NO_3)_4$ in ethylene glycol. There are two reduction peaks on the cathodic scan. The first peak at around +0.14 V is due to the reduction of Te(IV) to Te(0), and the second peak at +0.02 V is due to the formation of an antimony-tellurium alloy. This peak lies at a potential +0.1 V more positive than the potential of the reduction of pure antimony (Figure 3.1) due to the alloy formation lowering the chemical potential of antimony in the alloy. The antimony-tellurium alloy electrodeposition in ethylene glycol follows the regular deposition behavior. The electrodeposition of the more noble element, tellurium, in the ethylene glycol solution containing both $Te(NO_3)_4$ and $Sb(NO_3)_3$ is favored at lower overpotentials. The tellurium content in the film increases as its molar ratio increases in the bath (Figure 3.9). Very uniform and flat antimony-tellurium films were obtained from +0.18 V to -0.04 V, and the atomic concentration of tellurium in the film decreased at more negative potentials in an ethylene glycol solution containing 50 mM $Te(NO_3)_4$ and 50 mM $Sb(NO_3)_3$ (Figure 3.10).

3.3.3 Electrodeposition of multilayered thermoelectric material

To obtain thermoelectric material with a high ZT number, a high electric conductivity and a low thermal conductivity are desired. The most common way to increase ZT number is reducing the thermal conductivity by increasing phonon scattering more than the electron scattering. One way to achieve that

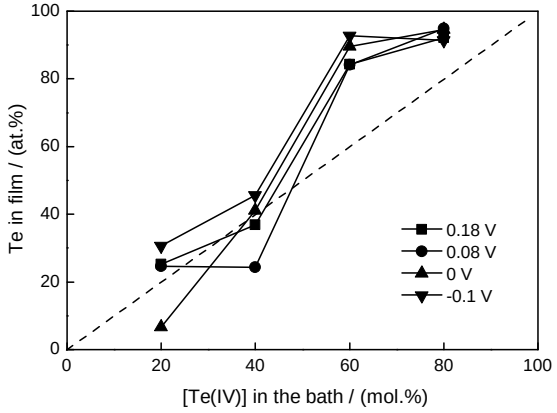

Figure 3.9: Dependence of the film composition on the electrolyte bath composition at 50 °C without stirring. The total metal ion concentration ([Te(IV)]+[Sb(III)]) was 0.2 M.

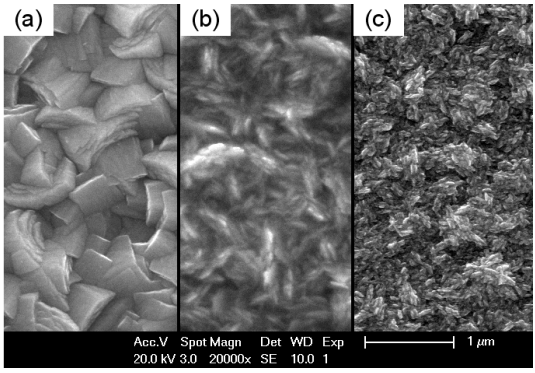

Figure 3.10: SEM images of the antimony telluride films deposited from a 50 mM $Sb(NO_3)_3$, 50 mM $Te(NO_3)_4$ and 0.5 M $LiNO_3$ solution in ethylene glycol at 50 °C at different potentials: (a) 0.18 V (95 at.% Te), (b) 0.08 V (74 at.% Te), and (c) -0.04 V (64 at.% Te).

is by making multilayer materials. The scattering of phonons at the interphase of the two layers lowers the thermal conductivity of the material. Multilayer materials are expected to have better thermoelectric performance compared to the single layer materials. $Bi_2Te_3/(Bi_{1-x}Sb_x)_2Te_3$ multilayer material could be electrodeposited from a single bath using pulse plating with the help of a rotating disk electrode. In the solution containing 20 mM $Bi(NO_3)_3$, 100 mM $Sb(NO_3)_3$ and 30 mM $Te(NO_3)_4$, films with different compositions were electrodeposited (Figure 3.12). The antimony content in the film increased and the tellurium content decreased as more negative potentials were applied. The increase in antimony content accompanied a decrease of tellurium content. This phenomenon was also observed for electrodeposition from aqueous solutions [126]. At more positive potentials or higher rotation speeds, 60 at.% Te could be obtained. At rotation speeds of 100 rpm and 200 rpm, the tellurium content increased from 40 at.% to 60 at.% for all potentials and the antimony fraction x in $Bi_{1-x}Sb_x$ decreased from 0.38 to 0.10. At a rotation rate of 500 rpm, the tellurium content was about 60 at.% at all the potentials, and the antimony fraction x varied from 0.24 to 0.10. The morphology of the films changed with the rotation speed and applied potentials. Figure 3.13 and 3.11 are SEM images of films electrodeposited at different rotation speeds and different potentials. With an increase in the rotation speeds, the crystals became larger. The crystals became smaller when more negative potentials were applied. The surface images of the films electrodeposited from the ethylene glycol solution exhibited a smooth morphology. The cross-section of the film (Figure 3.11e) shows a continuous film instead of crystal islands. The Seebeck coefficient of the electrodeposited $(Bi_{1-x}Sb_x)_2Te_3$ films were measured using the method described by Nguyen *et al.* [49]. $(Bi_{1-x}Sb_x)_2Te_3$ ($x < 0.4$) thin films are n-type thermoelectric materials.

The alloys containing 60 at.% Te were electrodeposited at different conditions. The X-ray diffraction (XRD) patterns of those $(Bi_{1-x}Sb_x)_2Te_3$ illustrate the existence of a single rhombohedral phase (Figure 3.14). The diffraction peaks shift to higher angles with the increase of antimony content. Similar peak shifts were also found for bulk $(Bi_{1-x}Sb_x)_2Te_3$ materials synthesized by mechanical alloying and pulse discharge sintering [16]. The peak at $2\theta \sim 27.8°$, 38.3°, 41.2° and 50.3° correspond to the crystal orientation of (0 1 5), (1 0 10), (1 1 0) and (2 0 5), respectively.

$(Bi_{0.91}Sb_{0.09})_2Te_3/(Bi_{0.8}Sb_{0.2})_2Te_3$ multilayer films were electrodeposited from the ethylene glycol solution containing 20 mM $Bi(NO_3)_3$, 100 mM $Sb(NO_3)_3$ and 30 mM $Te(NO_3)_4$ on a rotating disk electrode with a rotation speed of 500 rpm. Pulsed potential deposition was used to obtain layers with different compositions. $(Bi_{0.8}Sb_{0.2})_2Te_3$ layers were electrodeposited at -0.1 V and $(Bi_{0.91}Sb_{0.09})_2Te_3$ layers were electrodeposited at +0.25 V. The layer thickness

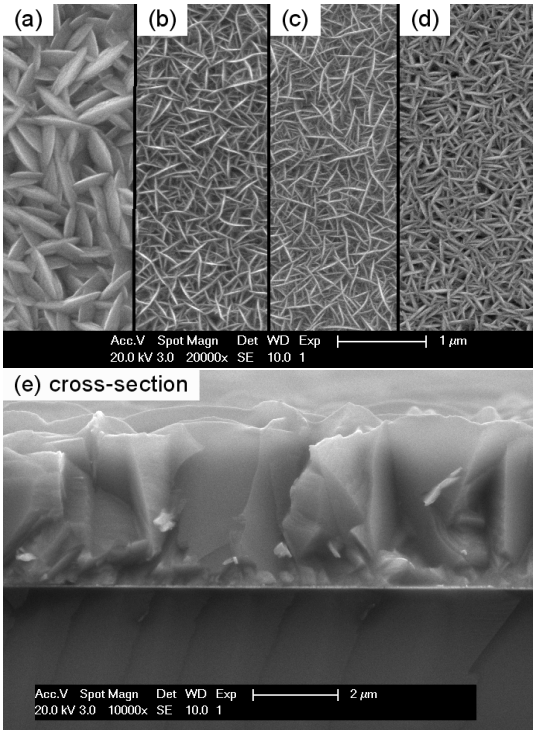

Figure 3.11: SEM pictures of films electrodeposited from an ethylene glycol solution containing 20 mM $Bi(NO_3)_3$, 100 mM $Sb(NO_3)_3$ and 30 mM $Te(NO_3)_4$ with a rotation speed of 200 rpm at different potentials: (a,e) +0.25 V, (b) +0.1 V, (c) 0.0 V, (d) and -0.1 V at 50 °C. (a-d) shows the surface morphology of the films and (e) shows the cross-section.

could be easily controlled using different pulsed time. The back scatter electrons image (BSE) of the cross-section in Figure 3.15a shows a clear contrast between each layer, indicating the different layer compositions. The antimony distribution is shown in Figure 3.15c. Each layer has a thickness around 1 µm. There is almost no antimony present in the layer electrodeposited at +0.25 V. The fraction of antimony in the alloy could be increased by reducing the rotation speed. $(Bi_{0.9}Sb_{0.1})_2Te_3/(Bi_{0.7}Sb_{0.3})_{2.8}Te_{2.2}$ multilayers were electrodeposited at a rotation speed of 200 rpm using a potential of -0.1 V for 80 s and +0.25 V for 500 s (Figure 3.15b). The layer thickness could be easily controlled by adjusting the deposition time. Efforts were made to measure both the in-plane and cross-plane thermal conductivity. However due to the influence of the substrates, the errors were so large that the results were not reliable.

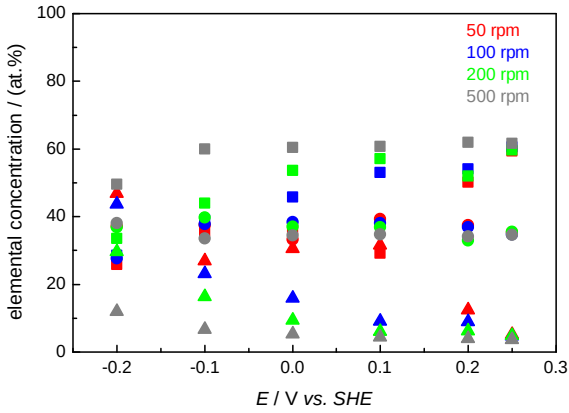

Figure 3.12: Composition of the films electrodeposited from an ethylene glycol solution containing 20 mM $Bi(NO_3)_3$, 100 mM $Sb(NO_3)_3$, 30 mM $Te(NO_3)_4$ and 0.5 M $LiNO_3$ at 50 °C on a rotating disk electrode with different rotating speeds: red: 50 rpm, blue: 100 rpm, green: 200 rpm and grey: 500 rpm. The symbols represent the concentration of different elements: ● Bi, ▲ Sb, and ■ Te.

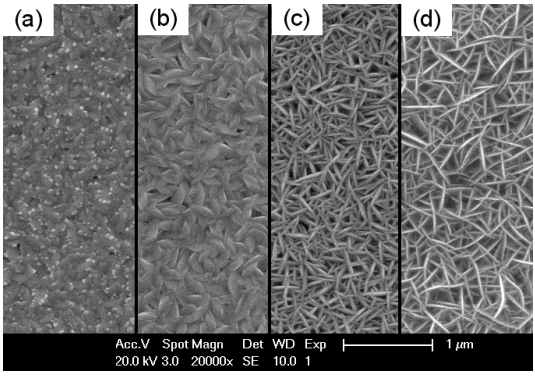

Figure 3.13: SEM pictures of the films electrodeposited from an ethylene glycol solution containing 20 mM $Bi(NO_3)_3$, 100 mM $Sb(NO_3)_3$ and 30 mM $Te(NO_3)_4$ at -0.1 V with different rotation speeds: (a) 50 rpm, (b) 100 rpm, (c) 200 rpm, and (d) 500 rpm at 50 °C.

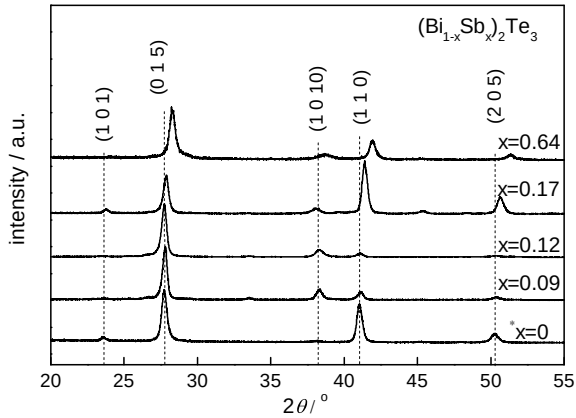

Figure 3.14: XRD patterns of the $(Bi_{1-x}Sb_x)_2Te_3$ films electrodeposited from an ethylene glycol solution containing 20 mM $Bi(NO_3)_3$, 100 mM $Sb(NO_3)_3$, 30 mM $Te(NO_3)_4$ and 0.5 M $LiNO_3$ at 50 °C. *The pattern is reported in ref. [129].

3.4 Conclusions

Chloride-free ethylene glycol solutions were used for electrodeposition of antimony and $Bi_2Te_3/(Bi_{1-x}Sb_x)_2Te_3$ multilayers. In the antimony solutions, Sb(III) was reduced to two different allotropes. Amorphous antimony might have been obtained at the first reduction wave in the cyclic voltammogram. At more negative potentials, Sb(III) was reduced to crystalline Sb(0). Both bismuth-antimony and antimony-tellurium show regular alloy deposition behavior from chloride-free ethylene glycol solutions. The antimony content in the alloys increased at more negative potentials. In the alloy deposition, the formation of the alloys lowered the partial molar energy of antimony leading to a positive shift of reduction potential of antimony. n-Type thermoelectric $Bi_2Te_3/(Bi_{1-x}Sb_x)_2Te_3$ ($x < 0.5$) multilayer could electrodeposited from a single electroplating bath by pulsed potentials using a rotating disk electrode. The layer thickness could be controlled by changing the deposition time. Lowering the rotation speed or electrodepositing at higher overpotential increased the antimony fraction in the $(Bi_{1-x}Sb_x)_2Te_3$ ternary alloys.

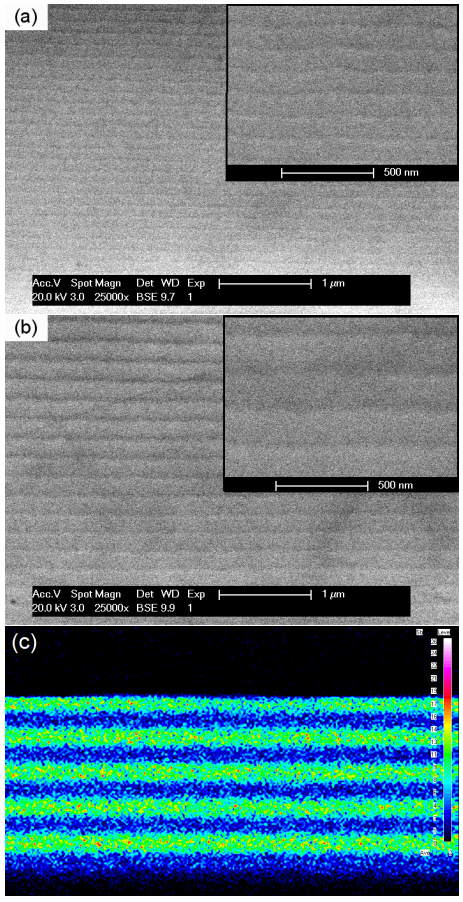

Figure 3.15: BSE images (a,b) and antimony distribution (c) of films electrodeposited from an ethylene glycol solution containing 20 mM $Bi(NO_3)_3$, 100 mM $Sb(NO_3)_3$, 30 mM $Te(NO_3)_4$ and 0.5 M $LiNO_3$ at 50 °C and for different rotation rates: (a) 500 rpm, the potential was switched from -0.1 V for 60 s to +0.25 V for 200 s (b) 200 rpm, the potential was switched from -0.1 V for 80 s to +0.25 V for 500 s.

Chapter 4

Electrodeposition of germanium from the ionic liquid 1-butyl-1-methylpyrrolidinium dicyanamide

This chapter is adapted from:

M. Wu, N. R. Brooks, S. Schaltin, K. Binnemans and J. Fransaer, Electrodeposition of germanium from the ionic liquid 1-butyl-1-methylpyrrolidinium dicyanamide, *Phys. Chem. Chem. Phys*, **15**, 4955–4964 (2013). – Reproduced by permission of the PCCP Owner Societies.

(Scientific contribution: most of the experiments, data analysis and writing the first draft.)

Abstract

The electrodeposition of germanium from the ionic liquid 1-butyl-1-methylpyrrolidinium dicyanamide ([BMP][DCA]) and a mixture of [BMP][DCA] with 1-butyl-1-methylpyrrolidinium chloride ([BMP]Cl) was studied using cyclic voltammetry and using an electrochemical quartz crystal microbalance (EQCM). $[GeCl_4(BuIm)_2]$ (BuIm = *N*-butylimidazole) was used as germanium source as it has a solubility of 0.47 M, up to 13 times the solubility of $GeCl_4$ in [BMP][DCA]. Cyclic voltammograms show an irreversible electrochemical behavior and two reduction waves were observed. The wave at the more positive potential was assigned to the reduction of Ge(IV) to Ge(II). The wave at the more negative potential was attributed to the formation of Ge(0). The diffusion coefficient of Ge(IV) in [BMP][DCA] containing 0.1 M $[GeCl_4(BuIm)_2]$ is 3.0 10^{-12} m^2 s^{-1}, and the exchange current density is 16 A m^{-2} at 50 °C. Polymerization of dicyanamide anions took place at the anode in the solution of [BMP][DCA]. The polymerization reaction could be suppressed by using an equimolar [BMP]Cl-[BMP][DCA] mixture as electrolyte. Smooth, porous germanium films were electrodeposited on both copper and silicon substrates.

4.1 Introduction

Germanium is a very important material for a wide range of applications, including electronic devices [156], light-emitting devices [157, 158], infrared sensors [159], and thermo-photovoltaic cells [160], Germanium thin films in commercial devices are mainly prepared by either chemical or physical vapor deposition, but the deposition rates are very slow. Typically, deposition rates for chemical vapor deposition are only about 1–5 monolayers per minute (equivalent to 9–43 nm per hour) [161]. The slow deposition rates and the deposition conditions (high vacuum is required) make these vapor deposition processes expensive.

Electrochemical deposition, which is a fast and cheap processing technique, can also be applied to obtain thin germanium films. However, the electrodeposition of germanium from aqueous solutions is very difficult because of the low hydrogen overpotential on germanium, and only ultrathin germanium films can be obtained [162]. Although bright germanium films can be electrodeposited from ethylene glycol and propylene glycol baths, the current efficiencies are low due to the hydrogen evolution [72, 163]. Current efficiencies can be increased by removing water from the electrolyte but this is very difficult to achieve in ethylene glycol and propylene glycol due to the strong hydrogen bonding [164]. Germanium films have been electrodeposited anodically from ethylenediamine solutions of K_4Ge_9, which contains deltahedral Ge_9^{4-} Zintl ions [165, 166]. The observed current efficiencies of the anodic deposition were at least two orders of magnitude higher than those of cathodic electrodeposition. Ke *et al.* investigated the electrodeposition of germanium from supercritical fluids, using the germanium(II) compound $[NBu^n_4][GeCl_3]$ and the germanium(IV) compounds $GeCl_4$ [92].

Ionic liquids offer an appealing alternative because they have a very wide electrochemical window and a relatively high ionic conductivity [74, 167, 168, 169]. Hydrophobic ionic liquids can also be more easily dried [170], and after drying, only a few ppm of water remain, which avoids the hydrogen evolution problem [78]. Endres and co-workers used 1-butyl-3-methylimidazolium hexafluorophosphate ([BMIM][PF_6]) and 1-butyl-1-methylpyrrolidinium bis(trifluoromethylsulfonyl)imide ([BMP][Tf_2N]) for germanium electrodeposition with $GeCl_4$, $GeBr_4$ or GeI_4 as a source of germanium [83, 88, 171, 80, 81, 82, 172, 87]. In their study, they noticed that the deposits were chemically attacked by GeI_4 [80], and that the bis(trifluoromethylsulfonyl)imide anions were found to decompose at the anode and the decomposition products caused the dissolution of the electrodeposited germanium films [88]. Also at temperatures above 370 K, the hexafluorophosphate anion can hydrolyse to give HF even when only small

traces of water are present [173], so we selected ionic liquids with non-fluorinated anions. Reports on nanostructured germanium, either in a wired or porous structure, have also been published [174, 175, 176, 90]. The electrodeposition of germanium and GeS_x has also been reported from the ionic liquid 1-methyl-1-propylpiperidinium bis(trifluoromethylsulfonyl)imide [177]. The deposited films of GeS_x were smooth, porous, and had an amorphous glassy character.

In this study, the ionic liquid 1-butyl-1-methylpyrrolidinium dicyanamide ([BMP][DCA]) was used as a solvent for germanium electrodeposition. Dicyanamide-based ionic liquids have low viscosities compared to other ionic liquids leading to a more efficient mass transport and a higher electrical conductivity. Due to the coordinating ability of the dicyanamide anion, metal salts are often better soluble in dicyanamide ionic liquids [178]. Although higher overpotentials are required to reduce a metal ion in a dicyanamide complex compared to the corresponding chloride complex [178], the 1-butyl-1-methylpyrrolidinium cation has a very good cathodic stability and can provide a potential range wide enough for the electrodeposition of germanium. A new germanium(IV) compound, $[GeCl_4(BuIm)_2]$ (BuIm = *N*-butylimidazole), was used as the germanium source. This compound has a higher solubility in [BMP][DCA] and lower vapor pressure than the commonly used germanium compound $GeCl_4$. In this paper we also describe for the first time the electropolymerization of dicyanamide at the anode during electrodeposition.

4.2 Experimental

Before use, 1-butyl-1-methylpyrrolidinium dicyanamide ([BMP][DCA])(IoLiTec, >98%) and 1-butyl-1-methylpyrrolidinium chloride ([BMP]Cl) (IoLiTec, >99%) were very thoroughly dried in a vacuum of 0.6 mbar at 120 °C for 8 hours. After drying, the water content of [BMP][DCA] was below 1 ppm. In some experiments, [BMP][DCA] was further degassed in high vacuum (6 10^{-7} mbar) for 60 hours at room temperature. $GeCl_4$ was provided by Umicore (Olen, Belgium, 99.99%). $[GeCl_4(BuIm)_2]$ was synthesized by dissolving $GeCl_4$ (2.30 g) in dichloromethane (10 mL) and *N*-butylimidazole (2.67 g) was added dropwise resulting in immediate precipitation of the product. The solid was recovered by filtration and washed with CH_2Cl_2 and then dried *in vacuo* to give $[GeCl_4(BuIm)_2]$ (4.78 g, 94 % yield) as a white solid. Raman: ν/cm^{-1}: 3176, 3149, 3001, 2961 2946, 2905, 2871, 2737, 1544, 1521, 1448, 1412, 1376, 1341, 1301, 1279, 1258, 1234, 1202, 1131, 1092, 1067, 1028, 978, 959, 887, 861, 720, 635, 400, 314, 290, 236, 197, 153, 118, 75. Found: Ge, 15.63 %. Calc. for $C_{14}H_{24}N_4GeCl_4$: Ge, 15.69 %. The germanium content was measured by total-reflection X-ray fluorescence (TXRF) on a Bruker S2 PicoFox spectrometer. The IR and Raman

spectra were recorded on a Bruker Vertex 70 FTIR spectrometer, coupled with a Ram II Raman module, at a resolution of 4 cm^{-1}. Manipulations were carried out using dry solvents in a glove box or using Schlenk line techniques. $SbCl_3$ (Alfa Aesar, >99%) and $AgNO_3$ (Sigma-aldrich, >99%) were used as received.

The viscosities of the liquids were measured by a Brookfield viscometer DV-II + Pro. The solubilities of $GeCl_4$ and $[GeCl_4(BuIm)_2]$ in [BMP][DCA] were determined by inductively coupled plasma atomic emission spectroscopy by a Varian 720 ES (ICP-OES) apparatus. The solutions for ICP were prepared by dissolving the $GeCl_4$ and $[GeCl_4(BuIm)_2]$ solutions in 23 wt.% HCl to prevent hydrolysis of germanium(IV) ions. The water content in the ionic liquid was measured using a Mettler Toledo DL39 Karl Fischer coulometer.

All electrochemical experiments were performed in an argon-filled glove box (oxygen and water contents were below 1 ppm). *n*-Type germanium was used as the reference electrode and also as the counter electrode in most experiments. A polished platinum disk ($\phi = 1$ mm), or an n-type germanium, or a p-type germanium was embedded in EpoFix® resin and used as working electrode. The germanium electrodes were connected with copper wire by soldering. These connections were tested by current-voltage experiment and they were ohmic contacts. Copper disks ($\phi = 2$ mm) or silicon (100) n-type (P-doped) wafers were used as working electrodes for germanium deposition. The rotating disk electrode experiments were performed on a platinum rotating disk ($\phi = 3$ mm, Autolab). Platinum and copper working electrodes were degreased with an alkaline cleaner (P3-RST Henkel) at 70 °C for 10 minutes, then rinsed with deionized water and immersed in 10 wt.% HCl solution for 1 minute, followed by rinsing with deionized water and absolute ethanol and finally dried in a stream of hot air. Silicon wafers were degreased by soaking them consecutively in dichloromethane, acetone, methanol and milli-Q water, each for 10 minutes. Then the wafers were cleaned in a mixture of H_2SO_4 and H_2O_2 (3:1) for 20 minutes. Afterwards, silicon wafers were hydrogen-terminated by immersing them in a 40 wt.% NH_4F solution which was purged by nitrogen gas for another 20 minutes. The light source for cyclic voltammometry under illumination was a halogen lamp (500 W). An EG&G 273 potentiostat or an Autolab PGSTAT 302N was used for electrochemical experiments.

The electrochemistry of the germanium solution and the polymerization in neat [BMP][DCA] were studied by electrochemical quartz crystal microbalance (EQCM, Maxtek RS232/IEEE488). The mass change per unit area ($\triangle m$) on a platinum-coated 5 MHz quartz crystal was determined by the Sauerbrey equation:

$$\Delta f = -C_f \Delta m \tag{4.1}$$

where Δf is the frequency change and C_f is the sensitivity factor of the crystal,

which was calibrated as 7126 Hz g^{-1} m^2 in [BMP][DCA] solutions. The calibration process followed the method described by Gabrielli *et al* [142]. A solution of 50 mM $AgNO_3$ in [BMP][DCA] was used for calibration, and depositions were done at constant potentials. The sensitivity factor was calculated using the Sauerbrey equation by assuming the current efficiency for silver deposition in this solution is 100 %.

An SDT (Simultaneous DSC and TGA) Q600 TA Instruments module was used for thermogravimetric analysis (TGA). The morphology and elemental composition of the films were determined by scanning electron microscopy (SEM) and energy-dispersive X-ray spectroscopy (EDX) (Philips XL 30 FEG).

4.3 Results and discussions

The ionic liquid 1-butyl-3-methyl-imidazolium dicyanamide ([BMIM][DCA]) was the first choice as the electrolyte solvent because of its low viscosity and because $[GeCl_4(BuIm)_2]$ also contains *N*-butylimidazole, but the electrochemical window of this ionic liquid was found to be only 3.0 V (-0.8 V to 2.2 V vs. Ge) on platinum. This value is in good agreement with the value of 3.0 V reported by Mann *et al* [179]. [BMP][DCA] which has the same anion as [BMIM][DCA] has an electrochemical window of 3.5 V on platinum and the cathodic limit is wide enough for germanium deposition (Figure 4.1 (solid line)). A small background current density is observed within the electrochemical window during the cathodic scan which is probably due to impurities in the ionic liquid. The volatile impurities were removed by degassing using the following procedure: the dried [BMP][DCA] was stored in high vacuum ($\sim$6 10^{-7} mbar) for more than 60 hours, while the liquid was continuously stirred by a magnetic stirrer bar. The formation of many bubbles was observed during the first 20 minutes of this procedure. These bubbles may be caused by remaining water traces and dissolved gases. The electrochemical window was measured after this degassing procedure in high vacuum, and it was found that the background current density on the cathodic scan could still be observed, but the current was smaller (Figure 4.1 (dotted line)). The remaining impurities causing the background current are probably not volatile and so cannot be removed in high vacuum.

$GeCl_4$ is the most widely used germanium source for germanium electrodeposition in ionic liquids [81, 83, 85, 88]. This compound is a liquid at room temperature and has a boiling temperature of 86.5 °C, so it easily evaporates at the elevated temperatures commonly used for carrying out electrodeposition experiments in ionic liquids. Also the solubility of $GeCl_4$ in [BMP][DCA] is low: only 38 mM of $GeCl_4$ can be dissolved in this ionic liquid at room

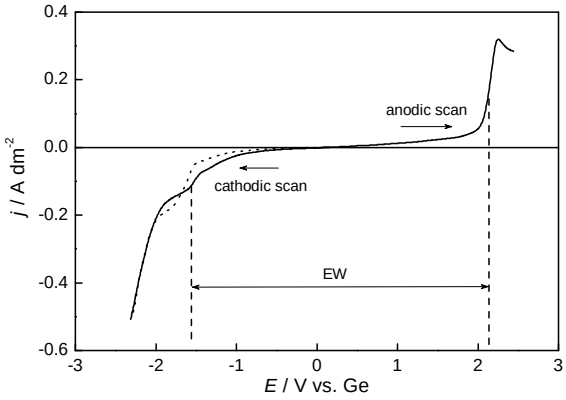

Figure 4.1: Voltammograms of [BMP][DCA] on a platinum disk ($\phi = 1$ mm), and the electrochemical window is indicated as EW. The solid lines are the linear sweep voltammograms in dried [BMP][DCA], and the dotted line is the cathodic scan in dried [BMP][DCA] kept in high vacuum (6 10^{-7} mbar) for more than 60 hours. The counter and reference electrodes were n-type germanium and the scan rate was 25 mV s^{-1}.

temperature, as determined by ICP-OES. In order to solve these problems, we decided to investigate other sources of germanium. We did this by reacting $GeCl_4$ with an organic ligand. Therefore $GeCl_4$ was reacted with two equivalents of *N*-butylimidazole (BuIm) to form the compound $[GeCl_4(BuIm)_2]$ which is a white solid with the structure shown in Figure 4.2. This compound is a lot less volatile than $GeCl_4$ as shown by thermogravimetric analysis (Figure 4.3) using a temperature program consisting of holding the temperature constant for 2 hours at 10 °C intervals between 30 °C and 100 °C (16 hours overall). The compound started losing weight at 50 °C, but there was only 15 % of weight lost in total. Additionally, the weight loss will be lower when the compound is dissolved in the ionic liquid because of the solvation interactions with the electrolyte. The low volatility of $[GeCl_4(BuIm)_2]$ makes it possible to work at higher temperatures than would be possible with $GeCl_4$. Moreover, $[GeCl_4(BuIm)_2]$ has a much higher solubility compared to $GeCl_4$: up to 0.47 M can be dissolved in [BMP][DCA] at room temperature. These properties make $[GeCl_4(BuIm)_2]$ a potentially better germanium source for electrodeposition from ionic liquids than $GeCl_4$.

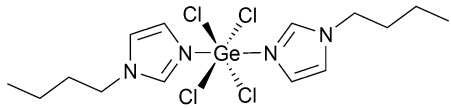

Figure 4.2: Structure of the germanium(IV) complex $[GeCl_4(BuIm)_2]$ used for the electrodeposition experiments in this work.

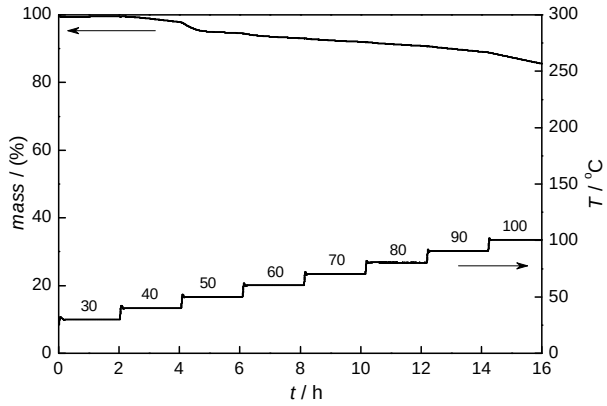

Figure 4.3: Thermogravimetric analysis for pure $[GeCl_4(BuIm)_2]$. The compound was kept at a given temperature for two hours and then heated to the next isothermal temperature in a nitrogen atmosphere.

4.3.1 Electrochemistry of $[GeCl_4(BuIm)_2]$ in [BMP][DCA]

Figure 4.4a shows the cyclic voltammograms of a 0.1 M $[GeCl_4(BuIm)_2]$ solution in [BMP][DCA] in the dark and under illumination. In theory, only a very small cathodic current on p-type germanium or a very small anodic current on n-type germanium can be observed in the dark. When the electrode was exposed to light, an increase of cathodic current on p-type germanium and an increase of anodic current on n-type germanium is expected. Under illumination, the cathodic current increased which suggests the deposited germanium is p-type. However, the anodic current also increased under illumination which is not expected as the anodic current on p-type semiconductor should not be affected by light. In order to compare the effect of light on n-type and p-type germanium electrode, cyclic voltammetry was also performed on both n-type and p-type germanium (Figure 4.4b). However, the cyclic voltammograms are very similar on both n-type and p-type germanium. This means the germanium electrode exhibits metallic behavior in the electrolyte. Hence, it is not possible to conclude

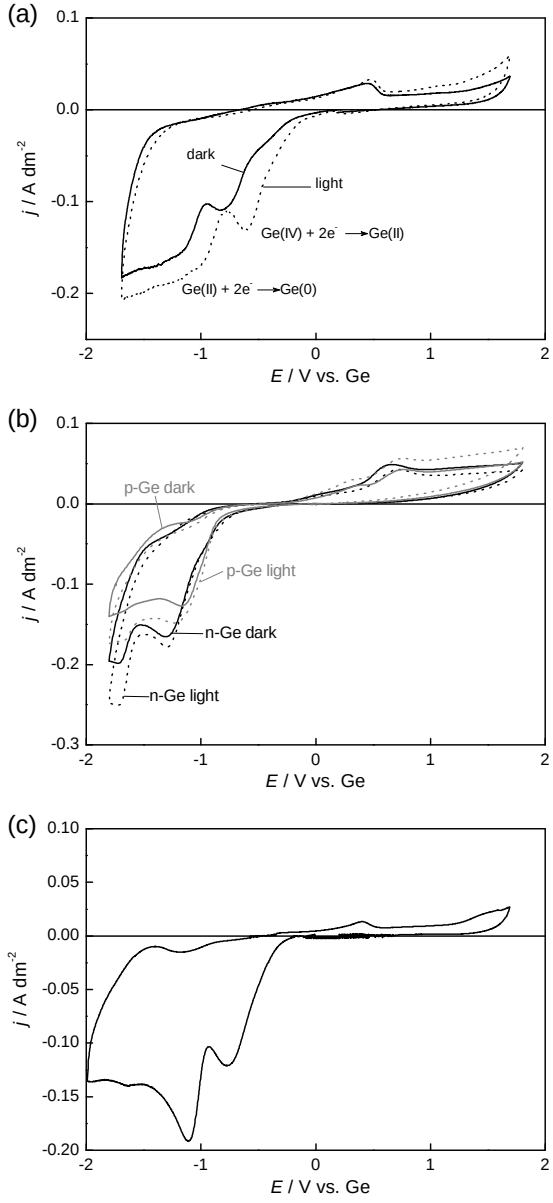

Figure 4.4: Cyclic voltammograms at room temperature: (a,b) in the 0.1 M $[GeCl_4(BuIm)_2]$ solution in [BMP][DCA]; (c) in the 0.4 M $[GeCl_4(BuIm)_2]$ solution in [BMP][DCA]. The working electrode were (a) a platinum disk coated with 30 nm germanium, (b) n-type germanium or p-type germanium and (c) a platinum disk. The counter and reference electrodes were n-type germanium and the scan rate was 25 mV s^{-1}.

if the deposited germanium is an n-type or a p-type semiconductor.

On the cyclic voltammogram (Figure 4.4a), there were two reduction waves on the cathodic scan. The first reduction wave at -0.6 V (vs. Ge) was assigned to the reaction Ge(IV) → Ge(II), and the second reduction wave to the Ge(II) → Ge(0). This was substantiated by electrochemical quartz crystal microbalance (EQCM) experiments. A cyclic voltammogram was recorded on a platinum-coated EQCM crystal working electrode, and the corresponding frequency change was simultaneously recorded using an EQCM. Based on the frequency change, the mass change on the crystal can be calculated from the Sauerbrey equation. By combing the information of the charge and mass change on the working face of the crystal, the M/z value at any potential is given by Faraday's law:

$$\frac{M}{z} = \mathrm{F}\frac{\Delta m}{j\Delta t} \tag{4.2}$$

where M (g mol^{-1}) is the molar mass of the reductant or the oxidant, z is the number of electrons involved in the electrochemical reaction, Δm (kg m^{-2}) is the mass change per surface area caused by Faradaic current, j (A m^{-2}) is the current density, and Δt (s) is the time. Every electrochemical reaction has a specific M/z value.

When a negative overpotential is applied, three possible reactions can occur. Ge(IV) ions can be reduced in a two-electron reaction to Ge(II):

$$\mathrm{Ge(IV)} + 2\mathrm{e}^- \rightarrow \mathrm{Ge(II)} \qquad (\frac{M}{z} = \frac{72.6}{2} = 36.3 \ \text{g mol}^{-1}). \tag{4.3}$$

However, as Ge(II) ions are soluble in this electrolyte, there is no mass change caused by this reaction on the crystal. The experimental M/z value of this reaction is zero. The Ge(II) can be further reduced in two-electron reaction to elemental germanium:

$$\mathrm{Ge(II)} + 2\mathrm{e}^- \rightarrow \mathrm{Ge(0)} \qquad (\frac{M}{z} = \frac{72.6}{2} = 36.3 \ \text{g mol}^{-1}), \tag{4.4}$$

or Ge(IV) ions can be directly reduced in a four-electron reaction to elemental germanium:

$$\mathrm{Ge(IV)} + 4\mathrm{e}^- \rightarrow \mathrm{Ge(0)} \qquad (\frac{M}{z} = \frac{72.6}{4} = 18.2 \ \text{g mol}^{-1}). \tag{4.5}$$

The latter two reactions will cause a mass increase on the crystal and they can be identified by their M/z values. If two reactions with different M/z values occur simultaneously, an intermediate M/z value will be found.

Figure 4.5a shows the frequency shift of the EQCM together with the cyclic voltammogram. From the open circuit potential to -0.75 V (vs. Ge), the

frequency change of the crystal is zero. The M/z values (Figure 4.5b) in this potential range are zero, indicating that Ge(IV) is reduced to Ge(II). At potentials below -0.75 V (vs. Ge), the frequency decreases fast and steadily. The decrease in frequency corresponds to the increase of the mass on the crystal. The M/z value increases from zero to around 18.2 g mol^{-1} suggesting that the reactions Ge(IV) to Ge(II) and Ge(II) to Ge(0) occur simultaneously. The deposition rate in this potential range is about 0.87 µm per hour. The electrodeposition efficiency increases with more negative potentials and 100 % efficiency can be obtained at potentials more negative than -1.1 V (vs. Ge). During the anodic potential scan, there is no frequency change in the beginning, then there is a small increase in frequency at +0.5 V (vs. Ge) which might be due to a slight dissolution of the deposited germanium. However most of the anodic current in this potential range is caused by the oxidation of Ge(II) to Ge(IV) which was proven by potential 'hold - scan' experiments. A constant potential of -0.4 V (vs. Ge), where only the reaction Ge(IV) to Ge(II) occurs, was applied for different times (from 0 s to 10 minutes), followed by scanning from -0.4 V to +1.0 V (vs. Ge). With longer holding times, more Ge(II) ions were generated and the oxidation peak was more pronounced. At more positive potentials, instead of an increase in the frequency of the EQCM, the frequency decreased very dramatically. The M/z value even reaches 520 g mol^{-1}, which indicates that something with a large molar mass is deposited on the electrode, which will be discussed later. As the charge used for the oxidation of Ge(0) and Ge(II) is very small compared to the charge for reduction of Ge(IV), the electrodeposition of germanium is virtually irreversible in this electrolyte.

The diffusion coefficient and kinetic parameters of Ge(IV) were also studied using rotating disk electrode voltammetry. The diffusion coefficient in the solution is calculated from the Koutecký-Levich equation [108]:

$$\frac{1}{j_{\mathrm{L}}} = \frac{1}{0.62 z \mathrm{F} D^{\frac{2}{3}} \omega^{\frac{1}{2}} \nu^{-\frac{1}{6}} c} + \frac{1}{z \mathrm{F} k c} \tag{4.6}$$

where j_{L} is the limiting current, F is the Faraday constant, ν is the kinematic viscosity (m^2 s^{-1}), c is the concentration (mol m^{-3}), ω is the rotation rate (rad s^{-1}), k is the heterogeneous rate constant for electron transfer (m s^{-1}). The kinematic viscosity was calculated from the dynamic viscosity, which is 3.3 10^{-5} m^2 s^{-1} at 50 °C (Table 4.1). Figure 4.6a shows the linear potential scans on a rotating disk electrode for various rotation rates. At more negative potential, the currents can be contributed by the reduction of both Ge(IV) and Ge(II), so it is not feasible to calculate the diffusion coefficient of Ge(IV) at more negative potentials using the Koutecký-Levich equation. As discussed above, at more positive potentials, only the reaction Ge(IV) → Ge(II) takes place and the current generated by this reaction can be used for calculating the diffusion coefficient of Ge(IV). Figure 4.6b is the Koutecký-Levich plot which

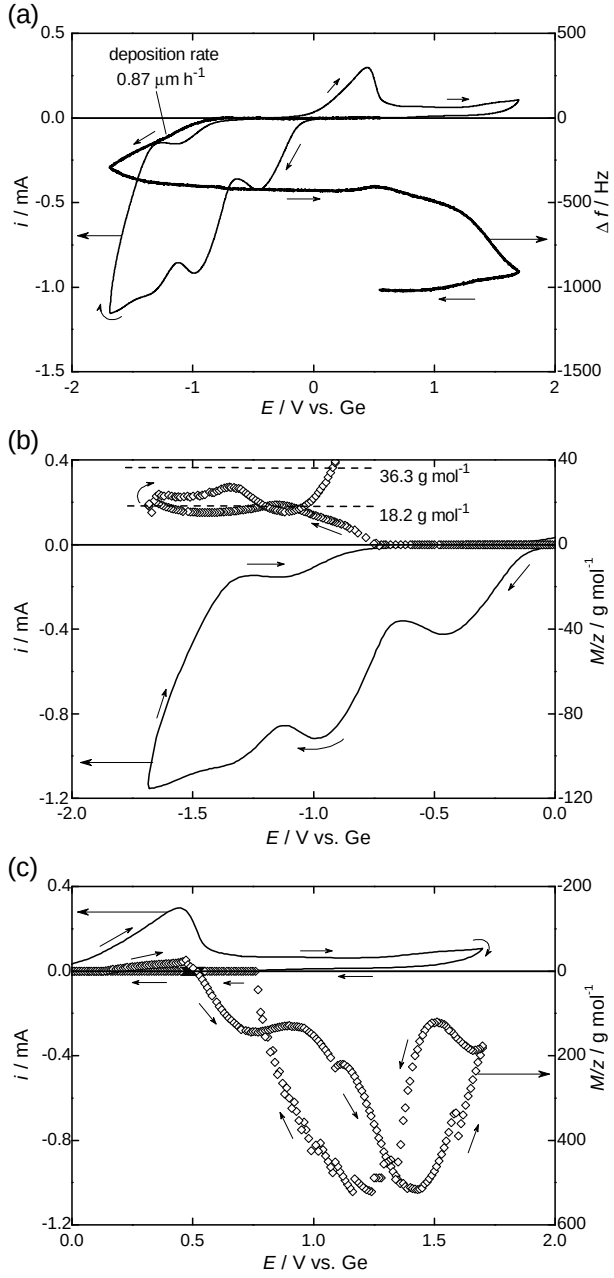

Figure 4.5: Cyclic voltammogram on a platinum coated quartz crystal (ϕ = 13 mm) and the crystal frequency change (a) and M/z values (b,c) for 0.1 M $[GeCl_4(BuIm)_2]$ solution in [BMP][DCA] at room temperature. The counter and reference electrodes were n-type germanium and the scan rate was 25 mV s^{-1}.

shows j^{-1} at potentials of -0.35, -0.40, 0.45 and -0.48 V (vs. Ge) as a function of $1/\sqrt{\omega}$. A diffusion coefficient of 3.0±0.2 10^{-12} m^2 s^{-1} was calculated from the slope. The rate constant k can be determined from the intercept of the plots and it depends on the applied overpotential as [109]:

$$\ln k = \ln k_0 - \frac{\alpha \mathrm{F}}{\mathrm{R}T}\eta, \tag{4.7}$$

where k_0 is the standard rate constant (m s^{-1}), α is the transfer coefficient which is a measure of the symmetry of the energy barrier [109], R is the molar gas constant, and η is the overpotential (V). The equilibrium potential for the reaction 4.3 is estimated as the zero-current potential, -0.41 V (vs. Ge) on the cyclic voltammogram (Figure 4.7). Based on the linear relationship between ln$k$ and overpotential η (Figure 4.8), the standard rate constant k_0 is determined as 2.99 10^{-6} m s^{-1}. The transfer coefficient α is 0.28 which suggests an asymmetric electron transfer behavior. The exchange current density can be calculated by:

$$j_0 = z\mathrm{F}k_0 c^{1-\alpha} \tag{4.8}$$

which gives 16 A m^{-2}.

4.3.2 Electrodeposition of germanium in [BMP][DCA]

As can be seen from the SEM image (Figure 4.9), uniform and porous germanium films could be electrodeposited from 0.1 M of $[GeCl_4(BuIm)_2]$solution in [BMP][DCA] at 50 °C. The EDX spectrum indicates a small amount of oxygen in the film probably due to the oxidation of the germanium surface upon exposure to the air. The porosity makes such germanium films useful as a potential anode for Li-ion batteries [180, 181]. The current density during the electrodeposition was very low, at constant potential of -0.6 V (vs. Ge), the average current density was only -4.3 10^{-3} A dm^{-2}, and it decreased with time (Figure 4.10a). This is because the electrodeposited germanium layer has a low electrical conductivity which causes a voltage drop at the cathode across the deposited germanium. As a result, at constant potential, with the increase in the coverage and thickness of the germanium film on the working electrode, the current decreases. The electrical conductivity of a semiconductor can be increased by doping. Figure 4.10b shows the change in the current density with time during the deposition of an Sb-doped germanium film. During the deposition of this film, Instead of decreasing, the current density increases during the first four hours after which it slowly decreased.

In order to increase the current density and hence the deposition rate, a more concentrated [BMP][DCA] solution containing 0.4 M $[GeCl_4(BuIm)_2]$ was

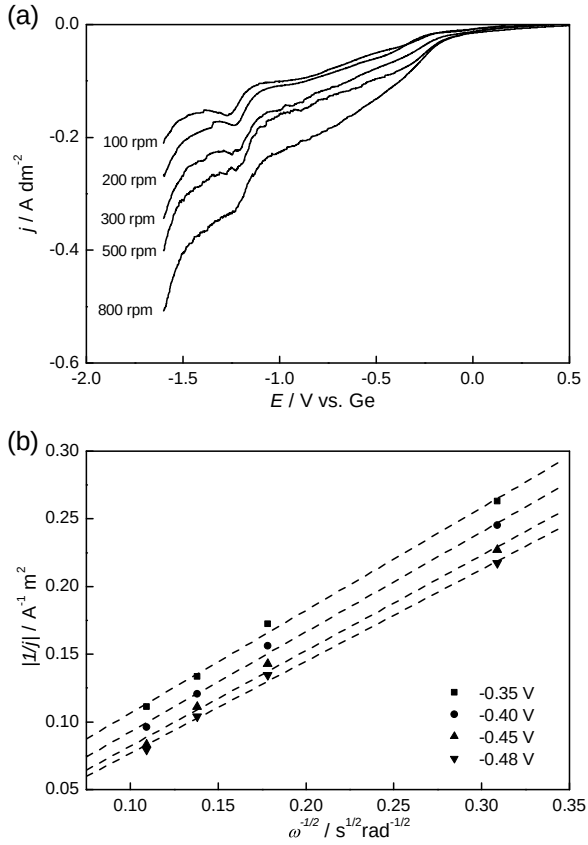

Figure 4.6: Polarization curves (a) performed on a platinum rotating disk (ϕ = 3 mm) in the 0.1 M solution of $[GeCl_4(BuIm)_2]$ in [BMP][DCA] at 50 °C, the counter and reference electrodes were n-type germanium and the scan rate was 25 mV s^{-1}; and Koutecký-Levich plot (b).

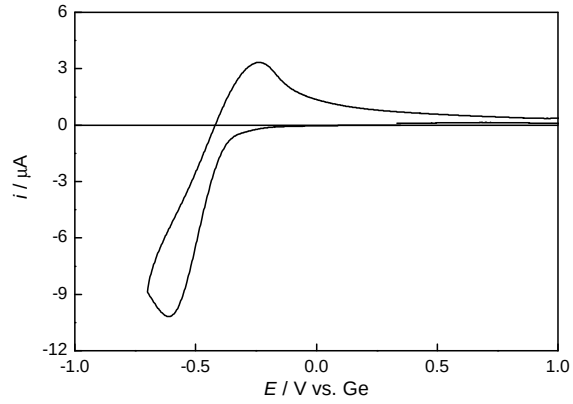

Figure 4.7: [
DCA] at 50 °C.]Cyclic voltammogram of 0.1 M [$GeCl_4(BuIm)_2$] solution in [BMP][DCA] at 50 °C. The counter and reference electrodes were n-type germanium and the scan rate was 25 mV s^{-1}.

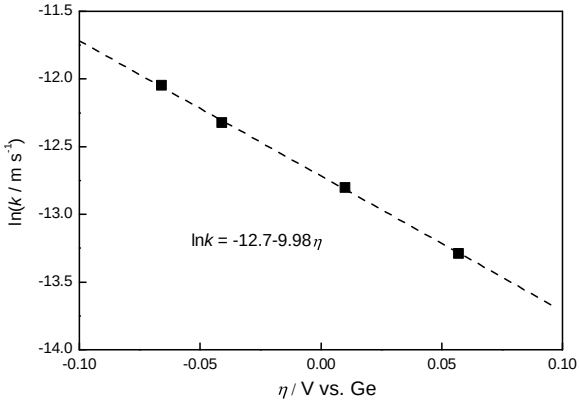

Figure 4.8: Plot of ln$k$ vs. overpotential η in the solution of 0.1 M [$GeCl_4(BuIm)_2$] in [BMP][DCA] at 50 °C. The working electrode was a platinum disk ($\phi = 3$ mm) and the counter and reference electrodes were n-type germanium.

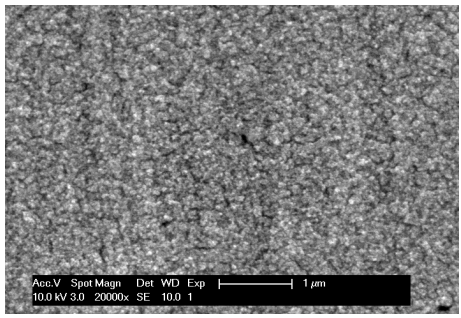

Figure 4.9: SEM images of the film deposited from a 0.1 M $[GeCl_4(BuIm)_2]$ solution in [BMP][DCA] at 50 °C for 13 h, applied potential: -0.65 V (vs. Ge), theoretical thickness: 0.8 µm. The working electrode was copper and the counter electrode was an n-type germanium wafer. The solution was stirred with a magnetic stirrer bar during deposition.

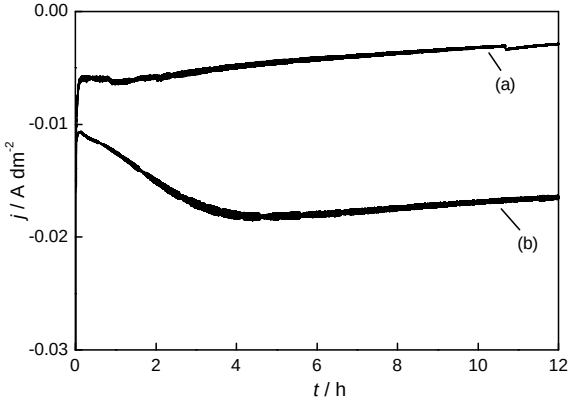

Figure 4.10: The current density changes with time during potentiostatic electrodeposition at -0.65 V (vs. Ge) in the 0.1 M $[GeCl_4(BuIm)_2]$ solution in [BMP][DCA] (a) and additional 1 10^{-6} M $SbCl_3$ (b) at 50 °C. The working electrodes were copper and the counter electrode was an n-type germanium wafer. The solutions were stirred with a magnetic stirrer bar during deposition.

prepared. The higher concentration of $[GeCl_4(BuIm)_2]$ made the solution very viscous (Table 4.1). Unfortunately, the dynamic viscosity of 0.4 M $[GeCl_4(BuIm)_2]$ in [BMP][DCA] is 15 times higher than that of 0.1 M $[GeCl_4(BuIm)_2]$, and 34 times higher than the viscosity of pure [BMP][DCA] at 30 °C. The cyclic voltammogram of this solution is shown in Figure 4.4c. The first reduction peak around -0.75 V (vs. Ge) is correlated to the reduction of Ge(IV) to Ge(II), and the second reduction peak at -1.1 V (vs. Ge) is due to Ge(II) to Ge(0). Compared to the 0.1 M $[GeCl_4(BuIm)_2]$ solution, the peaks are shifted by 0.2 V to more negative potentials. Although the concentration has increased four times, the current density of the reduction peaks in the 0.4 M solution has not increased compared to the current density observed in the 0.1 M solution. This can be explained by the increase in viscosity. The limiting current density can be estimated by the Levich equation:

$$j_{\mathrm{L}} = 0.62 z \mathrm{F} D^{\frac{2}{3}} \nu^{-\frac{1}{6}} \omega^{\frac{1}{2}} c, \tag{4.9}$$

and the Stokes - Einstein relation:

$$D = \frac{\mathrm{k_B} T}{6\pi\mu r} \tag{4.10}$$

where $\mathrm{k_B}$ is Boltzmann's constant, μ is the dynamic viscosity (Pa s), and r is hydrodynamic radius (m) of the diffusing species. At 30 °C, the dynamic viscosity of the 0.4 M solution is 15 times larger than that of the 0.1 M solution, and it can be assumed the kinematic viscosity is also affected by the same amount if the density change is negligible. Therefore the diffusion coefficient of Ge(IV) in the 0.1 M solution is 15 times higher than that in the 0.4 M solution based on the assumption that the sizes of the germanium complexes are the same in both solutions. The ratio of the limiting current densities in the 0.1 M solution and in the 0.4 M solution is calculated as 2.4 at 30 °C and this value decreases to 1 at 70 °C suggesting that the limiting current density cannot be increased by increasing the Ge(IV) concentration at temperatures below 70 °C. Germanium films were electrodeposited from a 0.4 M $[GeCl_4(BuIm)_2]$ solution at constant potential at two different temperatures. The films deposited at room temperature (Figure 4.11 a) are more porous than the ones electrodeposited at 50 °C (Figure 4.11 b). EDX analysis shows the films also contain a small amount of oxygen due to the oxidation of germanium in the air. During electrodeposition, the current density decreased with time which is similar to the case in the 0.1 M solution.

4.3.3 Polymerization of dicyanamide at the anode

It was observed that the color of the solutions changed after electrodeposition. The dried ionic liquid [BMP][DCA] has a pale yellow color (Figure 4.12a), which

Table 4.1: Viscosities of [BMP][DCA] and 0.1 M and 0.4 M solution of $[GeCl_4(BuIm)_2]$ in [BMP][DCA] at different temperatures

temperature (°C)	viscosity (Pa s)		
	[BMP][DCA]	0.1 M $GeCl_4(BuIm)_2$	0.4 M $GeCl_4(BuIm)_2$
30	0.031	0.070	1.05
50	0.016	0.033	0.30
70	0.010	0.019	0.097

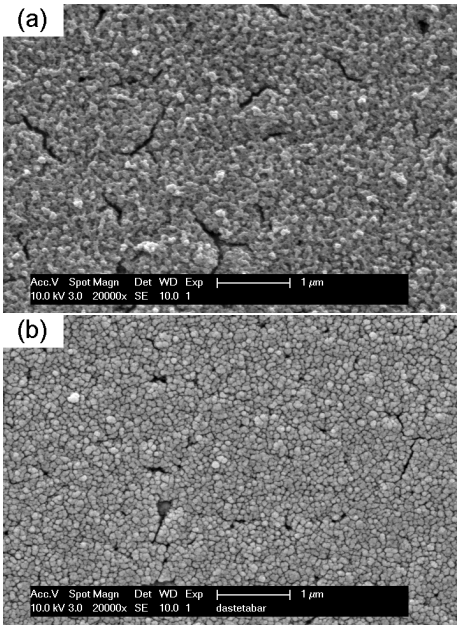

Figure 4.11: SEM images of the germanium film deposited from a 0.4 M solution of $[GeCl_4(BuIm)_2]$ in [BMP][DCA] at (a) room temperature and (b) 50 °C, deposition potential: -1.1 V (vs. Ge), theoretical thickness: 0.48 µm (a) and 0.53 µm (b). The counter electrode was an n-type germanium wafer and the solution was stirred with a magnetic stirrer bar during deposition.

became slightly more yellow by adding 0.1 M of $[GeCl_4(BuIm)_2]$ (Figure 4.12b). During electrodeposition, the color of the solution became darker as the amount of charge that passed through the electrolyte increased. The solution turned brown after passing about 271 C dm^{-3} of charge (Figure 4.12c). Changes could also be seen on the germanium counter electrode which originally had a silver-grey luster. After electrodeposition, it was still shiny but the color had changed to yellow (Figure 4.13). This layer was not soluble in acids or common organic solvents such as acetone, ethanol, methanol and dimethylformamide, but could be dissolved in alkaline solutions. The elemental composition of the layer was checked by EDX and it was found that it consisted of carbon, nitrogen and oxygen, showing that it is an organic layer.

The formation of this organic layer was further investigated by EQCM experiments. When a constant current density of 0.05 A dm^{-2} was applied in neat [BMP][DCA], the crystal frequency kept decreasing indicating that some compound was being deposited. The growth rate of the layer was calculated to be on average about 0.33 mg m^{-2} s^{-1} (Figure 4.14). This layer is probably caused by polymerization of an ionic liquid component. Considering the high electrochemical stability of the 1-butyl-1-methylpyrrolidinium cation [182], it is more likely that formation of the organic coating was caused by the electropolymerization of the dicyanamide anion.

This layer is not electrically conductive as can be seen from cyclic voltammograms of the simple ferrocene/ ferrocenium reaction (Figure 4.15). During the anodic scan, the ferrocene (Fc) is oxidized to ferrocenium (Fc^+), and then the Fc^+ is reduced back to Fc during the cathodic scan. The magnitude of the anodic and cathodic currents should be comparable. However the first cycle of the cyclic voltammogram shows a larger anodic current compared to the cathodic one. This is caused by the formation of an insulating organic layer on the working electrode during the anodic scan that blocks part of the active area of working electrode. The current density also decreases with the number of scan cycles due to the increase in the coverage area of the organic layer on the working electrode implying very poor electrical conductivity of the organic layer. Due to this poor conductivity of the organic layer formed at the anode during electrodeposition of germanium from 0.1 M of $[GeCl_4(BuIm)_2]$ solution in [BMP][DCA], the potential increased between working electrode and counter electrode.

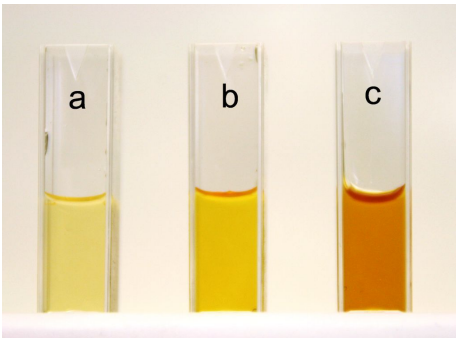

Figure 4.12: Color changes of the electrolyte solution: dried ionic liquid [BMP][DCA], freshly prepared 0.1 M $[GeCl_4(BuIm)_2]$ in [BMP][DCA], and (c) 0.1 M $[GeCl_4(BuIm)_2]$ in [BMP][DCA] after passing 271 C dm^{-3} of charge.

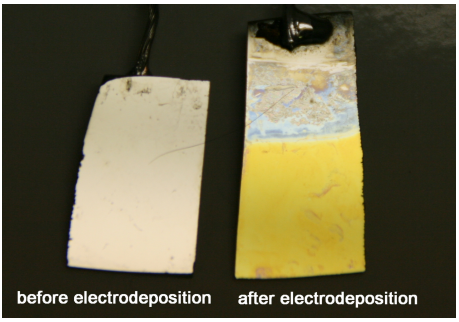

Figure 4.13: Picture of the n-type germanium wafer anode before (left) and after (right) electrodeposition in a 0.1 M $[GeCl_4(BuIm)_2]$ solution in [BMP][DCA].

4.3.4 Electrodeposition from [BMP][DCA] and [BMP]Cl mixture

In order to prevent polymerization of dicyanamide anions at the anode, various additives were tested to suppress the polymerization reaction. [BMP]Cl is a good candidate because the chloride ions can be oxidized to chlorine gas at the anode and it has the same cations as [BMP][DCA]. [BMP]Cl and [BMP][DCA] were used in a 1:1 molar ratio. This mixture was a gel at room temperature, but it became a clear liquid at higher temperatures. It was not possible to determine an accurate melting point by DSC, but to be sure that the ionic liquid was totally molten, the mixtures were used at 100 °C. The electrochemical window of the mixture is about 2.9 V, from -1.6 V to +1.3 V (vs. Ge) at 100 °C (Figure

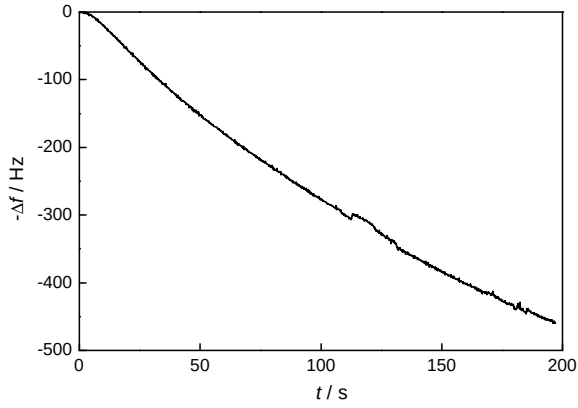

Figure 4.14: Frequency change on a platinum coated EQCM crystal in neat [BMP][DCA] at room temperature, and a constant current 0.05 A dm^{-2} was applied. The counter and reference electrodes were platinum.

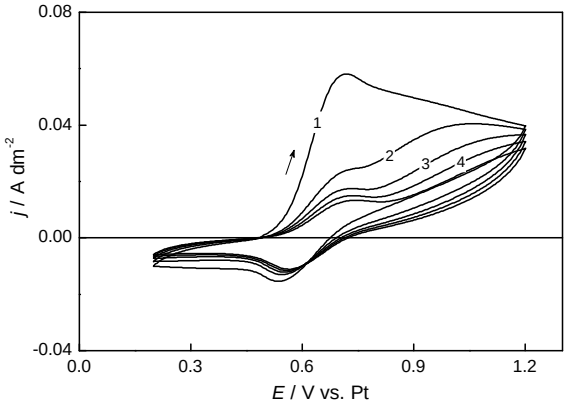

Figure 4.15: Sequential cyclic voltammograms of a 0.05 M ferrocene solution in [BMP][DCA] on a platinum disk (ϕ = 1 mm) at room temperature. The counter and reference electrodes were platinum and the scan rate was 5 mV s^{-1}.

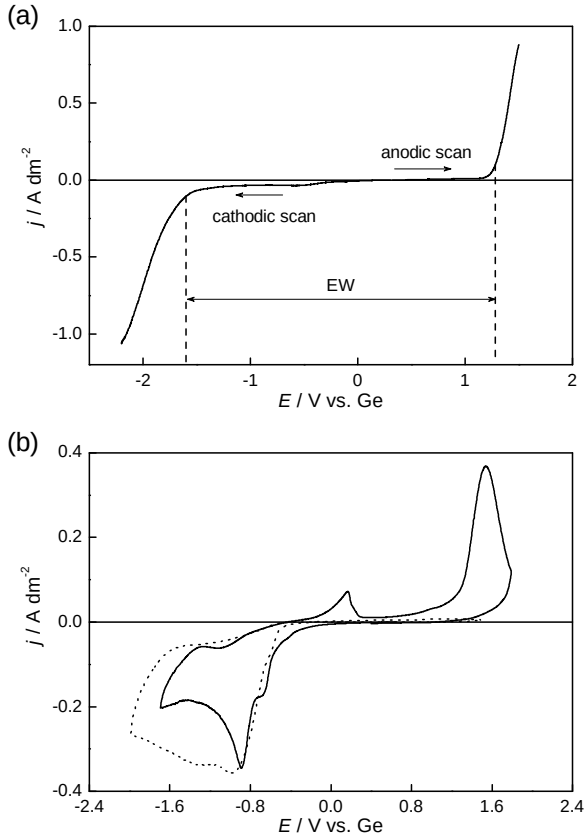

Figure 4.16: Voltammograms of [BMP][DCA] and [BMP]Cl mixture (1:1 molar ratio) (a) and cyclic voltammogram of 0.1 M $[GeCl_4(BuIm)_2]$ in [BMP][DCA] and [BMP]Cl mixture (molar ratio 1:1) at 100 °C (b). The working electrode was platinum (solid lines) or silicon (dotted line), and the counter and reference electrodes were n-type germanium and the scan rate was 25 mV s^{-1}.

4.16 a). The increase of the anodic current is due to the breakdown of the ionic liquids.

Figure 4.16b (solid line) shows the cyclic voltammogram of 0.1 M $[GeCl_4(BuIm)_2]$ in the [BMP][DCA] and [BMP]Cl. The reduction peak at about -0.8 V (vs. Ge) corresponds to the deposition of germanium, and the oxidation peak at the +1.5 V (vs. Ge) is due to breakdown of the ionic liquids. Figure 4.17 shows the germanium films deposited from the 0.1 M and the 0.2 M $[GeCl_4(BuIm)_2]$ in the mixture of [BMP][DCA] and [BMP]Cl. These films have a similar morphology

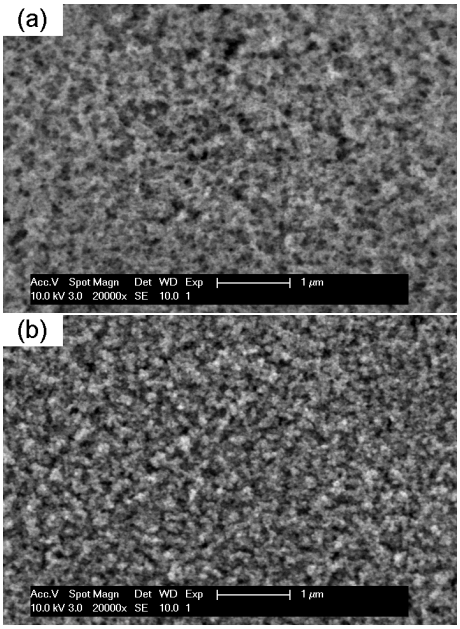

Figure 4.17: SEM images of the germanium film deposited on copper disks from 0.1 M (a) and 0.2 M (b) $[GeCl_4(BuIm)_2]$ in 1:1 molar ratio [BMP][DCA] and [BMP]Cl at 100 °C, applied potential: -0.65 V (vs. Ge), theoretical thickness: 0.68 µm (a) and 1.0 µm (b), the counter electrode was an n-type germanium wafer. The solution was stirred with a magnetic stirrer bar during deposition.

as the films electrodeposited from [BMP][DCA] solution. Because of the high deposition temperature (100 °C), the average current density was -0.084 A dm^{-2} at a constant potential of -0.65 V (vs. Ge) in 0.1 M solution and -0.16 A dm^{-2} in 0.2 M solution. Many gas bubbles were formed around the counter electrode during deposition, and after electrodeposition the germanium counter electrode appeared rough. Moreover, the potential between working and counter electrodes remained constant during the potentiostatic deposition, indicating that no poorly conductive layer was formed at the anode. Hence the presence of chloride ions in the solution suppressed the polymerization of the dicyanamide anion at the anode.

Electrodeposition of germanium films on silicon. Germanium films were electrodeposited on n-type silicon substrates from a 0.1 M solution of $[GeCl_4(BuIm)_2]$ in the mixture of [BMP][DCA] and [BMP]Cl, with a molar ratio of 1:1. 18-Crown-6 and KF were added in a 50 mM concentration to the electrolyte solution to prevent the formation of an oxidation layer on the

silicon surface by forming volatile SiF_4. 18-Crown-6 allows solubilization of KF in the organic electrolyte and it promotes the dissociation of KF in K^+ ions (bonded by 18-crown-6) and naked F^- ions. The dotted line in Figure 4.16b shows the cyclic voltammogram of the solution on a silicon substrate. There is a clear reduction peak at -1.0 V (vs. Ge) due to the deposition of germanium. However there is no increase in current during the anodic scan. This is because the silicon electrode is an n-type semiconductor, and a depletion region arises due to the applied positive potential [93]. Hot entry (apply potential before immersing working electrode into the solution) was applied for deposition and black germanium films were deposited on silicon. The average current density was about -0.023 A dm^{-2} at a constant potential of -0.75 V (vs. Ge). The film has a similar morphology to the ones deposited on copper substrate. These experiments show that germanium films can be directly electrodeposited on n-type silicon substrates, but no epitaxial growth was observed.

4.4 Conclusions

We have presented a systematic study of germanium electrodeposition from a solution of $[GeCl_4(BuIm)_2]$ in the ionic liquid [BMP][DCA] and in a mixture of [BMP][DCA] and [BMP]Cl (1:1 molar ratio). Uniform and porous germanium films could be obtained from the ionic liquid [BMP][DCA] containing up to 0.47 M of the germanium complex $[GeCl_4(BuIm)_2]$. In the 0.1 M $[GeCl_4(BuIm)_2]$ solution, Ge(IV) ion has a diffusion coefficient of 3.0 10^{-12} m^2 s^{-1} at 50 °C and the exchange current density is 16 A m^{-2}. Cyclic voltammograms show two reduction waves: the first one at more positive potential corresponds to the reduction of Ge(IV) to Ge(II), and the second peak at more negative potential is assigned to Ge(II) to Ge(0). The small oxidation peak on the reverse scan is attributed to the oxidation of Ge(II) to Ge(IV). During electrodeposition, polymerization of the dicyanamide anion takes place at the anode and it forms a poorly conductive organic layer. The polymerization can be suppressed by adding [BMP]Cl to the solution of [BMP][DCA]. Porous, yet uniform, germanium films can be electrodeposited from the mixture of [BMP][DCA] and [BMP]Cl on copper and n-type silicon wafers.

Chapter 5

Electrodeposition of germanium at elevated temperatures and pressures

This chapter is adapted from:

M. Wu, G. Vanhoutte, N. R. Brooks, K. Binnemans and J. Fransaer, Electrodeposition of germanium at elevated temperatures and pressures, *Phys. Chem. Chem. Phys*, **17**, 12080–12089 (2015). – Reproduced by permission of the PCCP Owner Societies.

(Scientific contribution: most of the experiments, data analysis and writing the first draft.)

Abstract

The electrodeposition of germanium at elevated temperatures up to 180 °C and pressures was studied from the ionic liquids 1-butyl-1-methylpyrrolidinium dicyanamide and 1-butyl-1-methylpyrrolidinium bis(trifluoromethylsulfonyl)-imide containing $[GeCl_4(BuIm)_2]$ (where BuIm = 1-butylimidazole) or $GeCl_4$. Cyclic voltammetry (CV), electrochemical quartz crystal microbalance (EQCM), rotating ring-disk electrode (RRDE), scanning electron microscope (SEM), X-ray diffraction (XRD), transmission electron microscopy (TEM), electron backscatter diffraction (EBSD) and Auger electron spectroscopy (AES) were used to investigate the electrochemical behavior and the properties of the electrodeposited germanium. Electrodeposition at elevated temperatures leads to higher deposition rates due to: (1) increase in the diffusion rate of the electroactive germanium compounds; (2) faster electrochemical kinetics in the electrolyte; and (3) higher electrical conductivity of the electrodeposited germanium film. Moreover, the morphology of the germanium film is also of a better quality at higher electrodeposition temperatures due to an increase in adatom mobility.

5.1 Introduction

The electrodeposition of germanium thin films is receiving a lot of attention from the scientific community, thanks to the importance of germanium in semiconductor applications [70, 183, 92, 90]. Thin films of germanium can be fabricated from various solutions using electrodeposition. Due to the low overpotential for hydrogen evolution on germanium electrodes, only ultrathin germanium layers could be obtained from aqueous solutions [162, 73, 65]. Grey shiny germanium films were electrodeposited from organic solvents, e.g. ethylene glycol, propylene glycol, etc [62, 72, 163]. However, the current efficiency for electrodeposition from protic organic electrolytes such as ethylene glycol and propylene glycol is very low due to formation of hydrogen gas. To avoid hydrogen evolution, electrolytes based on supercritical fluids or ionic liquids are gaining more and more interest [92, 170].

Ionic liquids are solvents that consist entirely of ions. They have a wide electrochemical window and an intrinsic ionic conductivity [74, 75]. Using ionic liquids as electrolytes and performing electrodeposition from ionic liquids has been a hot research topic during last decade. Some metals that are impossible to deposit from water due to hydrolysis or due to the fact that hydrogen evolution happens before metal ion reduction can be electrodeposited from ionic liquids because water can be easily removed [79]. Endres and coworkers first reported on germanium electrodeposition from the ionic liquid 1-butyl-3-methylimidazolium hexafluorophosphate using germanium(IV) halides as germanium source [80, 81, 82, 83]. Germanium nanoclusters were obtained, but carbon, oxygen and halogen impurities were detected in the deposits. Germanium has also been electrodeposited from other ionic liquids, e.g. 1-butyl-3-methylimidazolium bis(trifluoromethylsulfonyl)imide, 1-butyl-1-methylpyrrolidinium bis(trifluoromethylsulfonyl)imide, 1-ethyl-2,3-dimethylimidazolium bis(trifluoromethylsulfonyl)imide [85, 86, 87]. Due to the low boiling point of $GeCl_4$ (86.5 °C), most of the depositions have been carried out at room temperature. Xin *et al.* performed Si_xGe_{1-x} deposition from 1-ethyl-3-methylimidazolium bis(trifluoromethylsulfonyl)imide using $GeCl_4$ and $SiCl_4$ at 90 °C and found a 2D-ordered Si_xGe_{1-x} deposit at 90 °C instead of the 3D structure that was formed at room temperature [184]. The film morphology was improved due to the increase of adatom mobility on the surface at elevated temperatures [185]. To prevent the evaporation of the electroactive germanium compound, we used a new germanium compound $[GeCl_4(BuIm)_2]$ (where BuIm = 1-butylimidazole), which is much less volatile than $GeCl_4$, and successfully electrodeposited porous germanium films from a mixture of 1-butyl-1-methylpyrrolidinium dicyanamide and 1-butyl-1-methylpyrrolidinium chloride at 100 °C [186]. The deposition rate at 100 °C was much higher than

at room temperature. Because at elevated temperatures, both the diffusion rate of germanium ions and electrochemical kinetics are increased. Also, the electrical conductivity (σ) of electrodeposited germanium film also increased at higher temperatures as $\sigma \propto \exp(-E_g/2k_BT)$, where E_g is the band gap of the material, k_B is the Boltzmann constant, and T is the absolute temperature [187].

This paper is about the electrodeposition of germanium at elevated temperatures up to 120 °C from 1-butyl-1-methylpyrrolidinium dicyanamide and up to 180 °C from 1-butyl-1-methylpyrrolidinium bis(trifluoromethylsulfonyl)imide. To prevent the evaporation of $[GeCl_4(BuIm)_2]$ and $GeCl_4$, a high pressure electrochemical cell was built. At temperatures higher than 150 °C, dense shiny germanium films could be electrodeposited and high deposition rates could be obtained.

5.2 Experimental

The ionic liquids 1-butyl-1-methylpyrrolidinium bis(trifluoromethylsulfonyl)-imide [BMP][Tf_2N] (IoLiTec, > 98%) and 1-butyl-1-methylpyrrolidinium dicyanamide [BMP][DCA] (IoLiTec, > 98%) were thoroughly dried in a vacuum of 0.6 mbar at 120 °C for at least 8 h. $GeCl_4$ (Umicore, Olen, Belgium, 99.99%) was used as received. $[GeCl_4(BuIm)_2]$ was synthesized according to a literature procedure [186].

The electrolyte solutions were prepared in an argon-filled glove box (oxygen and water contents were below 1 ppm), and then the electrolytes were transferred into a closed pressure cell. The schematic drawing of the pressure electrochemical cell is shown in Figure 5.1. It was a cylindrical glass cell with a screw cap. The electrochemical experiments were performed outside the glove box and the closed cell was entirely immersed in a hot silicon oil bath. All the electrochemical experiments were carried out in a three-electrode system. The counter electrode was a p-type germanium wafer and a platinum wire was used as a pseudo-reference electrode. The working electrode used for cyclic voltammetry and for linear scan voltammetry experiments was a polished platinum disk ($\phi = 1$ mm) embedded in EpoFix® resin. In rotating ring-disk electrode experiments, a platinum/platinum rotating ring-disk electrode (Pine Research Instrumentation, E7R8 Series) was used as working electrode. The dimensions of the ring and disk electrodes were provided by the supplier. The disk has a diameter of 4.57 mm ($2r_1$), and the inside and outside diameters of the ring are 4.93 mm ($2r_2$) and 5.38 mm ($2r_3$), respectively. The collection efficiency of the electrode N_0 was experimentally measured in a solution containing either 4.93

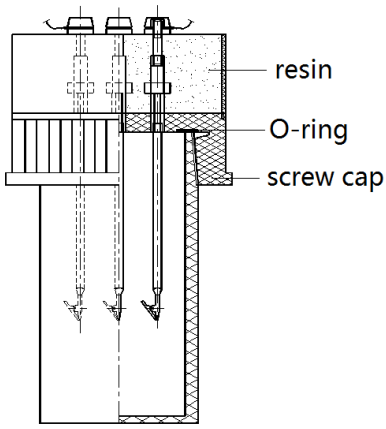

Figure 5.1: Schematic drawing of the electrochemical cell used for electrochemical experiments at elevated temperatures.

mM $K_3[Fe(CN)_6]$ or 4.86 mM $K_4[Fe(CN)_6]$ and 20 mM KOH at 30 °C and it is 24.5%. Platinum-coated silicon wafers (silicon covered with 500 nm of silica, 10 nm of titanium and 100 nm of platinum) or n-type germanium wafers (Umicore, Cz88 742) were used as working electrode for germanium deposition. Before electrodeposition, all the substrates were rinsed with deionized water and absolute ethanol and finally dried in a stream of hot air. An EG&G 273 or an Autolab 302N potentiostat was used for electrochemical experiments.

The electrochemistry of germanium deposition in $[BMP][Tf_2N]$ was studied by electrochemical quartz crystal microbalance (EQCM, Maxtek). The mass change per unit area ($\triangle m$) on a platinum-coated 5 MHz quartz crystal was determined by the Sauerbrey equation:

$$\Delta f = -C_f \Delta m \tag{5.1}$$

where Δf is the frequency change; and C_f is the sensitivity factor of the crystal, which was calibrated as 6523 Hz g^{-1} m^2 in $[BMP][Tf_2N]$ solutions. The calibration was done according to the method described by Gabrielli *et al.* [142]. A solution of 50 mM $[Ag(MeCN)_4]_2[Ag(Tf_2N)_3]$ in $[BMP][Tf_2N]$ was used for calibration, and deposition was done at a constant potential. The sensitivity factor was calculated using the Sauerbrey equation by assuming the current efficiency for silver deposition in this solution is 100%. $[Ag(MeCN)_4]_2[Ag(Tf_2N)_3]$ was chosen because it has higher solubility in

[BMP][Tf_2N] than $AgNO_3$. It was prepared according to a literature procedure [188, 78].

The concentration of [BMP][Tf_2N] containing $GeCl_4$ was determined using inductively coupled plasma optical emission spectroscopy (ICP-OES, Varian 720-ES). Because [BMP][Tf_2N] is immiscible with water, methanol was added to make the ICP solutions. The morphology and elemental composition of the films were determined by scanning electron microscopy (SEM) and energy-dispersive X-ray spectroscopy (EDX, Philips XL 30 FEG). X-ray diffraction (XRD, Seifert 3003), transmission electron microscopy (TEM, FEI Tecnai G2 F20) and electron backscatter diffraction (EBSD) were used to characterize the crystal structure of the deposits. TEM sample was prepared with focused ion beam (FIB, FEI Helios). EBSD was performed using a TSL-EDAX system on an FEI Nova 600 NanoLab instrument. The cross-sections for EBSD measurement and SEM were prepared using a JEOL cross-section polisher.

Auger electron spectroscopy (AES) was used for analyzing the carbon impurity in the germanium film. The Auger chamber (Thermo Scientific) was under ultrahigh vacuum (8.9 10^{-9} Torr) and spectra were measured using a primary electron beam with an energy of 8 keV with a typical current of 10 nA and a Gaussian profile with a radius of about 0.5 mm. Auger electrons were detected with a hemispherical analyzer (Thermo Scientific) in an energy range from 100 eV up to 1500 eV. Depth profiling was done by sputtering with an argon ion beam for 5 min between each AES measurement. The sputter beam current was approximately 3 µA, and the beam size had a Gaussian profile with a diameter of approximately 1 mm and was scanned over an area of 2 × 2 mm^2. AES spectra was analyzed using Avantage Data System software (Thermo Scientific).

5.3 Results and discussion

5.3.1 Electrodeposition of germanium using [$GeCl_4$(BuIm)$_2$]

In the authors' previous experiments, uniform and porous germanium films could be electrodeposited from 0.1 M [$GeCl_4$(BuIm)$_2$] in [BMP][DCA] at room temperature [186]. The deposition rate was calculated from the mass change on a electrochemical quartz crystal microbalance and it was 0.87 µm h^{-1}. Efforts to increase the deposition rate were made by increasing the [$GeCl_4$(BuIm)$_2$] concentration to 0.4 M in [BMP][DCA]. Unfortunately, due to the high viscosity of the solution, the deposition rate did not significantly increase [186]. To increase the deposition rate, a [BMP][DCA] solution containing 0.4 M [$GeCl_4$(BuIm)$_2$] was heated to 120 °C. Germanium films were electrodeposited

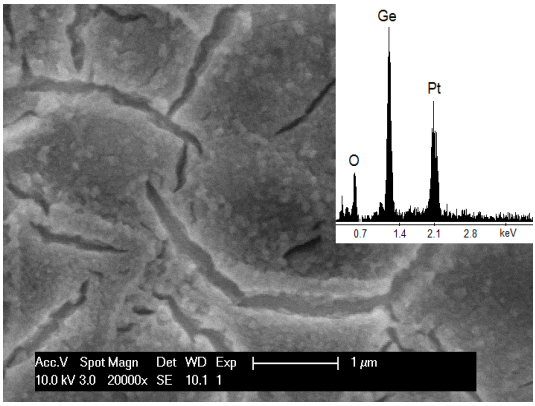

Figure 5.2: SEM image and EDX spectrum of the germanium film electrodeposited at -1.6 V from 0.4 M $[GeCl_4(BuIm)_2]$ in [BMP][DCA] at 120 °C. The working electrode was a platinum wafer, the counter electrode was a p-type wafer and the reference electrode was a platinum wire. The solution was stirred with a magnetic stirrer bar during electrodeposition.

at different potentials. The film deposited at -1.6 V (vs. Pt) had an orange color and showed many cracks on the surface (Figure 5.2). The EDX spectrum of the deposit showed the film also contains a considerable amount of oxygen. Due to the bad adhesion between the germanium film and platinum substrate, the germanium film pealed off during ultrasonic cleaning. The theoretical deposition rate was calculated from the applied charge based on Faraday's law and it reached 2.0 µm h^{-1}. This value is close to the germanium deposition rate reported in propylene glycol containing 5 vol% $GeCl_4$ ($\sim$ 2.2 µm h^{-1}) [163]. However, due to the polymerization of dicyanamide anions, the solution darkened and became more viscous during the electrodeposition process. Polymerization of [BMP][DCA] is caused, not only by applied electrical current, but also by the high temperature [189, 190]. Figure 5.3 shows the color of pure [BMP][DCA] after heating at 140 °C for different times. The solution turned darker at longer heating times, indicating that the polymerization took place during heating. The discoloration at elevated temperature is similar to the one due to the applied electrical charge [186]. The increase in viscosity due to the polymerization led to a decrease of the deposition rate. Because of the fast polymerization $[DCA]^-$ ions, germanium films could not be obtained at temperatures higher than 140 °C from [BMP][DCA].

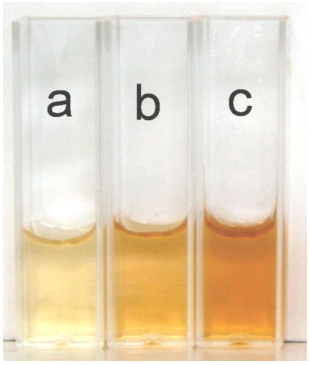

Figure 5.3: Color changes of pure [BMP][DCA] after heating at 140 °C for different times: (a) 0 h, (b) 20 h, and (c) 72 h.

5.3.2 Electrodeposition of germanium using $GeCl_4$

$GeCl_4$ has a high solubility in [BMP][Tf_2N]. A [BMP][Tf_2N] solution containing 0.5 M was used for deposition of germanium. However, due to the low boiling temperature of $GeCl_4$ (86.5 °C), the loss of $GeCl_4$ in [BMP][Tf_2N] at elevated temperatures is significant. The evaporation of $GeCl_4$ even occurred at room temperature as detected by ICP-OES. After exposing the solution in argon atmosphere for 30 min, the concentration of $GeCl_4$ in [BMP][Tf_2N] decreased to 0.37 M. The solution was further heated at 150 °C for one hour, and then no germanium trace was found in the solution, which means all $GeCl_4$ has evaporated. To prevent the loss of germanium, a three-electrode pressure cell which could be totally sealed was designed and used for $GeCl_4$ solutions in [BMP][Tf_2N] at higher temperatures (Figure 5.1). When the temperature increased, the evaporation of $GeCl_4$ leads to an increase in the pressure above the solution (autogenerated $GeCl_4$ atmosphere), preventing the further loss of $GeCl_4$. The pressure change with temperature can be calculated from the Clapeyron equation:

$$\ln\left(\frac{P_2}{P_1}\right) = \frac{\triangle H_v}{\mathrm{R}}\left(\frac{1}{T_1} - \frac{1}{T_2}\right) \tag{5.2}$$

where P is the pressure (Pa), $\triangle H_v$ is the molar heat of evaporation (J mol^{-1}), R is the gas constant (8.314 J K^{-1} mol^{-1}), and T is the temperature (K). The pressure calculated based on equation 5.2 at different temperatures is shown in Figure 5.4. Laubengayer *et al.* showed that the actual experimental pressures agreed with the calculated [191]. At 150 °C, the pressure is expected to increase to about 4 bar.

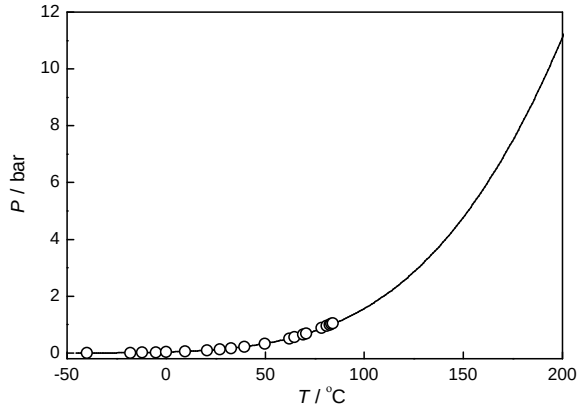

Figure 5.4: Vapor pressure of $GeCl_4$ as a function of temperature. The black line was calculated based on equation 5.2 and the circles are the experimental data from the literature [191].

The viscosity and density of [BMP][Tf_2N] change with temperature. The density of [BMP][Tf_2N] at different temperatures was described in the literature [192, 193]. The kinematic viscosity (ν) of pure [BMP][Tf_2N] was measured at different temperatures and was converted to dynamic viscosity (Figure 5.5, Table 5.1). The viscosity non-linearly decreases with increasing temperatures. This nonlinear effect could be described by the Tammann-Vogel-Fulcher (TVF) equation:

$$\log \mu = \log \mu_0 - B/(T - T_0) \tag{5.3}$$

where μ is the dynamic viscosity (Pa s), T is temperature (K), μ_0, B and T_0 are adjustable parameters. μ_0 is the viscosity at infinite temperature, T_0 is the temperature at which the viscosity become infinite, and parameter B corresponds to the pseudo-activation energy associated with viscous flow [194]. The best fit for μ_0, B and T_0 are 1.24 10^{-5} Pa s, 25.1 K and 7.4 K, respectively. The decrease in viscosity of [BMP][Tf_2N] at higher temperatures promotes the diffusion of $GeCl_4$ which means that germanium can be electrodeposited at a high current density, but in order to reach these higher temperatures a pressurized cell must be used.

Figure 5.6a shows the cyclic voltammograms of 0.5 M $GeCl_4$ in [BMP][Tf_2N] at room temperature. The cyclic voltammograms were stopped at cathodic vertex potentials of -1.0 V, -1.2 V, -1.5 V, -1.7 V, -2.0 V and -2.5 V to study the reactions happening at different potentials. There are two reduction peaks on the cathodic scan and three oxidation waves on the anodic scan. The second oxidation peak a2 correlated to the first reduction peak r1 at -1.1 V. The peak

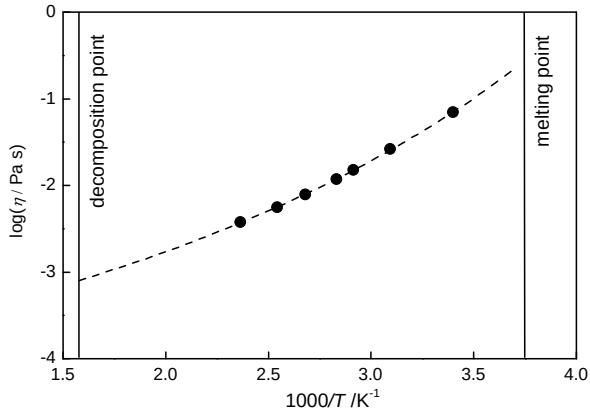

Figure 5.5: Tammann-Vogel-Fulcher fitting of viscosity change of ionic liquid [BMP][Tf_2N] with temperature.

Table 5.1: Viscosity of [BMP][Tf_2N] at different temperatures

T (°C)	ν (10^{-6} m^2 s^{-1})	μ (10^{-3} Pa s)
21	49.9	69.7
50	19.1	26.3
70	11.0	14.9
80	8.8	11.8
100	5.9	7.8
120	4.3	5.6
150	2.9	3.8

current density of a2 increased as more negative cathodic vertex potential was applied. The first reduction peak r1 is due to the reduction of Ge(IV) to Ge(II). This was further proven using a potential scan experiment: a constant potential of -1.0 V was applied until the charge density reached 2 C dm^{-2}. Ge(II) ions were formed at the working electrode. Then the potential was scanned from -1.0 V to +1.5 V after waiting at open circuit potential for different times (0 s, 10 s, 30 s and 300 s). With longer waiting time, more Ge(II) ions diffused away from working electrode. The oxidation peak a2 which was due to the oxidation of Ge(II) to Ge(IV) decreased as longer waiting times were applied (Figure 5.7). When an even more negative cathodic vertex potential was applied, the second oxidation peak a2 decreased, less Ge(II) was in the solution because at the second reduction peak r2 Ge(II) was further reduced to Ge(0). The oxidation peak a3 corresponds to the oxidation of chloride ions to chlorine gas ($E^0_{Cl_2/Cl^-}$=+1.36 V vs. SHE). Chloride ions are present in solution after

reduction of $GeCl_4$ to Ge(0). The oxidation potential of chloride ions was determined using a [BMP][Tf_2N] solution containing 0.4 M [BMP]Cl. Figure 5.8 shows the linear sweep voltammograms of 0.4 M [BMP]Cl in [BMP][Tf_2N]. An oxidation peak could be observed at +1.07 V which was due to the oxidation of chloride ions to chlorine gas. This peak is not present in pure [BMP][Tf_2N]. The first oxidation peak a1 appeared only when the cathodic potential was scanned to the second reduction peak r2, indicating a1 was due to the stripping of Ge(0).

When the cell was immersed in the heating bath to 150 °C some gas bubbles were formed in the solution due to the high volatility of the $GeCl_4$. The formation of gas bubbles stopped when the final temperature was reached. The cyclic voltammogram of 0.5 M $GeCl_4$ in [BMP][Tf_2N] at 150 °C is quite similar to the cyclic voltammogram at room temperature (Figure 5.6b). There are two reduction peaks on the cathodic scan. The first one at -1.25 V is due to the reduction of Ge(IV) to Ge(II), and the second reduction peak at -2.1 V corresponds to the deposition of Ge(0). The peak current density is -4.2 A dm^{-2} compared to -1.3 A dm^{-2} at room temperature. The increase in the current density is due to the reduction of the viscosity at elevated temperatures. The decrease in viscosity leads to an increase in diffusion coefficient of Ge(IV) ions in [BMP][Tf_2N]. The diffusion coefficient of Ge(IV) was calculated based on the following equations [195]:

$$j_{\mathrm{p}} = 0.496 z \mathrm{F} c \left(\frac{\alpha z_a \mathrm{F} v D}{\mathrm{R} T} \right)^{\frac{1}{2}} \tag{5.4}$$

$$E_{\mathrm{p}} - E_{\mathrm{p}/2} = -\frac{47.7}{\alpha z_a}\,\mathrm{mV} \tag{5.5}$$

where F is the Faraday constant, j_{p} is peak current density (A m^{-2}), z is the total number of electrons involved in the overall process, z_a is number of electrons involved in the rate determine step reaction, α is the charge transfer coefficient, c is the concentration (mol m^{-3}), v is the scan rate (V s^{-1}), D is the diffusion coefficient (m^2 s^{-1}), E_p is the peak potential, and $E_{\mathrm{p}/2}$ is the half peak potential. Cyclic voltammetry was performed in the potential range of the first reduction peak where Ge(IV) is reduced to Ge(II) with different scan rates and the peak current density was plotted versus the square root of the scan rate v (Figure 5.9). The diffusion coefficient of Ge(IV) in [BMP][Tf_2N] at room temperature (22 °C) and 150 °C are 9.0 10^{-12} m^2 s^{-1} and 1.9 10^{-10} m^2 s^{-1}, respectively, meaning that the diffusion coefficient at 150 °C is 22 times larger than that at room temperature. This is in close correspondence to the Stokes-Einstein relation:

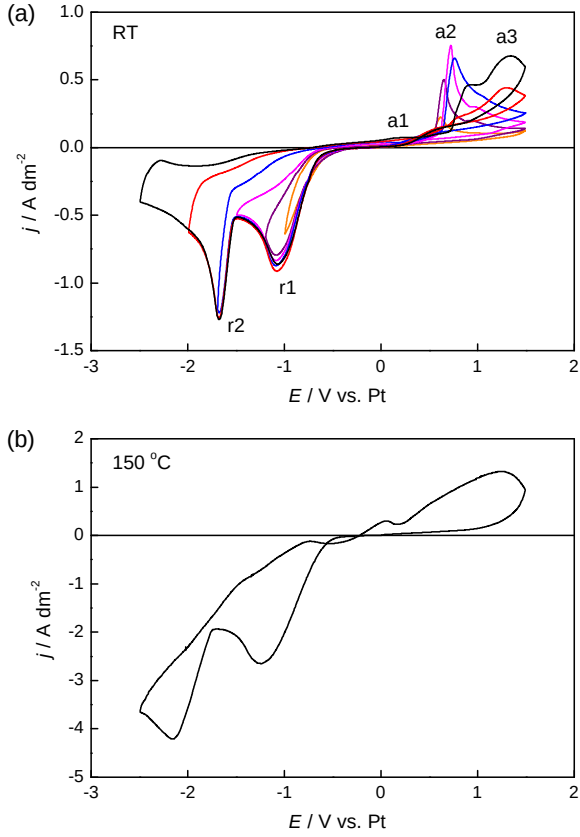

Figure 5.6: Cyclic voltammograms of 0.5 M $GeCl_4$ in [BMP][Tf_2N] at (a) room temperature and (b) 150 °C. At room temperature, the cyclic voltammetry stopped at different cathodic vertex potentials of -1.0 V, -1.2 V, -1.5 V, -2.0 V and -2.5 V. The working electrode was a platinum disk ($\phi = 1$ mm) and the counter electrode was a p-type germanium wafer. The scan rate was 50 mV s^{-1}.

$$D = \frac{k_B T}{6\pi\mu r} \tag{5.6}$$

where k_B is Boltzmann's constant, μ is the dynamic viscosity (Pa s), and r is the hydrodynamic radius (m) of the diffusing species. The dynamic viscosity of the ionic liquid [BMP][Tf_2N] at room temperature is 18 times larger than that at 150 °C, and the diffusion coefficient is 26 times higher at 150 °C than that at room temperature.

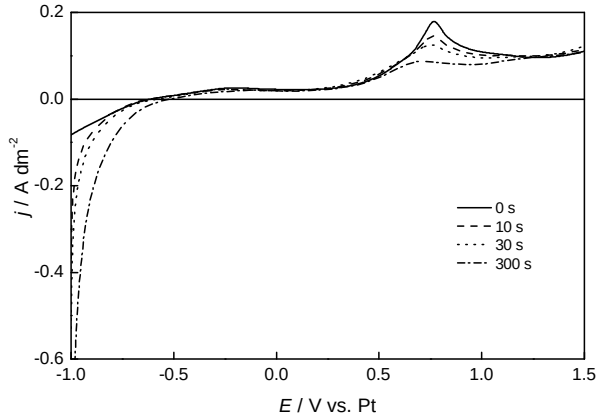

Figure 5.7: Linear scan voltammograms of [BMP][Tf_2N] solution containing 0.5 M $GeCl_4$ at room temperature. The working electrode was a platinum disk (ϕ = 1 mm) which was polarized at -1.0 V with the charge of -2 C dm^{-2} and then kept at open circuit potential for different times of 0 s, 10 s, 30 s and 600 s before performing LSV. The counter electrode was a platinum coil.

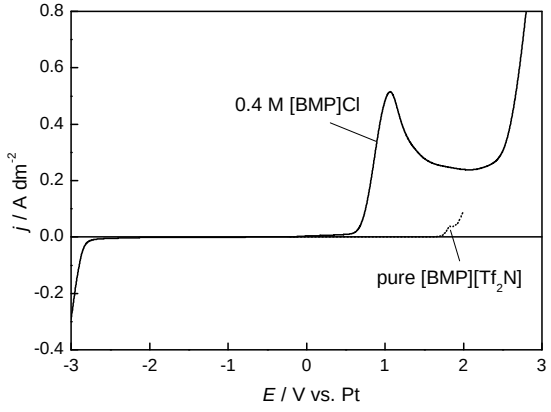

Figure 5.8: Linear sweep voltammograms of 0.4 M [BMP]Cl in [BMP][Tf_2N] (solid line) and pure [BMP][Tf_2N] (dotted line) at room temperature. The working electrode was a platinum disk ($\phi = 1$ mm), the counter electrodes was a platinum coil. The scan rate was 50 mV s^{-1}.

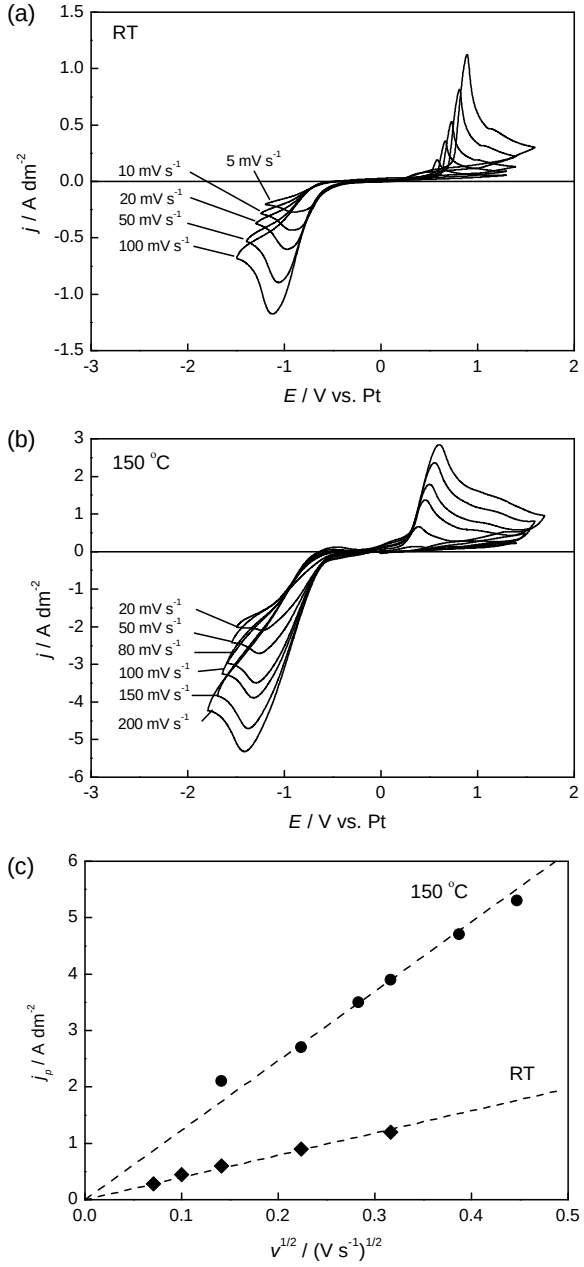

Figure 5.9: Cyclic voltammograms of 0.5 M $GeCl_4$ in [BMP][Tf_2N] with different scan rates at (a) room temperature and (b) 150 °C, and (c) the plot of current density versus the square root of the scan rate v.

The electrochemical behavior of [BMP][Tf_2N] solution containing $GeCl_4$ was further studied using *Electrochemical Quartz Crystal Microbalance* (EQCM). As shown in Figure 5.10a, a cyclic voltammogram was recorded on a platinum-coated EQCM crystal working electrode, and the corresponding frequency change was simultaneously recorded by EQCM. Based on the frequency change, the mass change on the crystal was calculated from the Sauerbrey equation. The M/z value was calculated at different potential ranges (Figure 5.10b) and it varies for different reactions:

$$\mathrm{Ge(IV)} + 2\mathrm{e}^- \rightarrow \mathrm{Ge(II)} \qquad \frac{M}{z} = 0 \tag{5.7}$$

$$\mathrm{Ge(IV)} + 4\mathrm{e}^- \rightarrow \mathrm{Ge(0)} \qquad \frac{M}{z} = 18.2 \text{ g mol}^{-1} \tag{5.8}$$

$$\mathrm{Ge(II)} + 2\mathrm{e}^- \rightarrow \mathrm{Ge(0)} \qquad \frac{M}{z} = 36.3 \text{ g mol}^{-1} \tag{5.9}$$

The first reduction peak was assigned to the reduction of Ge(IV) to Ge(II). Thus, no mass increase was expected at this potential range. However a small mass increase was observed and the increase of mass stopped when reached a certain value. This is consistent with the observation of Endres and co-workers using a scanning tunneling microscope (STM) [81]. They found the growth of germanium islands at the beginning of the first reduction peak and the formation of a coherent, closed germanium layer when the potential was scanned to slightly more negative values than the first reduction peak. This layer hardly changed until the beginning of the second reduction peak [81]. Xie *et al.* explained that two electrochemical reactions take place at the first reduction peak: the reduction of Ge(IV) to Ge(II) and the underpotential deposition (UPD) of germanium [196]. At the second reduction wave, the potential is negative enough for reaction 5.9 to take place. In the beginning, the reduction rate of Ge(II) to Ge(0) was not fast enough to catch up with the rate of formation of Ge(II) so the M/z value increased from 0 to 65 g mol^{-1} as the potential scanned to more negative values. Based on equations 5.8 and 5.9, the M/z value should not exceed 36.3 g mol^{-1}. The morphology of the germanium film led to this abnormal increase in M/z value. Endres and co-workers found germanium nanoclusters forming during cathodic scan from ionic liquid 1-butyl-3-methylimidazolium hexafluorophosphate containing $GeCl_4$ [81]. The roughness of the germanium surface leads to the increase in frequency change which can be explained by several possible mechanisms [197]. This also can be seen from the ratio between resonance frequency change ($\triangle f$)

and resistance change ($\triangle R$) of the crystal [198]:

$$S_{\mathrm{q}} = \frac{\triangle f}{\triangle R} = \frac{32 f^3 A (\rho_{\mathrm{q}} e_{\mathrm{q}})^2}{2\pi (\rho_{\mathrm{q}} \mu_{\mathrm{q}})^{\frac{3}{2}}} \tag{5.10}$$

where f is the resonance frequency of a loaded crystal (Hz), A is the active area of the 1-inch crystal (3.419 10^{-5} m^2), ρ_{q} is the density of quartz (2.648 10^3 kg m^3), e_{q} is the piezoelectric constant for an AT cut quartz (0.095 kg s^2 V^{-1}), and μ_{q} is the shear modulus of quartz (2.947 10^{10} Pa). The S_{q} is calculated from the equation and it should be around 1.97 if the surface is absolute smooth. If the EQCM working surface is absolutely smooth, the S_{q} value is a constant. It increases proportional to the degree of surface roughness [199]. Figure 5.10c shows the resonance resistance change. The S_{q} value at -1.6 V was 2.5 and it increased to 11.5 at -2.5 V illustrating the fact that the electrodeposited germanium was rough.

On the cathodic back scan, a mass decrease was observed from -1.6 V on, due to the chemical dissolution of germanium deposit via the comproportionation reaction:

$$\mathrm{Ge(IV)} + \mathrm{Ge(0)} \rightleftharpoons 2\mathrm{Ge(II)}. \tag{5.11}$$

In order to exclude the effect of the ionic liquid on the dissolution of germanium film, two germanium films (8.9 C dm^{-2}) were electrodeposited from 0.1 M $GeCl_4$ in [BMP][Tf_2N] at -2.0 V at room temperature. Then they were immersed into two different solutions: (a) dried ionic liquid [BMP][Tf_2N], and (b) freshly prepared 0.1 M $GeCl_4$ in [BMP][Tf_2N]. After 12 hours, the germanium film in solution (b) was completely dissolved while the germanium film in the pure [BMP][Tf_2N] stayed intact even after 7 days. This suggests that the pure ionic liquid [BMP][Tf_2N] does not attack the germanium film and the germanium film dissolved only in the solution containing $GeCl_4$. The mass decrease during the cathodic scan was due to the comproportionation reaction (5.11). On the anodic scan, due to the chemical and electrochemical dissolution of germanium, the mass decreased. At potentials more positive than +0.8 V, a large anodic peak was observed, however there was almost no mass loss in that potential range. This suggests that the main oxidation peak does not correspond to the dissolution of germanium. This oxidation peak corresponded to the oxidation of chloride ions.

The rotating-ring disk electrode experiments provide clear evidence of the formation of Ge(II) at the first reduction peak. A cyclic voltammogram was performed on the disk and a constant potential of +1.3 V was applied on the ring (Figure 5.11). Under the assumption that Ge(IV) and Ge(II) do not form complexes with the anions of ionic liquid itself, the reactions at the disk are:

$$\mathrm{GeCl_4} + 2\mathrm{e}^- \rightleftharpoons \mathrm{GeCl_4^{2-}} \quad (\mathrm{r}'_1, \mathrm{r}'_2) \tag{5.12}$$

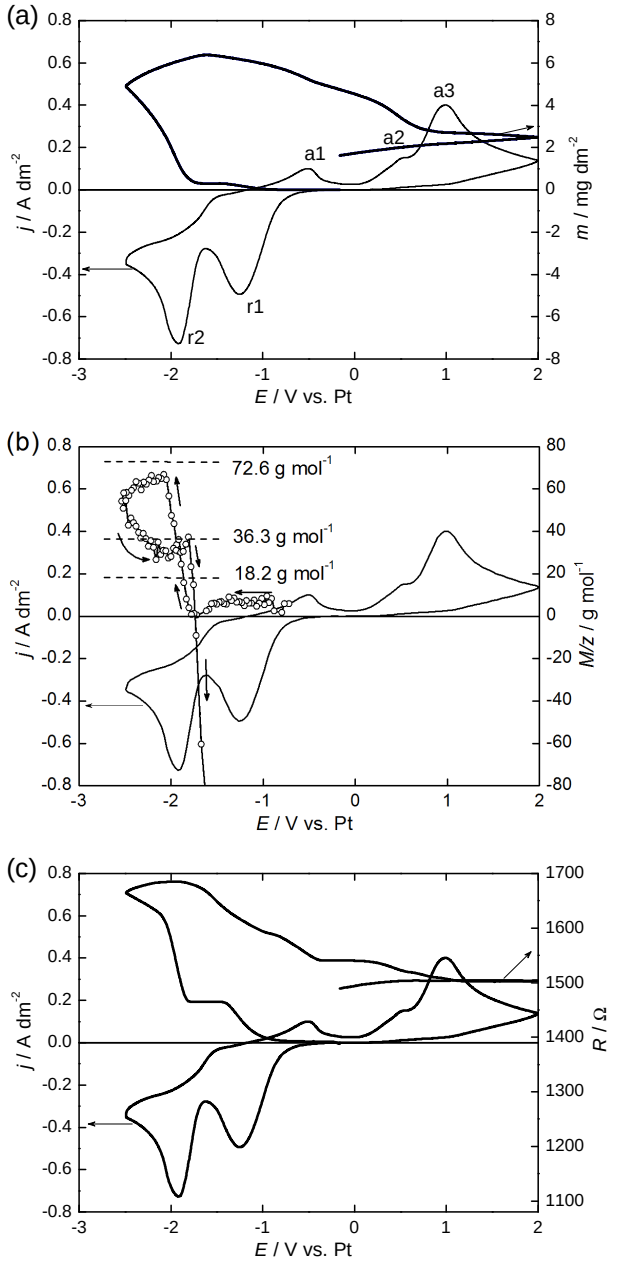

Figure 5.10: Cyclic voltammograms and corresponding (a) mass change, (b) M/z value change, and (c) resonance resistance change in a [BMP][Tf_2N] solution containing 0.1 M $GeCl_4$ at 50 °C. The counter electrode was a platinum coil and the scan rate was 50 mV s^{-1}.

$$GeCl_4^{2-} + 2e^- \rightleftharpoons Ge + 4Cl^- \quad (r_2') \tag{5.13}$$

and the reactions at the ring are:

$$GeCl_4^{2-} - 2e^- \rightleftharpoons GeCl_4 \qquad (a_1') \tag{5.14}$$

$$4Cl^- + 4e^- \rightleftharpoons 2Cl_2 \qquad (a_2') \tag{5.15}$$

At the first reduction plateau r'1 (-1.3 V– -1.4 V), $GeCl_4$ was reduced to $GeCl_4^{2-}$ and then $GeCl_4^{2-}$ convected to the ring and this $GeCl_4^{2-}$ was oxidized back to $GeCl_4$ on the ring. Thus, a corresponding current a'1 was observed on the ring. The ring-disk current ratio (i_{ring}/i_{disk}) N_{k1}in this potential range is 23.6% which is close to the collection efficiency measured from $K_3[Fe(CN)_6]$ solution: N_0 = 24.5% which indicates that no chloride ions were released at the first reduction plateau.

At the second reduction wave r'2 (-1.75 V – -2.0 V), $GeCl_4^{2-}$ was reduced to Ge, and no oxidation current is expected on the ring. However, an anodic current a'2 was observed. This is because chloride ions were liberated from the germanium complex when $GeCl_4^{2-}$ was reduced to Ge. The chloride ions were convected to the ring and were oxidized to chlorine gas. A ring-disk current ratio N_{k2} of 26.1% is found in this potential range which is close N_0. This suggests the ring reaction involves the same number of electrons as the disk reactions. The disk reactions involves overall four electrons and four chloride ions were released. Therefore, four electrons are involved in the reaction at the ring.

Due to the passivation of the electrode, the disk current decreased. At the third reduction plateau r'3, $GeCl_4$ was reduced to $GeCl_4^{2-}$ which is the same reaction on r'1, but the current is much lower. The current on the ring is due to the oxidation of $GeCl_4^{2-}$ to $GeCl_4$. However, the ring-disk current ratio (i_{ring}/i_{disk}) increases as the potential becomes more positive (Figure 5.11inset). It reaches 100% when the potential scans to -0.47 V. This indicates the ring current has two components: one is due to the oxidation of $GeCl_4^{2-}$ ions which are electrochemically reduced on the disk and the other is from the oxidation of $GeCl_4^{2-}$ ions that are chemically formed by the comproportionation reaction 5.11. When the disk current decreases to zero, a very small ring current of 2.5 µA still can be detected. This current is not present on the forward scan and it can be attributed to the oxidation of $GeCl_4^{2-}$ ions formed by comproportionation reaction. Based on that current and the collection efficiency, the dissolution rate of germanium due to the comproportionation was estimated as 0.36 µm h^{-1}. In order to prevent the oxidation of chloride ions on the ring, the ring potential was changed to +0.65 V where $GeCl_4^{2-}$ can be oxidized to $GeCl_4$ but not positive enough for oxidizing chloride ions. The result is shown in Figure 5.12. At the first reduction peak, a ring current was observed. The ring current

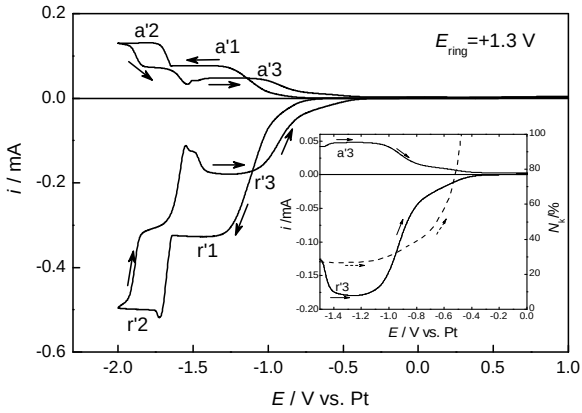

Figure 5.11: Rotating ring-disk electrode result from 0.5 M $GeCl_4$ in [BMP][Tf_2N] at room temperature: a cyclic voltammogram was applied on the disk at a scan rate of 2 mV s^{-1} and a ring potential of +1.3 V was applied. The rotation speed was 500 rpm. Solid lines: current, dashed lines: ring/disk current ratio N_k.

was lower than the limiting current and the collection efficiency is about 18.7%. This is because the applied potential was not positive enough. At the second reduction peak, the ring current dropped to zero.

Germanium films were electrodeposited from [BMP][Tf_2N] solutions at elevated temperatures in order to investigate their morphologies. Figure 5.13a shows the SEM pictures of the germanium film electrodeposited at 150 °C. The film was electrodeposited at -1.2 V with an average current density of -0.35 A dm^{-2}, and the theoretical thickness calculated from the charge was 4.8 µm. The germanium film had a very flat and uniform morphology, but there were a few cracks on the macroscale. In the EDX spectrum, a very small oxygen peak was observed which was due to the oxidation of germanium in the air. A chlorine peak was also found in the EDX. Endres and co-workers attributed the presence of chlorine to $GeCl_3$ termination of the deposit-electrolyte interface [83]. Figure 5.13c shows SEM picture of the germanium film electrodeposited at -0.9 V at 180 °C. The EDX spectrum for this film shows a very small oxygen peak and barely a chlorine peak. The film deposited at 180 °C had a grey but shiny metallic appearance, and no cracks were found in the film (Figure 5.14). The average current density was -0.46 A dm^{-2} and the theoretical thickness was 5.8 µm. Increasing the deposition temperature, not only increased the deposition rate, but also prevented the formation of cracks in the dense films. Dissolution of the p-type germanium anode was observed during electrodeposition. The

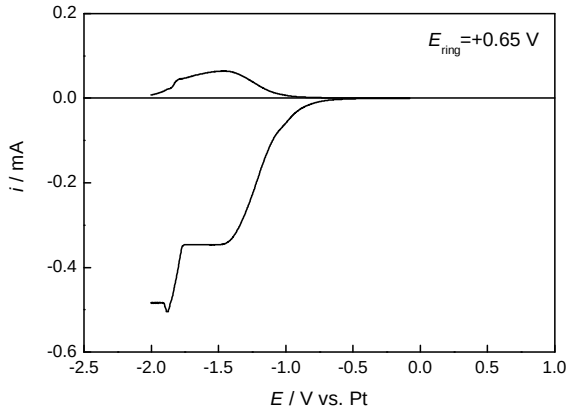

Figure 5.12: Rotating ring-disk electrode result from 0.5 M $GeCl_4$ in [BMP][Tf_2N] at room temperature: a cyclic voltammogram was applied on the disk at a scan rate of 2 mV s^{-1} and a ring potential of +0.65 V was applied. The rotation speed was 500 rpm.

surface of the germanium wafer became rough. The color of the solution did not change after electrodeposition.

The electrodeposited germanium film was removed from the substrate using resin and analyzed by XRD. No diffraction peaks were observed for the germanium film which indicates that the electrodeposited germanium on platinum was amorphous. When germanium was electrodeposited on a copper substrate, XRD diffraction peaks for Cu_3Ge alloy were observed. This suggests that electrodeposited germanium formed intermetallics with the copper substrate (Figure 5.15).

Maldonado and co-workers were the first to report the epitaxial electrodeposition of germanium nanowires from an aqueous solution, and their work required the formation of gallium nanodroplets [68]. In principle, at elevated temperature, due to the increase of the adatom mobility epitaxial growth of germanium on germanium substrate can be achieved if the surface of the germanium substrate is free of contaminations like oxides, grease, etc. The n-type germanium (100) substrates were rinsed with deionized water before using to remove most of the native oxides on the surface. Also, thanks to the comproportionation reaction (5.11), germanium substrates should be “self-cleaned" in the [BMP][Tf_2N] solution containing $GeCl_4$. This was supposed to prevent the existence of a native oxide layer between the germanium wafer and the electrolyte. However, the transmission electron microscopy (TEM) picture of the cross-section of the

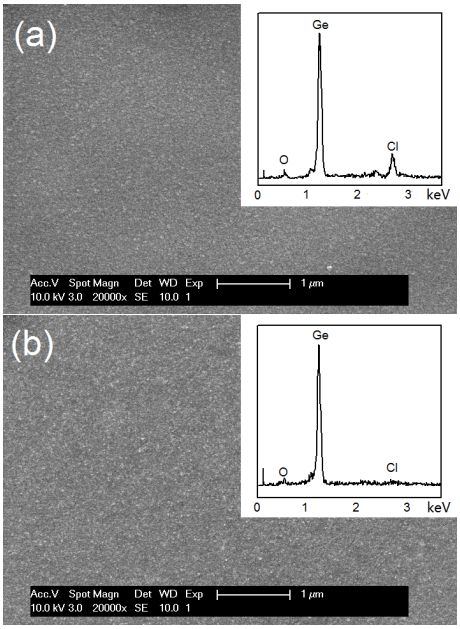

Figure 5.13: SEM images of electrodeposited germanium films. The germanium films were electrodeposited from [BMP][Tf_2N] solution containing 0.5 M $GeCl_4$ at different potentials and temperatures:(a) -1.2 V at 150 °C and (b) -0.9 V at 180 °C for one hour. The counter electrode was a p-type germanium wafer. The solution was stirred by a magnetic stir bar.



Figure 5.14: Photograph of the germanium film electrodeposited at -0.9 V at 180 °C for one hour. The counter electrode was a p-type germanium wafer. The solution was stirred by a magnetic stirrer bar.

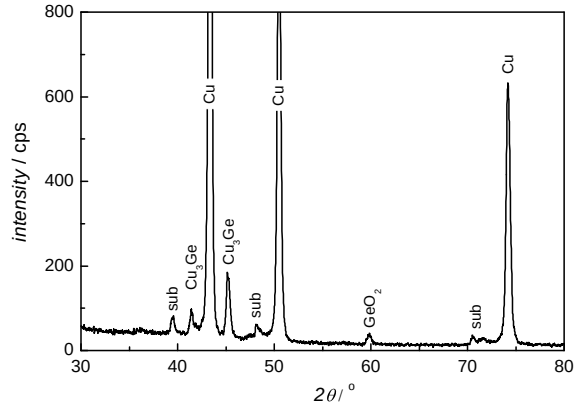

Figure 5.15: XRD pattern of the germanium film deposited on copper substrate from 0.5 M $GeCl_4$ in [BMP][Tf_2N] at 150 °C. The deposition potential was -1.5 V vs. Pt. The counter electrode was a p-type germanium wafer. The peaks labeled as “sub" came from the the XRD pattern originated from the sample holder.

germanium layer deposited on germanium substrate shows the interface was not clean (Figure 5.16). The electron diffraction patterns indicates that the deposited germanium film was amorphous whereas the substrate was single crystalline. In order to eliminate oxygen from the germanium substrates, a positive potential of +1.0 V was applied for different times (3 s, 10 s, 15 s and 20 s) before deposition to dissolve the top layer of germanium. The films were characterized by electron backscatter diffraction (EBSD). Kikuchi pattern of germanium was always found on the substrates, but the electrodeposited films did not give rise to any Kikuchi diffraction patterns. Epitaxial growth of germanium was not successful even with the pre-dissolution of germanium wafer before deposition.

Figure 5.17 shows the SEM image of the cross-section of a thick germanium film (75 µm thick) electrodeposited on germanium. The film was very dense but partially delaminated from the substrate. The deposition rate reached about 6.0 µm h^{-1}. The energy-dispersive X-ray spectroscopy (EDS) illustrates the presence of chlorine as well as oxygen and carbon impurities. The purity of the germanium film was further analyzed using Auger electron spectroscopy (AES) (Figure 5.18). Without etching, carbon and oxygen were detected on the surface of the electrodeposited germanium and the germanium peaks were almost invisible which means the germanium surface was covered with a contamination layer. After the first etching cycle, the oxygen and carbon peaks reduced and

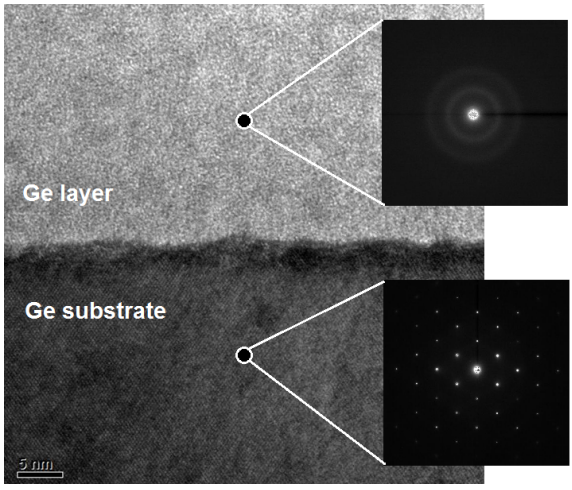

Figure 5.16: TEM image and electron diffraction patterns of the cross-section of the germanium film electrodeposited on an n-type germanium substrate. The film was deposited from 0.5 M $GeCl_4$ in [BMP][Tf_2N] at 180 °C at -0.9 V vs. Pt. The solution was stirred by a magnetic stir bar.

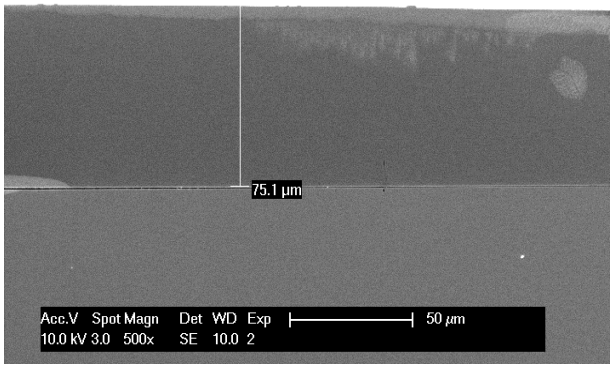

Figure 5.17: SEM image of the cross-section of the germanium film electrodeposited on an n-type germanium substrate. The film was deposited from 0.5 M $GeCl_4$ in [BMP][Tf_2N] at 180 °C at -0.9 V vs. Pt for 12.4 h. The solution was stirred by a magnetic stir bar.

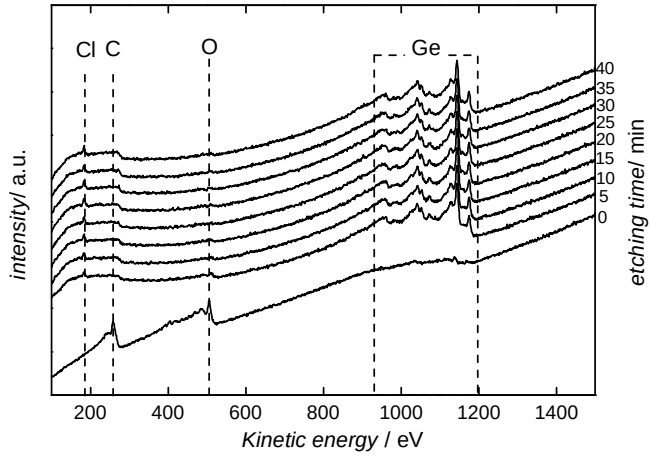

Figure 5.18: Auger electron spectra of the germanium film deposited on an n-type germanium substrate from 0.5 M $GeCl_4$ in [BMP][Tf_2N] at 180 °C at -0.9 V vs. Pt.

germanium peaks can be clearly observed. However a small peak at about 184 eV appeared which is associated with chlorine. Carbon and oxygen peaks were vanished after four etching cycles, but the chlorine peak was still there. The concentration of chlorine in germanium is difficult to quantify due to the low signal intensity and thus a low signal-to-noise ratio, therefore no proper peak fitting could be obtained. The presence of those impurities in the film can be another reason for the absence of epitaxial growth.

5.4 Conclusions

The electrodeposition of germanium from $GeCl_4$ in the ionic liquid 1-butyl-1-methylpyrrolidinium bis(trifluoromethylsulfonyl)imide has been studied in a pressure cell at elevated temperatures up to 180 °C. The viscosity of the solution decreased from 69.7 10^{-3} Pa s at room temperature to 3.8 10^{-3} Pa s at 150 °C. The diffusion coefficient of germanium increased to 1.9 10^{-10} m^2 s^{-1} at 150 °C. High deposition rates up to 6.0 µm h^{-1} could be obtained. The germanium films obtained at elevated temperatures had a grey or silver shiny metallic color. The germanium deposited on both platinum and n-type germanium substrates was amorphous. Orange germanium films were also obtained from 1-butyl-1-methylpyrrolidinium dicyanamide containing [$GeCl_4(BuIm)_2$] at 120

°C. The deposition rate reached 2.0 µm h^{-1}. Due to the fast polymerization of dicyanamide anions at elevated temperatures, germanium films could not be obtained in this ionic liquid at temperatures higher than 140 °C.

Chapter 6

General conclusions and outlook

6.1 Conclusions

6.1.1 General conclusions

The research presented in this thesis concerned two main topics: (1) electrodeposition of room temperature thermoelectric materials Bi_2Te_3 and multilayered $Bi_2Te_3/(Bi_{1-x}Sb_x)_2Te_3$ thin films from ethylene glycol solutions without chloride ions; and (2) electrodeposition of germanium from ionic liquids at room temperature and elevated temperatures up to 180 °C.

The first topic includes Chapter 2 and Chapter 3. Chloride-free ethylene glycol solutions were used to investigate the electrodeposition of bismuth, tellurium, antimony and their alloys. Te(IV) has a high solubility up to 0.5 M in chloride-free ethylene glycol solutions. This value is more than two orders of magnitude larger than its solubility in acidic solutions. Transparent precipitates formed in concentrated chloride-free tellurium solution after a long time. This precipitation is a new compound with tellurium chelated by four ethylene glycol molecules. In tellurium solutions, the exchange current density is much lower than that in bismuth solutions, but the diffusion coefficient of Te(IV) is higher than Bi(III). In the solutions containing bismuth and tellurium, equilibrium alloy deposition was achieved in low concentrated solutions, which is very rare in alloy deposition. The film composition can easily be controlled by the ratio

of metal ions in the solution. The electrodeposited films are very flat and uniform. Both n-type and p-type bismuth telluride films were obtained from the chloride-free ethylene glycol solutions. A maximum Seebeck coefficient of -120 $\mu V\ K^{-1}$ was obtained. The deposition of antimony was found having two steps: at lower overpotential amorphous antimony layer could be formed, whereas crystalline antimony was formed at higher overpotentials. The deposition of bismuth-antimony and antimony-tellurium followed the behavior of regular alloy deposition. The ternary alloys could be electrodeposited from the solutions as well. The antimony content in the film increased with higher rotation speed or higher overpotential was applied. The ternary alloys have a similar crystal texture as the bismuth telluride deposited from ethylene glycol. Multilayered $Bi_2Te_3/(Bi_{1-x}Sb_x)_2Te_3$ thin films were obtained and the layer thickness is adjustable by the pulsed time. By making this multilayered structure, the thermal conductivity is expected to be reduced whereas the Seebeck coefficient is expected to be increased.

Chapter 4 and Chapter 5 present the study of second topic. In Chapter 4, black germanium films were electrodeposited from [BMP][DCA] at room temperature containing the germanium compound $[GeCl_4(BuIm)_2]$. Ge(IV) is first reduced to Ge(II) and then Ge(II) is further reduced to Ge(0). The deposition rate calculated from the mass change on EQCM was 0.87 $\mu m\ h^{-1}$. Electropolymerization of $[DCA]^-$ anions on the anode was observed and reported for the first time. A yellow organic layer formed on the anode during deposition and this layer is poorly conductive. By mixing [BMP][DCA] and [BMP]Cl, the polymerization can be significantly suppressed. The deposition was performed at 100 °C due to the high melting point of [BMP]Cl and also lead to an increased current density. The current density could not be increased by increasing the concentration because the viscosity also increased as more germanium compound was dissolved. Only a small amount of oxygen impurity was found in the germanium films which could be due to the oxidation of germanium in the air. Electrodeposition of germanium was carried out at even higher temperatures up to 180 °C to increase the deposition rate. To prevent the polymerization of $[DCA]^-$ anions, $GeCl_4$ in $[BMP][Tf_2N]$ was used. The current density at elevated temperatures was much higher than that at room temperature which is because of an increase of the diffusion rate of germanium. The diffusion coefficient of germanium at 150 °C is 22 times larger than that at room temperature. The deposition rate reached 6 $\mu m\ h^{-1}$ at 180 °C. Efforts were made to deposit homo-epitaxial germanium, but only amorphous germanium layers were obtained because of the poor cleanliness of the germanium substrates. The film morphology also improved by increasing the deposition temperature. Grey films could be obtained instead of black germanium layer that were obtained from ionic liquids at room temperature.

6.1.2 Breakthroughs

The main breakthroughs of this PhD research include:

- Equilibrium alloy deposition of Bi_2Te_3 was achieved in chloride-free ethylene glycol solutions. It is very rare to find a system in which the deposited alloy composition can be simply adjusted by the corresponding ion ratio in the electrolytes. Precise control of the film composition is crucial for thermoelectric materials since their thermoelectric properties strongly depend on the composition.
- Thermoelectric multilayers were successfully electrodeposited from an ethylene glycol bath. Making a multilayer structure can improve the ZT number of thermoelectric materials by reducing the thermal conductivity and increasing the Seebeck coefficient. Using pulsed potential deposition, multilayers can be obtained from a single bath and the layer thicknesses can be easily controlled by pulsed time.
- Germanium was electrodeposited from [BMP][DCA] containing [$GeCl_4$-$(BuIm)_2$]. Unlike the germanium films deposited from other ionic liquids using $GeCl_4$ as the germanium source, the films obtained from [BMP][DCA] do not contain chlorine impurities and only oxygen impurities can be detected. Exclusion of chlorine impurities is vital for the solar cell application.
- Electro-polymerization of $[DCA]^-$ anions was found and reported for the first time. During electrodeposition, $[DCA]^-$ anions form an insulating polymer on the anode which stops the electrodeposition after a certain time. The product of electro-polymerization of $[DCA]^-$ has been recently found to be useful in supercapacitors by another group [189].
- Shiny grey germanium films were electrodeposited from [BMP][Tf_2N] containing $GeCl_4$ at elevated temperatures up to 180 °C in a pressure cell. Black germanium films are always obtained from ionic liquids at room temperature. By elevating the deposition temperature, the film morphology is improved and compact shiny germanium films can be obtained. Besides the improvement of morphology, thick germanium films can be obtained at a high deposition rate.

6.2 Outlook for future research

At the end of this dissertation, some suggestions and prospects are given based on the research results and conclusions.

How to improve the thermoelectric performance? To have a high figure of merit ZT, low thermal conductivities κ and high power factors $S^2\sigma$ are desired. There are several approaches to reduce the thermal conductivity which were discussed in Chapter 1 already. One of the approaches that can be achieved by electrodeposition is incorporation of nanoparticles in thermoelectric thin films. We did several preliminary experiments of electrodeposition bismuth telluride thin films with silica nanoparticles. Because the refractive indices of silica nanoparticles and ethylene glycol are very close, the attractive force between nanoparticles is reduced which enables the deposition of individual nanoparticles rather than agglomerates. The thermal conductivity is expected to be reduced due to the phonon scattering by the particles in the films.

Characterization of thermoelectric properties of electrodeposited thermoelectric thin films. The Seebeck coefficient of thermoelectric thin films were measured by the method reported in [49]. To have a reliable Seebeck coefficient, the sheet resistance of the film should be 10 times smaller than the seed layer ($R_{\mathrm{film}}/R_{\mathrm{seed}} < 0.1$) which means a minimum thickness of 10 µm is required for the film. However, in most of the cases, 10 µm is not thick enough to fulfill the requirement. This can be due to the low resistivity of the seed layer. Titanium coated substrates can be an alternative choice in the future. Another possible solution is to calculate the deviation between the theoretical and the experimental values and find a correction coefficient for different $R_{\mathrm{film}}/R_{\mathrm{seed}}$ ratios. Thermoelectric multilayers were prepared in order to reduce the thermal conductivity and increase the figure of merit ZT. The thermal conductivity is an important parameter here to prove the validation of the theory. So far, the results of thermal diffusivity measurements were not reliable enough to report. It is interesting and important to have a reliable thermal diffusivity measurement for thin films.

Electrodeposition crystalline germanium. We failed in electrodepositing germanium epitaxially on a single-crystal germanium wafer at elevated temperatures. This might be due to the insufficient surface cleanliness of the substrate. Some surface treatment tricks can be used to improve the surface condition. First of all, the substrates have to be cleaned according to the RCA process to remove the native oxides and then transferred into the cell quickly. However the “clean” surfaces may be oxidized again before they are transferred into the electrolyte or even oxidized in the electrolyte during heating up. Further efforts on making clean substrates are requird for epitaxial germanium deposition.

Bibliography

[1] Eds.: D. M. Rowe, *CRC Handbook of Thermoelectrics*, CRC Press LLC (1995). pages 2, 7, 9, 55

[2] T. C. Harman, P. J. Taylor, M. P. Walsh, B. E. LaForge, Quantum dot superlattice thermoelectric materials and devices, *Science*, **27**, 2229–2232 (2002). pages 3, 10

[3] C. Wood, Materials for thermoelectric energy conversion, *Rep. Prog. Phys.*, **51**, 459–539 (1988). pages 6

[4] J. M. O. Zide, D. Vashaee, Z. X. Bian, G. Zeng, J. E. Bowers, A. Shakouri, A. C. Gossard, Demonstration of electron filtering to increase the Seebeck coefficient in $In_{0.53}Ga_{0.47}As/In_{0.53}Ga_{0.28}Al_{0.19}As$ superlattices, *Phys. Rev. B*, **74**, 205335 (2006). pages 5

[5] M. Zebarjadi, K. Esfarjani, A. Shakouri, Z. Bian, J.-H. Bahk, G. Zeng, J. Bowers, H. Lu, J. Zide, A. Gossard, Effect of nanoparticles on electron and thermoelectric transport, *J. Electron. Mater.*, **38**, 954–959 (2009). pages 5

[6] C. Shuo, Z. Ren, Recent progress of half-Heusler for moderate temperature thermoelectric applications, *Materials today*, **16**, 387–395 (2013). pages 6

[7] B. Yu, M. Zebarjadi, H. Wang, K. Lukas, H. Wang, D. Wang, C. Opeil, M. Dresselhaus, G. Chen, Z. Ren, Enhancement of thermoelectric properties by modulation-doping in silicon germanium alloy nanocomposites, *Nano Lett.*, **12**, 2077–2082 (2012). pages 6

[8] S. Mishra, S. Satpathy, O. Jepsen, Electronic structure and thermoelectric properties of bismuth telluride and bismuth selenide, *J. Phys.: Condens. Matter*, **9**, 461–470 (1997). pages 7

[9] J. Drabble, C. Goodman, Chemical bonding in bismuth telluride, *J. Phys. Chem. Solids*, **5**, 142–144 (1958). pages 7

[10] V. Wanger, G. Dolling, B. Powell, G. Landweher, Lattice vibrations of Bi_2Te_3, *Phys. Stat. Sol (b)*, **85**, 311–317 (1978). pages 7

[11] J. Black, E. Conwell, L. Seigle, C. Spencer, Electrical and optical properties of some $m_2^{V-B}n_3^{VI-B}$ semiconductors, *J. Phys. Chem. Solids*, **2**, 240–251 (1957). pages 7

[12] A. LaLonde, Y. Pei, H. Wang, G. J. Snyder, Lead telluride alloy thermoelectrics, *Materials Today*, **14**, 526–532 (2011). pages 8

[13] S. V. Eremeev, G. Landolt, T. V. Menshchikova, B. Slomski, Y. M. Koroteev, Z. S. Aliev, M. B. Babanly, J. Henk, A. Ernst, L. Patthey, A. Eich, A. A. Khajetoorians, J. Hagemeister, O. Pietzsch, J. Wiebe, R. Wiesendanger, P. M. Echenique, I. R. Tsirkin, Stepan S. abd Amiraslanov, J. H. Dil, E. V. Chulkov, Atom-specific spin mapping and buried topological states in a homologous series of topological insulators, *Nat. Commun.*, **3**, 635 (2011). pages 9

[14] J. Fleurial, C. Gabrielli, R. Triboulte, H. Scherrer, S. Scherrer, Thermal properties of high quality single crystals of bismuth telluride–Part I: Experimental characterization, *J. Phys. Chem. Solids*, **49**, 1237–1247 (1988). pages 9, 11

[15] T.-S. Oh, D.-B. Hyun, N. Kolomoets, Thermoelectric properties of the hot-pressed $(Bi,Sb)_2(Te,Se)_3$ alloys, *Scripta Mater.*, **42**, 849–854 (2000). pages 7

[16] X.-D. Liu, Y.-H. Park, Structure and transport properties of $(Bi_{1-x}Sb_x)_2Te_3$ thermoelectric materials prepared by mechanical alloying and pulse discharge sintering, *Mater. Trans.*, **43**, 681–687 (2002). pages 7, 10, 69

[17] S. LeBlanc, Thermoelectric generators: Linking material properties and systems engineering for waste heat recovery applications, *SM&T*, **1–2**, 26–35 (2014). pages 10

[18] R. Venkatasubramanian, E. Siivola, T. Colpitts, B. O'Quinn, Thin-film thermoelectric devices with high room-temperature figures of merit, *Nature*, **413**, 597–602 (2001). pages 10, 55

[19] J.-P. Fleurial, A. Borshchevsky, M. Ryan, W. Phillips, E. Kolawa, T. Kacisch, R. Ewell, Thermoelectric microcoolers for thermal management applications, In: *Thermoelectrics, 1997. Proceedings ICT '97. XVI International Conference on* (1997). pages 10

[20] R. Venkatasubramanian, T. Colpitts, E. Watko, M. Lamvik, N. El-Masry, MOCVD of Bi_2Te_3, Sb_2Te_3 and their superlattice structures for thin-film thermoelectric applications, *J. Cryst. Growth*, **170**, 817–821 (1997). pages 10

[21] X. Wang, A. Yamamoto, K. Eguchi, H. Obara, T. Yoshida, Thermoelectric properties of SiC thick films deposited by thermal plasma physical vapor deposition, *Sci. Technol. Adv. Mater.*, **4**, 167–172 (2003). pages 10

[22] D. Hill, L. Williams, G. Mah, W. Bradley, The effect of physical vapor deposition parameters on the thermoelectric power of thin film molybdenum-nickel junctions, *Thin Solid Films*, **40**, 263–270 (1977). pages 10

[23] Eds.: R. Eason, *Pulsed laser deposition of thin films*, John Wiley & Sons. Inc., Hoboken, New Jersey (2007). pages 10

[24] R. S. Makala, K. Jagannadham, B. C. Sales, Pulsed laser deposition of $Bi_2Te_3Bi_2Te_3Bi_2Te_3$-based thermoelectric thin films, *J. Appl. Phys.*, **94**, 3907–3918 (2003). pages 10

[25] A. Bailini, F. Donati, M. Zamboni, V. Russo, M. Passoni, A. L. Casari, C.S. amd Bassi, C. Bottani, Pulsed laser deposition of Bi_2Te_3 thermoelectric films, *Appl. Surf. Sci.*, **254**, 1249–1254 (2007). pages 10

[26] Y. Kim, A. DiVenere, G. K. L. Wong, J. B. Ketterson, S. Cho, J. R. Meyer, Structural and thermoelectric transport properties of $Sb_2Te_3Sb_2Te_3Sb_2Te_3$ thin films grown by molecular beam epitaxy, *J. Appl. Phys.*, **91**, 715–718 (2002). pages 10

[27] A. Ibrahim, D. Thompson, Ion beam mixing to produce bi/sb alloys for thin film thermoelectric devices, *Nucl. Instrum. Methods Phys. Res., Sect. B*, **7**, 566–570 (1985). pages 10

[28] H.-B. Lee, H. J. Yang, J. H. We, K. Kim, K. C. Choi, B. J. Cho, Thin-film thermoelectric module for power generator applications using a screen-printing method, *J. Electron. Mater.*, **40**, 615–619 (2011). pages 10

[29] A. Chen, D. Madan, P. K. Wright, J. W. Evans, Dispenser-printed planar thick-film thermoelectric energy generators, *J. Micromech. Microeng.*, **21**, 104006 (8pp) (2011). pages 10

[30] C. Navone, M. Soulier, M. Plissonnier, A. L. Seiler, Development of $(Bi,Sb)_2(Te,Se)_3$-based thermoelectric modules by a screen-printing process, *J. Electron. Mater.*, **39**, 1755–1759 (2010). pages 10

[31] F. Xiao, C. Hangarter, B. Yoo, Y. Rheem, K.-H. Lee, N. V. Myung, Recent progress in electrodeposition of thermoelectric thin films and nanostructures, *Electrochim. Acta*, **53**, 8103–8117 (2008). pages 10, 37

[32] F. Völklein, V. Baier, U. Dillner, E. Kessler, Transport properties of flash-evaporated $(Bi_{1-x}Sb_x)_2Te_3$ films I: Optimization of film properties, *Thin Solid Films*, **187**, 253–262 (1990). pages 10

[33] J. George, B. Pradeep, Preparation and properties of co-evaporated bismuth telluride [Bi_2Te_3] thin films, *Solid State Commun.*, **56**, 117–120 (1985). pages 10

[34] Y. H. Shing, Y. Chang, A. Mirshafii, L. Hayashi, S. S. Roberts, J. Y. Josefowicz, N. Tran, Sputtered Bi_2Te_3 and PbTe thin films, *J. Vac. Sci. Technol. A*, **1**, 503–506 (1983). pages 10

[35] S. E. Huq, R. A. McMahon, H. Ahmed, Deposition of thin films using the ionised cluster beam method, *Semicond. Sci. Technol. 5 771*, **5**, 771–781 (1990). pages 10

[36] C. Boulanger, Thermoelectric material electroplating: a historical review, *J. Electron. Mater.*, **39**, 1818–1827 (2010). pages 11, 37

[37] J. Yang, W. Zhu, X. Gao, S. Bao, X. Fan, Electrochemical aspects of the formation of Bi_2Te_3 thin film via the route of ECALE, *J. Electroanal. Chem.*, **577**, 117–123 (2005). pages 11

[38] P. Heo, K. Hagiwara, R. Ichino, M. Okido, Electrodeposition and thermoelectric characterization of Bi_2Te_3, *J. Electrochem. Soc.*, **153**, C213–C217 (2006). pages 11, 37

[39] M. Takahashi, M. Kojima, S. Sato, N. Ohnisi, A. Nishiwaki, K. Wakita, T. Miyuki, S. Ikeda, Y. Muramatsu, Electric and thermoelectric properties of electrodeposited bismuth telluride (Bi_2Te_3) films, *J. Appl. Phys.*, **96**, 5582–5587 (2004). pages 11

[40] Eds.: M. Pourbaix, *Atlas of electrochemical equilibria in aqueous solutions*, National association of corrosion engineers (1974). pages 11, 55

[41] B. Yoo, C.-K. Huang, J. Lim, J. Herman, M. Ryan, J.-P. Fleurial, N. Myung, Electrochemically deposited thermoelectric n-type Bi_2Te_3 thin films, *Electrochim. Acta*, **50**, 4371–4377 (2005). pages 11, 55

[42] W. W. Feihui Li, Electrodeposition of $Bi_xSb_{2-x}Te_y$ thermoelectric thin films from nitric acid and hydrochloric acid systems, *Appl. Surf. Sci.*, **255**, 4225–4231 (2009). pages 11

[43] F. Golgovici, A. Cokocaru, M. Nedelcu, T. Visan, Voltammetric and impedance studies of electrodeposition of Te and its binary compounds with Bi and Sb using choline chloride- urea based electrolyte, *Chalcogenide Lett.*, **6**, 323–333 (2009). pages 11, 61

[44] C. Agapescu, A. Cojocaru, A. Cotarta, T. Visan, Electrodeposition of bismuth, tellurium, and bismuth telluride thin films from choline chloride-oxalic acid ionic liquid, *J. Appl. Electrochem.*, **43**, 309–321 (2013). pages 11

[45] F. Golgovici, A. Cojocaru, M. Nedelcu, T. Visan, Cathodic deposition of components in BiSbTe ternary compounds as thermoelectric films using choline-chloride-based ionic liquids, *J. Electron. Mater.*, **39**, 2079–2084 (2010). pages 11

[46] M. Martín-González, A. L. Prieto, M. S. Knox, R. Gronsky, T. Sands, A. M. Stacy, Electrodeposition of $Bi_{1-x}Sb_x$ films and 200-nm wire arrays from a nonaqueous solvent, *Chem. Mater.*, **15**, 1671–1681 (2003). pages 11, 55

[47] F.-H. Li, W. Wang, Electrodeposition of *p*-type $Bi_xSb_{2-x}Te_y$ thermoelectric film from dimethyl sulfoxide solution, *Electrochim. Acta*, **55**, 5000–5005 (2010). pages 11, 55

[48] W.-J. Li, W.-L. Yu, C.-Y. Yen, Pulsed electrodeposition of Bi_2Te_3 and Bi_2Te_3/Te nanowire arrays from a DMSO solution, *Electrochim. Acta*, **58**, 510–515 (2011). pages 11, 55

[49] H. Nguyen, J. Su, Z. Wang, R. Vullers, P. M. Vereecken, J. Fransaer, Measuring in-plane Seebeck coefficicent of electroplated thermoelectric films in presence of a conductive seed layer, *J. Mater. Res*, **26**, 1953–1957 (2011). pages 11, 38, 69, 128

[50] H. Alexander, P. Haasen, Dislocations and plastic flow in the diamond structure, *Solid State Phys.*, **22**, 27–159 (1968). pages 12

[51] J. Vanhellemont, E. Simoen, Brother silicon, sister germanium, *J. Electrochem. Soc.*, **154**, H572–H583 (2007). pages 12

[52] Eds.: R. E. Krebs, *The History and Use of Our Earth's Chemical Elements: A Reference Guide*, Greenwood Press, Westport (1992). pages 12

[53] J. Burton, F. Culkin, J. Riley, The abundances of gallium and germanium in terrestrial materials, *Geochim. Cosmochim. Acta*, **6**, 151–180 (1959). pages 12

[54] W. C. Butterman, J. D. Jorgenson, Mineral commodity profiles-Germanium, Technical report, U.S. Department of the interior & U.S. Geological Survey (2005). pages 12, 13, 14

[55] D. E. Guberman, 2007 Minerals Yearbook – Germanium, Technical report, U.S. Department of the interior & U.S. Geological Survey (2007). pages 12

[56] R. Moskalyk, Review of germanium processing worldwide, *Miner. Eng.*, **17**, 393–402 (2004). pages 13

[57] B. Abeles, R. W. Cohen, Ge-Si thermoelectric power generator, *J. Appl. Phys.*, **35**, 247–248 (1964). pages 14

[58] M. Wuttig, N. Yamada, Phase-change materials for rewriteable data storage, *Nat. Mater.*, **6**, 824–832 (2007). pages 14

[59] L. Testardi, J. Wernick, W. Royer, Superconductivity with onset above 23° k in Nb-Ge sputtered films, *Solid State Commun.*, **15**, 1–4 (1974). pages 14

[60] M.-H. Park, K. Kim, J. Kim, J. Cho, Flexible dimensional control of high-capacity Li-ion-battery anodes: From 0d hollow to 3d porous germanium nanoparticle assemblies, *Adv. Mater.*, **22**, 415–418 (2010). pages 14

[61] S. Yoon, C.-M. Park, H.-J. Sohn, Electrochemical characterizations of germanium and carbon-coated germanium composite anode for lithium-ion batteries, *Electrochem. Solid-State Lett.*, **11**, A41–A45 (2008). pages 14

[62] C. G. Fink, V. M. Dokras, Electrodeposition and electrowinning of germanium, *J. Electrochem. Soc.*, **95**, 80–97 (1949). pages 14, 16, 101

[63] R. I. Jaffee, E. W. McMullen, B. W. Gonser, Technology of germanium, *J. Electrochem. Soc.*, **89**, 277–290 (1946). pages 14

[64] J. I. Hall, A. E. Koenig, Electrochemical properties of germanium, *Trans. Electrochem. Soc.*, **65**, 215–219 (1934). pages 15

[65] A. I. Carim, S. M. Collins, J. M. Foley, S. Maldonado, Benchtop electrochemical liquid–liquid–solid growth of nanostructured crystalline germanium, *J. Am. Chem. Soc.*, **133**, 13292–13295 (2011). pages 15, 101

[66] Ed.: C. Hirayama, C. Guminski, Z. Galus, *Solubility dataMetals in Merdata series Volume 25 – Metals in Mercury*, Pergamon Press (1986). pages 15

[67] J. Gu, S. M. Collins, A. I. Carim, X. Hao, B. M. Bartlett, S. Maldonado, Template-free preparation of crystalline ge nanowire film electrodes via an electrochemical liquid-liquid-solid process in water at ambient pressure and temperature for energy storage, *Nano Lett.*, **12**, 4617–4623 (2012). pages 15

[68] E. Fahrenkrug, J. Gu, S. Jeon, P. A. Veneman, R. S. Goldman, S. Maldonado, Room-temperature epitaxial electrodeposition of single-crystalline germanium nanowires at the wafer scale from an aqueous solution, *Nano Lett.*, **14**, 847–852 (2014). pages 15, 118

[69] M. De Bonte, J. R. Celis, J. P. ; Roos, Electrodeposition of thick and bright silver-germanium alloy coatings, *Plat. Surf. Finish.*, **80**, 43–47 (1993). pages 16

[70] N. Chandrasekharan, S. C. Sevov, Anodic electrodeposition of germanium films from ethylenediamine solutions of deltahedral Ge_9^{4-} zintl ions, *J. Electrochem. Soc.*, **157**, C140–C145 (2010). pages 16, 17, 101

[71] Q. Huang, S. W. Bedell, K. L. Saenger, M. Copel, H. Deligianni, L. T. Romankiw, Single-crystalline germanium thin films by electrodeppositon and solid-phase epitaxy, *Electrochem. Solid-State Lett.*, **10**, D124–D126 (2007). pages 16, 17

[72] G. Szekely, Electrodeposition of germanium, *J. Electrochem. Soc.*, **98**, 318–324 (1951). pages 16, 77, 101

[73] M. J. Jawad, M. R. Hashim, N. K. Ali, E. P. Córcoles, M. E. Sharifabad, An alternative method to grow Ge thin films on Si by electrochemical deposition for photonic applications, *J. Electrochem. Soc.*, **159**, D124–D128 (2012). pages 17, 101

[74] M. Armand, F. Endres, D. R. MacFarlane, H. Ohno, B. Scrosati, Ionic-liquid materials for the electrochemical challenges of the future, *Nat. Mater.*, **8**, 621–629 (2009). pages 17, 77, 101

[75] N. V. Plechkova, K. R. Seddon, Applications of ionic liquids in the chemical industry, *Chem. Soc. Rev.*, **37**, 123–150 (2008). pages 17, 101

[76] M. Johnston, J.-J. Lee, G. S. Chottiner, B. Miller, T. Tsuda, C. L. Hussey, D. A. Scherson, Electrochemistry in ultrahigh vacuum: underpotential deposition of Al on polycrystalline W and Au from room temperature $AlCl_3$/1-ethyl-3-methylimidazolium chloride melts, *J. Phys. Chem. B*, **109**, 11296–11300 (2005). pages 17

[77] S. Schaltin, A. Shkurankov, K. Binnemans, J. Fransaer, Direct Cu-on-Ta electroplating from ionic liquids in high vacuum, *ECS Trans.*, **25**, 119–128 (2010). pages 17

[78] S. Schaltin, L. D'Urzo, Q. Zhao, A. Vantomme, H. Plank, G. Kothleitner, C. Gspan, K. Binnemans, J. Fransaer, Direct electroplating of copper on tantalum from ionic liquids in high vacuum: origin of the tantalum oxide layer, *Phys. Chem. Chem. Phys.*, **14**, 13624–13629 (2012). pages 17, 77, 104

[79] Ed.: F. Endres, D. MacFarlane, A. Abbott, *Electrodeposition from ionic liquids*, Wiley-VCH Weinheim (2008). pages 18, 101

[80] F. Endres, Electrodeposition of a thin germanium film on gold from a room temperature ionic liquid, *Phys. Chem. Chem. Phys.*, **3**, 3165–3174 (2001). pages 18, 77, 101

[81] F. Endres, S. Z. E. Abedin, Nanoscale electrodeposition of germanium on Au(111) from an ionic liquid: an in situ STM study of phase formation, part II. Ge from $GeCl_4$, *Phys. Chem. Chem. Phys*, **4**, 1649–1657 (2002). pages 18, 77, 80, 101, 113

[82] F. Endres, S. Z. E. Abedin, Nanoscale electrodeposition of germanium on Au(111) from an ionic liquid: an in situ STM study of phase formation part I. Ge from $GeBr_4$, *Phys. Chem. Chem. Phys*, **4**, 1640–1648 (2002). pages 18, 77, 101

[83] F. Endres, Electrodeposition of nanosized germanium from $GeBr_4$ and $GeCl_4$ in an ionic liquid, *Electrochem. Solid-State Lett.*, **5**, C38–C40 (2002). pages 18, 77, 80, 101, 117

[84] A. Lahiri, M. Olschewski, O. H'offt, S. Z. E. Abedin, F. Endres, In situ spectroelectrochemical investigation of Ge, Si, and Si $_x$Ge$_{1-x}$ electrodeposition from an ionic liquid, *J. Phys. Chem. C*, **117**, 1722–1727 (2013). pages 18, 19

[85] I. Mukhopadhyay, W. Freyland, Thickness induced metal-nonmetal transition in ultrathin electrodeposited Ge films, *Chem. Phys. Lett.*, **377**, 223–228 (2003). pages 18, 80, 101

[86] F. Martineau, K. Namur, J. Mallet, F. Delavoie, F. Endres, M. Troyon, M. Molinari, Electrodeposition at room temperature of amorphous silicon and germanium nanowires in ionic liquid, *Mater. Sci. Eng.*, **6**, 012012 (2009). pages 18, 19, 101

[87] R. Al-Salman, S. Z. El Abedin, F. Endres, Electrodeposition of Ge, Si and Si_xGe_{1-x} from an air- and water-stable ionic liquid, *Phys. Chem. Chem. Phys.*, **10**, 4650–4657 (2008). pages 18, 77, 101

[88] R. Al-Salman, M. A. Zoubi, F. Endres, Evidence for an influence of anodic decomposition products of ionic liquids on the electrodeposition of Si_xGe_{1-x} semiconductor, *J. Mol. Liq.*, **160**, 114–118 (2011). pages 19, 77, 80

[89] A. Lahiri, S. Zein El Abedin, F. Endres, UV-assisted electrodeposition of germanium from an air- and water-stable ionic liquid, *J. Phys. Chem. C*, **116**, 17739–17745 (2012). pages 19

[90] X. Meng, R. Al-Salman, J. Zhao, N. Borissenko, Y. Li, F. Endres, Electrodeposition of 3D ordered macroporous germanium from ionic liquids: A feasible method to make photonic crystals with a high dielectric constant, *Angew. Chem. Int. Ed.*, **48**, 2703–2707 (2009). pages 19, 78, 101

[91] X. Liu, J. Hao, X. Liu, C. Chi, N. Li, Y. Endres, Frank Zhang, Y. Li, J. Zhao, Preparation of Ge nanotube arrays from an ionic liquid for lithium ion battery anodes with improved cycling stability, *Chem. Commun.*, **51**, 2064–2067 (2015). pages 19

[92] J. Ke, P. N. Bartlett, D. Cook, T. L. Easun, M. W. George, W. Levason, G. Reid, D. Smith, W. Su, W. Zhang, Electrodeposition of germanium from supercritical fluids, *Phys. Chem. Chem. Phys.*, **14**, 1517–1528 (2012). pages 19, 77, 101

[93] R. Memming, *Semiconductor electrochemistry*, Wiley-VCH Weinheim (2001). pages 21, 22, 24, 26, 28, 98

[94] I. Teerlinck, *Electrochemical copper deposition in IC manufacturing*, PhD thesis, Universiteit Gent (2002). pages 28

[95] Ed.: A. J. Bard, M. Stratmann, S. Licht, *Encyclopedia of Electrochemistry, Volume 6, Semiconductor Electrodes and Photoelectrochemistry*, Wiley-VCH (2002). pages 30

[96] S. Jain, D. Roulston, A simple expression for band gap narrowing (BGN) in heavily doped Si, Ge, GaAs and Ge_xSi_{1-x} strained layers, *Solid-State Electron.*, **34**, 453–465 (1991). pages 30

[97] H. E. Dillon, Jr. J. A anad Farnsworth, Work-function studies of germanium crystals cleaned by ion bombardment, *J. Appl. Phys.*, **28**, 174 (1957). pages 31

[98] D. Haneman, Photoelectric emission and work functions of insb, gaas, bi2te3 and germanium, *J. Phys. Chem. Solids*, **11**, 209–214 (1959). pages 31

[99] L. Apker, E. Taft, J. Dickey, Photoelectric emission and contact potentials of semiconductors, *Phys. Rev.*, **74**, 1462–1474 (1948). pages 31

[100] D. V. Melnikov, J. R. Chelikowsky, Electron affinities and ionization energies in Si and Ge nanocrystals, *Phys. Rev. B*, **69**, 113305 (2004). pages 31

[101] A. Dimoulas, P. Tsipas, A. Sotiropoulos, Fermi-level pinning and charge neutrality level in germanium, *Appl. Phys. Lett.*, **89**, 252110 (2006). pages 31

[102] Y. Miyazaki, T. Kajitani, Preparation of Bi_2Te_3 films by electrodeposition, *J. Cryst. Growth*, **229**, 542–546 (2001). pages 37

[103] P. Magri, C. Boulanger, J.-M. Lecuire, Synthesis, properties and performances of electrodeposited bismuth telluride films, *J. Mater. Chem.*, **6**, 773–779 (1996). pages 37

[104] Y. Ma, E. Ahlberg, Y. Sun, B. B. Iversen, A. E. Palmqvist, Thermoelectric properties of thin films of bismuth telluride electrochemically deposited on stainless steel substrates, *Electrochim. Acta*, **56**, 4216–4223 (2011). pages 37, 55

[105] H. P. Nguyen, M. Wu, J. Su, R. J. Vullers, P. M. Vereecken, J. Fransaer, Electrodeposition of bismuth telluride thermoelectric films from a nonaqueous electrolyte using ethylene glycol, *Electrochim. Acta*, **68**, 9–17 (2012). pages 37, 38, 40, 46, 48, 55

[106] Eds.: D. M. Rowe, *CRC Handbook of Thermoelectrics*, CRC Press, Boca Raton (1995). pages 37, 46

[107] N. Brooks, M. Wu, L. Van Meervelt, K. Binnemans, J. Fransaer, Bis(ethyleneglycolato-o,o')tellurium(iv), *Acta Crystallogr. Sect. E: Struct. Rep. Online*, **69**, o1080 (2013). pages 39

[108] S. Treimer, A consideration of the application of Koutecký-Levich plots in the diagnoses of charge-transfer mechanisms at rotated disk electrodes, *Electroanalysis*, **14**, 154–171 (2002). pages 42, 60, 85

[109] A. J. Bard, L. R. Faulkner, *Electrochemical methods fundamentals and applications*, New York (N.Y.) : Wiley (2001). pages 42, 44, 87

[110] Y. Castrillejo, G. Haarberg, S. Palmero, R. Pardo, P. S. Batanero, Chemical and electrochemical behaviour of $BiCl_3$ in a $PbCl_2$ + KCl equimolar mixture at 475 °C, *J. Electroanal. Chem.*, **373**, 149–155 (1994). pages 44

[111] R. Johansson, The exchange processes between bismuth chloride complexes and liquid bismuth amalgam, *Acta Chem. Scand.*, **18**, 1809–1822 (1964). pages 44

[112] T. Montiel-Santillan, O. Solorza-Feria, H. Sanchez-Soriano, Tellurium electrodeposition like a precursor to prepare the *p*-CdTe semiconductor, *Int. J. Hydrogen Energy*, **27**, 461–464 (2002). pages 45

[113] A. Brenner, *Electrodeposition of alloys: Principle and practice*, volume I. Academic press, New York and London (1963). pages 48, 49

[114] L. E. Bell, Cooling, heating, generating power, and recovering waste heat with thermoelectric systems, *Science*, **321**, 1457–1461 (2008). pages 55

[115] W. Liu, K. C. Lukas, K. McEnaney, S. Lee, Q. Zhang, C. P. Opeil, G. Chen, Z. Ren, Studies on the Bi_2Te_3-Bi_2Se_3-Bi_2S_3 system for mid-temperature thermoelectric energy conversion, *Energy Environ. Sci.*, **6**, 552–560 (2013). pages 55

[116] B. C. Sales, Smaller is cooler, *Science*, **295**, 1248–1249 (2002). pages 55

[117] B. Poudel, Q. Hao, Y. Ma, Y. Lan, A. Minnich, B. Yu, X. Yan, D. Wang, A. Muto, D. Vashaee, X. Chen, J. Liu, M. S. Dresselhaus, G. Chen, Z. Ren, High-thermoelectric performance of nanostructured bismuth antimony telluride bulk alloys, *Science*, **320**, 634–638 (2008). pages 55

[118] A. Purkayastha, A. Jain, C. Hapenciuc, R. Buckley, B. Singh, C. Karthik, R. J. Mehta, T. Borca-Tasciuc, G. Ramanath, Synthesis and thermoelectric properties of thin film assemblies of bismuth telluride nanopolyhedra, *Chem. Mater.*, **23**, 3029–3031 (2011). pages 55

[119] C. B. Vining, An inconvenient truth about thermoelectrics, *Nat. Mater.*, **8**, 83–85 (2009). pages 55

[120] C. Frantz, N. Stein, Y. Zhang, E. Bouzy, O. Picht, M. Toimil-Molares, C. Boulanger, Electrodeposition of bismuth telluride nanowires with controlled composition in polycarbonate membranes, *Electrochim. Acta*, **69**, 30–37 (2012). pages 55

[121] I. Y. Erdogan, Ümit Demir, Orientation-controlled synthesis and characterization of Bi_2Te_3 nanofilms, and nanowires via electrochemical co-deposition, *Electrochim. Acta*, **56**, 2385–2393 (2011). pages 55

[122] L. Hicks, M. Dresselhaus, Effect of quantum-well stuctures on the thermoelectric figue of merit, *Phys. Rev. B*, **47**, 12727–12731 (1993). pages 55

[123] W. Glatz, L. Durrer, E. Schwyter, C. Hierold, Novel mixed method for the electrochemical deposition of thick layers of $Bi_{2+x}Te_{3-x}$ with controlled stoichiometry, *Electrochim. Acta*, **54**, 755–762 (2008). pages 55

[124] H. Köse, M. Bicer, C. Tutunoglu, A. O. Aydin, I. Sisman, The underpotential deposition of $Bi_2Te_{y-3}Se_y$ thin films by an electrochemical co-deposition method, *Electrochim. Acta*, **54**, 1680–1686 (2009). pages 55

[125] Y. Ma, E. Ahlberg, Y. Sun, B. B. Iversen, A. E. C. Palmqvist, Thermoelectric characteristics of electrochemically deposited Bi_2Te_3 and Sb_2Te_3 thin films of relevance to multilayer preparation, *J. Electrochem. Soc.*, **159**, D50–D58 (2012). pages 55

[126] D. Banga, J. L. Lensch-Falk, D. L. Medlin, V. Stavila, N. Y. C. Yang, D. B. Robinson, P. A. Sharma, Periodic modulation of Sb stoichiometry in $Bi_2Te_3/Bi_{2-x}Sb_xTe_3$ multilayers using pulsed electrodeposition, *Cryst. Growth Des.*, **12**, 1347–1353 (2012). pages 55, 69

[127] X. Li, K. Cai, D. Yu, Y. Wang, Electrodeposition and characterization of thermoelectric Bi_2Te_2Se/Te multilayer nanowire arrays, *Superlattices Microstruct.*, **50**, 557–562 (2011). pages 55

[128] B. Yoo, F. Xiao, K. N. Bozhilov, J. Herman, M. A. Ryan, N. V. Myung, Electrodeposition of thermoelectric superlattice nanowires, *Adv. Mater.*, **19**, 296–299 (2007). pages 55

[129] M. Wu, H. P. Nguyen, R. J. Vullers, P. M. Vereecken, K. Binnemans, J. Fransaer, Electrodeposition of bismuth telluride thermoelectric films from chloride–free ethylene glycol solutions, *J. Electrochem. Soc.*, **4**, D196–D201 (2013). pages 55, 56, 61, 72

[130] Y. N. Sadana, J. P. Singh, R. Kumar, Electrodeposition of antimony and antimony alloys–A review, *Surf. Coat. Technol.*, **24**, 319–353 (1985). pages 55

[131] J. Kuleshova, E. Koukharenko, X. Li, N. Frety, I. S. Nandhakumar, J. Tudor, S. P. Beeby, N. M. White, Optimization of the electrodeposition process of high-performance bismuth antimony telluride compounds for thermoelectric applications, *Langmuir*, **26**, 16980–16985 (2010). pages 55

[132] H. P. Nguyen, X. Peng, G. Murugan, R. J. M. Vullers, P. M. Vereecken, J. Fransaer, Electrodeposition of antimony, tellurium and their alloys from

molten acetamide mixtures, *J. Electrochem. Soc.*, **160**, D75–D79 (2013). pages 55

[133] G. Leimkühler, I. Kerkamm, R. Reineke-Koch, Electrodeposition of antimony telluride, *J. Electrochem. Soc.*, **149**, C474–C478 (2002). pages 55

[134] M.-H. Yang, M.-C. Yang, I.-W. Sun, Electrodeposition of indium antimonide from the water-stable 1-ethyl-3-methylimidazolium chloride/tetrafluoroborate ionic liquid, *J. Electrochem. Soc.*, **150**, C544–C548 (2003). pages 55

[135] Q. Huang, A. J. Kellock, S. Raoux, Electrodeposition of sbte phase-change alloys, *J. Electrochem. Soc.*, **155**, D104–D109 (2008). pages 55

[136] X. Dou, G. Li, H. Lei, X. Huang, L. Li, I. W. Boyd, Template epitaxial growth of thermoelectric Bi/BiSb superlattice nanowires by charge-controlled pulse, *J. Electrochem. Soc.*, **156**, K149–K154 (2009). pages 55

[137] H. Ebe, M. Ueda, T. Ohtsuka, Electrodeposition of Sb, Bi, Te, and their alloys in $AlCl_3$-NaCl-KCl molten salt, *Electrochim. Acta*, **53**, 100–105 (2007). pages 55

[138] A. L. Pitman, M. Pourbaix, N. de Zoubov, Potential-pH diagram of the antimony-water system: Its applications to properties of the metal, its compounds, its corrosion, and antimony electrodes, *J. Electrochem. Soc.*, **104**, 594–600 (1957). pages 55

[139] W. Qiu, S. Yang, T. Zhu, J. Xie, X. Zhao, Antimony telluride thin films electrodeposited in an alkaline electrolyte, *J. Electron. Mater.*, **40**, 1506–1511 (2011). pages 55

[140] H. Yamamoto, R. Iguchi, M. Morishita, Electrodeposition of Zn-Sb alloy film from ethylene glycol solvent, *ECS Trans*, **16**, 191–201 (2009). pages 55

[141] G. Sauerbrey, Verwendung von Schwingquarzen zur Wägung dünner Schichten und zur Mikrowägung, *Z. Phys.*, **155**, 206–222 (1959). pages 57

[142] C. Gabrielli, M. Keddam, R. Torresi, Calibration of the electrochemical quartz crystal microbalance, *J. Electrochem. Soc.*, **138**, 2657–2660 (1991). pages 57, 80, 103

[143] A. J. Bard, R. Parsons, J. Jordan, *Standard potentials in aqueous solutions*, CRC Press, New York (1985). pages 58

[144] F. Li, W. Wang, Y. Gong, J. Li, Electrodeposition of Sb_xTe_y thermoelectric films from dimethyl sulfoxide solution, *J. Electron. Mater.*, **41**, 3039–3043 (2012). pages 58

[145] C. Wang, Y. Du, Z. Zhou, The study of antimony underpotential deposition on gold electrode and its analytical application, *Electroanalysis*, **14**, 849–852 (2002). pages 58

[146] Y.-C. Fu, J.-W. Yan, Y. Wang, J.-H. Tian, H.-M. Zhang, Z.-X. Xie, B.-W. Mao, In situ STM studies on the underpotential deposition of antimony on Au(111) and Au(100) in a $BMIBF_4$ ionic liquid, *J. Phys. Chem. C*, **111**, 10467–10477 (2007). pages 58

[147] C. Wickersham, G. Bajor, J. Greene, Impulse stimulated "explosive" crystallization of sputter deposited amorphous (In,Ga)Sb films, *Solid State Commun.*, **27**, 17–20 (1978). pages 58

[148] F. Aymerich, A. Delunas, On the explosive semiconductor-semimetal transition of antimony, *Phys. Stat. Sol (a)*, **31**, 165–170 (1975). pages 58

[149] G. Gore, On a peculiar phenomenon in the electro-deposition of antimony, *Philos. Mag.*, **9**, 73–74 (1855). pages 58

[150] C. Coffin, Studies on explosive antimony. ii. its structure, electrical conductivity, and rate of crystallization, *Proc. Roy. Soc A*, **152**, 47–63 (1935). pages 58

[151] J. Lensch-Falk, D. Banga, P. Hopkins, D. Robinson, V. Stavila, P. Sharma, D. Medlin, Electrodeposition and characterization of nano-crystalline antimony telluride thin films, *Thin Solid Films*, **520**, 6109–6117 (2012). pages 58

[152] H. Jung, N. V. Myung, Electrodeposition of antimony telluride thin films from acidic nitrate-tartrate baths, *Electrochim. Acta*, **56**, 5611–5615 (2011). pages 58

[153] M.-Y. Kim, T.-S. Oh, Crystallization behavior and thermoelectric characteristics of the electrodeposited Sb_2Te_3 thin films, *Thin Solid Films*, **518**, 6550–6553 (2010). pages 58

[154] Ed.: R. C. Alkire, D. M. Kolb, *Chemistry - Advances In Electrochemical Science And Engineering*, volume 7. Wiley-VCH, Weinheim (2002). pages 63

[155] T. Moffat, Electrodeposition of $Ni_{1-x}Al_x$ in a chloroaluminate melt, *J. Electrochem. Soc.*, **141**, 3059–3070 (1994). pages 63

[156] I. Johansen, R. Arntzen, S. Bergmann, S. Husa, K. Ingebrigtsen, J. Johannessen, J. Sandved, Examples of thin film applications in electronic devices, *Thin Solid Films*, **50**, 171–185 (1978). pages 77

[157] X. Sun, J. Liu, L. C. Kimerling, J. Michel, Room-temperature direct bandgap electroluminesence from Ge-on-Si light-emitting diodes, *Opt. Lett.*, **34**, 1198–1200 (2009). pages 77

[158] L. Tsybeskov, Silicon-germanium nanostructures for light emitters and on-chip optical interconnects, *Proc. IEEE*, **97**, 1284–1303 (2009). pages 77

[159] S. Devouge, J. Conti, A. Goldsztein, E. Gosselin, M. Brans, A. Voué, J. De Coninck, F. Homblé, E. Goormaghtigh, J. Marchand-Brynaert, Surface functionalization of germanium ATR devices for use in FTIR-biosensors, *J. Colloid Interface Sci.*, **332**, 408–415 (2009). pages 77

[160] T. Nagashima, K. Okumura, K. Murata, M. Yamaguchi, A germanium back-contact type cell for thermophotovoltaic applications, In: *Photovoltaic Energy Conversion, 2003. Proceedings of 3rd World Conference on Photovoltaic Energy Conversion*, volume 1, 200 –203 May (2003). pages 77

[161] G. Medeiros-Ribeiro, A. M. Bratkovski, T. I. Kamins, D. A. A. Ohlberg, R. S. Williams, Shape transition of germanium nanocrystals on a silicon (001) surface from pyramids to domes, *Science*, **279**, 353–355 (1998). pages 77

[162] X. Liang, Y.-G. Kim, D. K. Gebergziabiher, J. L. Stickney, Aqueous electrodeposition of Ge monolayers, *Langmuir*, **26**, 2877–2884 (2010). pages 77, 101

[163] M. Saitou, K. Sakae, W. Oshikawa, Evaluation of crystalline germanium thin films electrodeposited on copper substrates from propylene glycol electrolyte, *Surf. Coat. Technol.*, **162**, 101–105 (2002). pages 77, 101, 105

[164] J. Padro, L. Saiz, E. Guardia, Hydrogen bonding in liquid alcohols: a computer simulation study, *J. Mol. Struct.*, **416**, 243–248 (1997). pages 77

[165] N. Chandrasekharan, S. C. Sevov, Anodic electrodeposition of germanium films from ethylenediamine solutions of deltahedral Ge_9^{4-} zintl ions, *J. Electrochem. Soc.*, **157**(4), C140–C145 (2010). pages 77

[166] N. Chandrasekharan, S. C. Sevov, Structural, vibrational, and optical characterization of anodically electroplated germanium thin films, *J. Electrochem. Soc.*, **157**, C419–C423 (2010). pages 77

[167] M. C. Buzzeo, R. G. Evans, R. G. Compton, Non-haloaluminate room-temperature ionic liquids in electrochemistry – A review, *ChemPhysChem*, **5**, 1106–1120 (2004). pages 77

[168] S. Z. E. Abedin, F. Endres, Electrodeposition of metals and semiconductors in air- and water-stable ionic liquids, *ChemPhysChem*, **7**, 58–61 (2006). pages 77

[169] A. P. Abbott, K. J. McKenzie, Application of ionic liquids to the electrodeposition of metals, *Phys. Chem. Chem. Phys.*, **8**, 4265–4279 (2006). pages 77

[170] Eds.: H. Ohno, *Electrochemical aspects of ionic liquids*, John Wiley & Sons, Inc., Hoboken, New Jersey (2005). pages 77, 101

[171] F. Endres, C. Schrodt, In situ STM studies on germanium tetraiodide electroreduction on Au(111) in the room temperature molten salt 1-butyl-3-methylimidazolium hexafluorophosphate, *Phys. Chem. Chem. Phys.*, **2**, 5517–5520 (2000). pages 77

[172] F. Endres, The electrodeposition of germanium from an ionic liquid: A mini-review on the nanoscale processes, In: *Proceedings- Electrichemical Society PV*, 677–689 (2002). pages 77

[173] V. Najdanovic-Visak, J. M. S. S. Esperanca, L. P. N. Rebelo, M. N. da Ponte, H. J. R. Guedes, K. R. Seddon, J. Szydlowski, Phase behaviour of room temperature ionic liquid solutions: an unusually large co-solvent effect in (water+ethanol), *Phys. Chem. Chem. Phys.*, **4**, 1701–1703 (2002). pages 78

[174] R. Al-Salman, M. A. Zoubi, F. Endres, Template assisted electrodeposition of germanium and silicon nanowires in an ionic liquid, *Phys. Chem. Chem. Phys*, **10**, 6233–6237 (2008). pages 78

[175] X. Meng, J. Zhao, H. Li, F. Endres, Y. Li, Enhanced photoluminescence of ordered macroporous germanium electrochemically prepared from ionic liquids, *Opt. Express*, **20**, 9421–9430 (2012). pages 78

[176] R. Al-Salman, X. Meng, J. Zhao, Y. Li, U. Kynast, M. M. Lezhnina, F. Endres, Semiconductor nanostructures via electrodeposition from ionic liquids, *Pure Appl. Chem.*, **82**, 1673–1689 (2010). pages 78

[177] S. Murugesan, P. Kearns, K. J. Stevenson, Electrochemical deposition of germanium sulfide from room-temperature ionic liquids and subsequent Ag doping in an aqueous solution, *Langmuir*, **28**, 5513–5517 (2012). pages 78

[178] M.-J. Deng, P.-Y. Chen, T.-I. Leong, I.-W. Sun, J.-K. Chang, W.-T. Tsai, Dicyanamide anion based ionic liquids for electrodeposition of metals, *Electrochem. Commun.*, **10**, 213–216 (2008). pages 78

[179] O. Mann, W. Freyland, O. Raz, Y. Ein-Eli, Electrochemical deposition of ultrathin ruthenium films on Au (1 1 1) from an ionic liquid, *Chem. Phys. Lett.*, **460**, 178–181 (2008). pages 80

[180] R. Mukherjee, R. Krishnan, T.-M. Lu, N. Koratkar, Nanostructured electrodes for high-power lithium ion batteries, *Nano Energy*, **1**, 518–533 (2012). pages 87

[181] X.-L. Wang, W.-Q. Han, H. Chen, J. Bai, T. A. Tyson, X.-Q. Yu, X.-J. Wang, X.-Q. Yang, Amorphous hierarchical porous GeO_x as high-capacity anodes for Li ion batteries with very long cycling life, *J. Am. Chem. Soc.*, **133**, 20692–20695 (2011). pages 87

[182] S. Pahal, M. Deepa, S. Bhandari, K. Sood, A. Srivastava, Electrochromism and redox switching of cobalt hexacyanoferrate-polyaniline hybrid films in a hydrophobic ionic liquid, *Sol. Energy Mater. Sol. Cells*, **94**, 1064–1075 (2010). pages 93

[183] J. Gu, E. Fahrenkrug, S. Maldonado, Direct electrodeposition of crystalline silicon at low temperatures, *J. Am. Chem. Soc.*, **135**, 1684–1687 (2013). pages 101

[184] W. Xin, J. Zhao, D. Ge, Y. Ding, Y. Li, F. Endres, Two-dimensional Si_xGe_{1-x} films with variable composition made via multilayer colloidal temperature guided ionic liquid electrodeposition, *Phys. Chem. Chem. Phys.*, **48**, 2421–2426 (2013). pages 101

[185] R. W. Chia, C. C. Wang, J. J. Lee, Effect of adatom mobility and substrate finish on film morphology and porosity: thin chromium film on hard disk, *J. Magn. Magn. Mater.*, **209**, 45–49 (2000). pages 101

[186] M. Wu, N. R. Brooks, S. Schaltin, K. Binnemans, J. Fransaer, Electrodeposition of germanium from the ionic liquid 1-butyl-1-methylpyrrolidinium dicyanamide, *Phys. Chem. Chem. Phys*, **15**, 4955–4964 (2013). pages 101, 102, 104, 105

[187] Eds.: R. E. Hummel, *Electronic Properties of Materials*, Springer Verlag, Berlin (2011). pages 102

[188] N. R. Brooks, S. Schaltin, K. Van Hecke, L. Van Meervelt, J. Fransaer, K. Binnemans, Heteroleptic silver-containing ionic liquids, *Dalton Trans.*, **41**, 6902–6905 (2012). pages 104

[189] T. Romann, O. Oll, P. Pikma, K. Kirsimäe, E. Lust, 4–10 V capacitors with graphene-based electrodes and ionic liquid electrolyte, *J. Power Sources*, **280**, 606–611 (2015). pages 105, 127

[190] O.-H. Kim, Y.-H. Cho, D. Y. Chung, M. J. Kim, J. M. Yoo, J. E. Park, H. Choe, Y.-E. Sung, Facile and gram-scale synthesis of metal-free catalysts: Toward realistic applications for fuel cells, *Sci. Rep.*, **5**, 8376 (2015). pages 105

[191] A. W. Laubengayer, D. L. Tabern, Germanium. XIV, *J. Phys. Chem*, **30**, 1047–1048 (1926). pages 106, 107

[192] M. Vranes, S. Dozic, V. Djeric, S. Gadzuric, Physicochemical characterization of 1-butyl-3-methylimidazolium and 1-butyl-1-methylpyrrolidinium bis(trifluoromethanesulfonyl)amide, *J. Chem. Eng. Data*, **57**, 1072–1077 (2012). pages 107

[193] M. Geppert-Rybczyńska, A. Knorr, J. K. Lehmann, A. Heintz, Liquid phase behavior of 1-butyl-1-methylpyrrolidinium bis(trifluoromethanesulfonyl)amide with 1-butanol or hexan-1-ol: measurements of coexistence curves, density, and interfacial tension, *J. Chem. Eng. Data*, **57**, 1923–1927 (2012). pages 107

[194] J. Russell, D. Giordano, , D. Dingwell, High-temperature limits on viscosity of non-arrhenian silicate melts, *Am. Mineral.*, **88**, 1390–1394 (2003). pages 107

[195] Ed.: M. Noel, K. I. Vasu, *Cyclic Voltammetry and the Frontiers of Electrochemistry*, Oxford & IBH Publishing Company (1990). pages 109

[196] X.-F. Xie, J.-W. Yan, J.-H. Liang, J.-J. Li, M. Zhang, B.-W. Mao, Underpotential deposition of germanium on Au(111) and Pt(111) surface in ionic liquid, *J. Electrochem*, **20**, 12–16 (2014). pages 113

[197] L. Daikhin, E. Gileadi, G. Katz, V. Tsionsky, M. Urbakh, D. Zagidulin, Influence of roughness on the admittance of the quartz crystal microbalance immersed in liquids, *Anal. Chem.*, **74**, 554–561 (2002). pages 113

[198] I. MAXTEK, *MAXTEK, INC.Operation and service manual- RQCM research quartz Crystal microbalance*, MAXTEK, INC. pages 114

[199] N.-J. Cho, J. N. D'Amour, J. Stalgren, W. Knoll, K. Kanazawa, C. W. Frank, Quartz resonator signatures under Newtonian liquid loading for initial instrument check, *J. Colloid Interface Sci.*, **315**, 248–254 (2007). pages 114

List of publications

1. **M. Wu**, G. Vanhoutte, N. R. Brooks, K. Binnemans and J. Fransaer, Electrodeposition of germanium at elevated temperatures and pressures from ionic liquids, *Phys. Chem. Chem. Phys*, **17**, 12080–12089 (2015).
2. S. Schaltin, G. Vanhoutte, **M. Wu**, F. Bardé and J. Fransaer, A QCM study of ORR-OER and an *in situ* study of a redox mediator in DMSO for Li-O_2 batteries, *Phys. Chem. Chem. Phys*, **17**, 12575–12586 (2015).
3. **M. Wu**, K. Binnemans and J. Fransaer, Electrodeposition of antimony from chloride-free ethylene glycol solutions and fabrication of thermoelectric $Bi_2Te_3/(Bi_{1-x}Sb_x)_2Te_3$ multilayer using pulsed potential electrodeposition, *Electrochim. Acta*, **147**, 451–459 (2014).
4. **M. Wu**, N. R. Brooks, S. Schaltin, K. Binnemans and J. Fransaer, Electrodeposition of germanium from the ionic liquid 1-butyl-1-methylpyrrolidinium dicyanamide, *Phys. Chem. Chem. Phys*, **15**, 4955–4964 (2013).
5. **M. Wu**, H. P. Nguyen, R. J. M. Vullers, P. M. Vereecken, K. Binnemans and J. Fransaer, Electrodeposition of bismuth telluride thermoelectric films from chloride-free ethylene glycol solutions, *J. Electrochem. Soc.*, **160**, D1–D6 (2013).
6. N. R. Brooks, **M. Wu**, L. Van Meervelt, K. Binnemans and J. Fransaer, Bis(ethyleneglycolato-O,O')tellurium(IV), *Acta Crystallogr. Sect. E: Struct. Rep. Online*, **69**, o1080 (2013).
7. H. P. Nguyen, **M. Wu**, J. Su, R. J. M. Vullers, P. M. Vereecken and J. Fransaer, *Electrochim. Acta*, **68**, 9–17 (2012).

List of Figures

1.1 Schematic of a thermoelectric generator. 4

1.2 Schematic of a thermoelectric cooler. 4

1.3 Charge carrier concentration dependency of Seebeck coefficient S, electrical conductivity σ, thermal conductivity κ and power factor $S^2\sigma$ (schematic). 6

1.4 Figure of merit of n-type and p-type materials at different temperatures. 8

1.5 Crystal structure of Bi_2Te_3. 9

1.6 Seebeck coefficient of bismuth-tellurium alloys at room temperature. 9

1.7 Seebeck coefficient of $(Bi_{1-x}Sb_x)_2Te_3$ alloys at room temperature. 10

1.8 Share of germanium use in different applications in the U.S. . . 14

1.9 Band diagram of metals and semiconductors. 22

1.10 Band diagram of n-type semiconductor-metal interface. 23

1.11 Band diagram of metal-semiconductor interface. 23

1.12 The electron energies of a redox system. 26

1.13 Energy scheme of an n-type semiconductor-electrolyte interface. 26

1.14 Energy diagram of the interface of semiconductor and redox system with different biases and the corresponding current. . . 29

1.15 Theoretical curves of the current density change vs. applied potential on an n-type electrode in the dark and under illumination 30

1.16 Band gap narrowing with the doping level. 30

1.17 The valence and conduction band positions and redox potentials of water. 32

2.1 Cyclic voltammograms from ethylene glycol solutions containing 0.05 M $Te(NO_3)_4$ or 0.05 M $TeCl_4$ and 0.5 M $LiNO_3$ at 50 °C. . 41

2.2 Cyclic voltammograms from ethylene glycol solutions containing 0.05 M $Bi(NO_3)_3$, 0.05 M $Te(NO_3)_4$, and 0.05 M $Bi(NO_3)_3$ + 0.05 M $Te(NO_3)_4$ (all with 0.5 M $LiNO_3$ supporting electrolyte) at 50 °C. 41

2.3 Polarization curves after iR correction and Koutecký-Levich plots for tellurium reduction at different potentials in an ethylene glycol solution containing 50 mM $Te(NO_3)_4$ and 0.5 M $LiNO_3$, at 50 °C. 43

2.4 $\ln(k)$ vs. η plots for bismuth and tellurium reductions from different chloride-containing and chloride-free ethylene glycol solutions at 50 °C. The concentrations of bismuth and tellurium salts were 0.05 M, of LiCl was 0.2 M. 44

2.5 SEM images of Te films deposited from ethylene glycol solutions containing 50 mM $TeCl_4$ or $Te(NO_3)_4$ and 0.5 M $LiNO_3$. 45

2.6 Composition of Bi_xTe_y films deposited at different potentials from a mixed solution containing 40 mM $Bi(NO_3)_3$, 60 mM $Te(NO_3)_4$, and 0.5 M $LiNO_3$. 46

2.7 SEM images of Bi_xTe_y films deposited from a mixed solution containing 40 mM $Bi(NO_3)_3$, 60 mM $Te(NO_3)_4$, and 0.5 M $LiNO_3$. 47

2.8 The XRD patterns of the films electrodeposited from the ethylene glycol solution containing 40 mM $Bi(NO_3)_3$, 60 mM $TeCl_4$ and 0.5 M $LiNO_3$ at different potentials. 47

2.9 Composition of Bi_xTe_y films deposited at different rotation speeds from a chloride-free ethylene glycol solution containing 50 mM $TeCl_4$, 50 mM $Bi(NO_3)_3$, and 0.5 M $LiNO_3$, at 50 °C. 48

2.10 SEM images of Bi_xTe_y films deposited at different rotation speeds from a mixed solution containing 50 mM $TeCl_4$, 50 mM $Bi(NO_3)_3$, and 0.5 M $LiNO_3$. 49

2.11 Variation of Bi_xTe_y film composition with respect to bath content at different applied potentials from non-stirred ethylene glycol solutions containing different total concentrations ([$Bi(NO_3)_3$. 50

3.1 Cyclic voltammograms of an ethylene glycol solution containing 0.05 M $Sb(NO_3)_3$ and 0.5 M $LiNO_3$ at 50 °C on different working electrodes. 59

3.2 SEM images of the antimony films deposited from a 50 mM $Sb(NO_3)_3$ and 0.5 M $LiNO_3$ solution in ethylene glycol at 50 °C at different potentials. 61

3.3 Cyclic voltammograms and corresponding real mass and theoretical mass changes on the crystal in ethylene glycol solutions containing 50 mM $Sb(NO_3)_3$ and 0.5 M $LiNO_3$, and 50 mM $SbCl_3$ and 0.5 M $LiNO_3$ at 50 °C. 62

3.4 SEM image of the antimony film deposited from a 50 mM $SbCl_3$ and 0.5 M $LiNO_3$ solution in ethylene glycol. 63

3.5 Polarization curves performed on an antimony-coated platinum rotating disk in an ethylene glycol solution containing 50 mM $Sb(NO_3)_3$ and 0.5 M $LiNO_3$ at 50 °C, and Levich plot. 64

3.6 Cyclic voltammograms in ethylene glycol solutions at 50 °C: (a) 50 mM $Sb(NO_3)_3$, 50 mM $Bi(NO_3)_3$ and 0.5 M $LiNO_3$, (b) 50 mM $Sb(NO_3)_3$, 50 mM $Te(NO_3)_4$ and 0.5 M $LiNO_3$. 65

3.7 Gibbs free energy of bismuth-antimony alloys and the calculated potential shift of antimony versus the mole fraction of antimony. 66

3.8 SEM images of the bismuth-antimony films deposited from a 50 mM $Sb(NO_3)_3$, 50 mM $Bi(NO_3)_3$ and 0.5 M $LiNO_3$ solution in ethylene glycol at 50 °C at different potentials. 67

3.9 Dependence of the film composition on the electrolyte bath composition at 50 °C without stirring. 68

3.10 SEM images of the antimony telluride films deposited from a 50 mM $Sb(NO_3)_3$, 50 mM $Te(NO_3)_4$ and 0.5 M $LiNO_3$ solution in ethylene glycol at 50 °C at different potentials. 68

3.11 SEM pictures of films electrodeposited from an ethylene glycol solution containing 20 mM $Bi(NO_3)_3$, 100 mM $Sb(NO_3)_3$ and 30 mM $Te(NO_3)_4$ with a rotation speed of 200 rpm at different potentials. 70

3.12 Composition of the films electrodeposited from an ethylene glycol solution containing 20 mM $Bi(NO_3)_3$, 100 mM $Sb(NO_3)_3$, 30 mM $Te(NO_3)_4$ and 0.5 M $LiNO_3$ at 50 °C on a rotating disk electrode with different rotating speeds. 71

3.13 SEM pictures of the films electrodeposited from an ethylene glycol solution containing 20 mM $Bi(NO_3)_3$, 100 mM $Sb(NO_3)_3$ and 30 mM $Te(NO_3)_4$ at -0.1 V with different rotation speeds. . 71

3.14 XRD patterns of the $(Bi_{1-x}Sb_x)_2Te_3$ films electrodeposited from an ethylene glycol solution containing 20 mM $Bi(NO_3)_3$, 100 mM $Sb(NO_3)_3$, 30 mM $Te(NO_3)_4$ and 0.5 M $LiNO_3$ at 50 °C. . . . 72

3.15 BSE images and antimony distribution of films electrodeposited from an ethylene glycol solution containing 20 mM $Bi(NO_3)_3$, 100 mM $Sb(NO_3)_3$, 30 mM $Te(NO_3)_4$ and 0.5 M $LiNO_3$ at 50 °C and for different rotation rates 73

4.1 Voltammograms of [BMP][DCA] on a platinum disk, and the electrochemical window is indicated as EW. 81

4.2 Structure of the germanium(IV) complex $[GeCl_4(BuIm)_2]$ . . . 82

4.3 Thermogravimetric analysis for pure $[GeCl_4(BuIm)_2]$ 82

4.4 Cyclic voltammograms at room temperature: (a,b) in the 0.1 M $[GeCl_4(BuIm)_2]$ solution in [BMP][DCA], dottedand solid lines represent illuminated and dark conditions, respectively; (c) in the 0.4 M $[GeCl_4(BuIm)_2]$ solution in [BMP][DCA]. 83

4.5 Cyclic voltammogram on a platinum coated quartz crystal and the crystal frequency change and M/z values for 0.1 M $[GeCl_4(BuIm)_2]$ solution in [BMP][DCA] at room temperature. 86

4.6 Polarization curves performed on a platinum rotating disk in the 0.1 M solution of $[GeCl_4(BuIm)_2]$ in [BMP][DCA] and Koutecký-Levich plot. 88

4.7 Cyclic voltammogram of 0.1 M $[GeCl_4(BuIm)_2]$ solution in [BMP 89

4.8 Plot of $\ln k$ vs. overpotential η in the solution of 0.1 M $[GeCl_4(BuIm)_2]$ in [BMP][DCA] at 50 °C. 89

4.9 SEM images of the film deposited from a 0.1 M $[GeCl_4(BuIm)_2]$ solution in [BMP][DCA] at 50 °C for 13 h. 90

4.10 The current density changes with time during potentiostatic electrodeposition at -0.65 V (vs. Ge) in the 0.1 M $[GeCl_4(BuIm)_2]$ solution in [BMP][DCA] and additional 1 10^{-6} M $SbCl_3$ at 50 °C. 90

4.11 SEM images of the germanium film deposited from a 0.4 M solution of $[GeCl_4(BuIm)_2]$ in [BMP][DCA] at room temperature and 50 °C. 92

4.12 Color changes of the electrolyte solution. 94

4.13 Picture of the n-type germanium wafer anode before and after electrodeposition in a 0.1 M $[GeCl_4(BuIm)_2]$ solution in [BMP][DCA]. 94

4.14 Frequency change on a platinum coated EQCM crystal in neat [BMP][DCA] at room temperature, and a constant current 0.05 A dm^{-2} was applied. 95

4.15 Sequential cyclic voltammograms of a 0.05 M ferrocene solution in [BMP][DCA] on a platinum disk at room temperature. . . . 95

4.16 Voltammograms of [BMP][DCA] and [BMP]Cl mixture (1:1 molar ratio) and cyclic voltammogram of 0.1 M $[GeCl_4(BuIm)_2]$ in [BMP][DCA] and [BMP]Cl mixture (molar ratio 1:1) at 100 °C 96

4.17 SEM images of the germanium film deposited on copper disks from 0.1 M and 0.2 M $[GeCl_4(BuIm)_2]$ in 1:1 molar ratio [BMP][DCA] and [BMP]Cl. 97

5.1 Schematic drawing of the electrochemical cell used for electrochemical experiments at elevated temperatures. 103

5.2 SEM image and EDX spectrum of the germanium film electrodeposited at -1.6 V from 0.4 M $[GeCl_4(BuIm)_2]$ in [BMP][DCA] at 120 °C. 105

5.3 Color changes of pure [BMP][DCA] after heating at 140 °C for different times. 106

5.4 Vapor pressure of $GeCl_4$ as a function of temperature. 107

5.5 Tammann-Vogel-Fulcher fitting of viscosity change of ionic liquid $[BMP][Tf_2N]$ with temperature. 108

5.6 Cyclic voltammograms of 0.5 M $GeCl_4$ in $[BMP][Tf_2N]$ at room temperature and 150 °C. 110

5.7 Linear scan voltammograms of [BMP][Tf_2N] solution containing 0.5 M $GeCl_4$ at room temperature. 111

5.8 Linear sweep voltammograms of 0.4 M [BMP]Cl in [BMP][Tf_2N] and pure [BMP][Tf_2N] at room temperature. 111

5.9 Cyclic voltammograms of 0.5 M $GeCl_4$ in [BMP][Tf_2N] with different scan rates at room temperature and 150 °C, and the plot of current density versus the square root of the scan rate v. 112

5.10 Cyclic voltammograms and corresponding mass change, M/z value change, and resonance resistance change in a [BMP][Tf_2N] solution containing 0.1 M $GeCl_4$ at 50 °C. 115

5.11 Rotating ring-disk electrode result from 0.5 M $GeCl_4$ in [BMP][Tf_2N] at room temperature: a cyclic voltammogram was applied on the disk and a ring potential of +1.3 V was applied. 117

5.12 Rotating ring-disk electrode result from 0.5 M $GeCl_4$ in [BMP][Tf_2N] at room temperature: a cyclic voltammogram was applied on the disk and a ring potential of +0.65 V was applied. 118

5.13 SEM images of the germanium films electrodeposited from [BMP][Tf_2N] solution containing 0.5 M $GeCl_4$ at different potentials and temperatures 119

5.14 Photograph of the germanium film electrodeposited at -0.9 V at 180 °C for one hour. 119

5.15 XRD pattern of the germanium film deposited on copper substrate from 0.5 M $GeCl_4$ in [BMP][Tf_2N] at 150 °C. 120

5.16 TEM image and electron diffraction patterns of the cross-section of the germanium film electrodeposited on an n-type germanium substrate. 121

5.17 SEM image of the cross-section of the germanium film electrodeposited on an n-type germanium substrate. 121

5.18 Auger electron spectra of the germanium film deposited on an n-type germanium substrate. 122

List of Tables

1.1 Germanium suppliers 13

1.2 Barrier height of metal/n-Ge Schottky diode 31

2.1 Corrosion rates of Bi and Te films in ethylene glycol solutions with and without chloride 40

2.2 Conductivity of different bismuth and tellurium ethylene glycol solutions at 50 °C 42

2.3 Kinetic parameters and diffusion coefficients for bismuth and tellurium in chloride-containing and chloride-free solutions . . . 45

4.1 Viscosities of [BMP][DCA] and 0.1 M and 0.4 M solution of $[GeCl_4(BuIm)_2]$ in [BMP][DCA] at different temperatures . . . 92

5.1 Viscosity of [BMP][Tf_2N] at different temperatures 108



FACULTY OF ENGINEERING SCIENCE
DEPARTMENT OF MATERIALS ENGINEERING
SURFACE AND INTERFACE ENGINEERED MATERIALS
Kasteelpark Arenberg 44 box 2450
B-3001 Heverlee
minxian.wu@mtm.kuleuven.be
http://www.mtm.kuleuven.be